Chalcopyrite-based micro-concentrator solar cells: realistic device modelling and fabrications

Dissertation

zur Erlangung des Grades eines
Doktors der Naturwissenschaften

im Fachbereich Physik der Freien Universität Berlin

angefertigt am

Helmholtz-Zentrum Berlin

vorgelegt von

Diego Sancho Martínez

Berlin, 2018

Erstgutachterin: **Frau Prof. Dr. Martina Schmid**

Zweitgutachter: **Herr Prof. Dr. Jan Behrends**

Tag der Disputation: **01.03.2019**

Index

Abbreviations and symbols

Listed in order of appearance in this work:

Symbol	Units	Description
CPV		Concentrator photovoltaics
III-V		Elements from the group III and V of the periodic table
CIGSe		$Cu(In_x,Ga_{1-x})Se_2$
CISe		$CuInSe_2$
SEM		Scanning Electron Microscope spectroscopy
EDX		Energy-Dispersive X-ray spectroscopy
IV-T		Current – Voltage dependence with Temperature
PL		Photoluminescence
XRF		X-ray fluorescence spectroscopy
FEM		Finite element analysis software
TWh	[TWh]	Tera-watts/hour
UN		United Nations
COP 23		United Nations Climate Conference Goals
PV		Photovoltaic
NREL		National Renewable Energy Laboratory
DNI		Direct Normal Irradiance
sun, suns, x	$[W/m^2]$	1000
CISe		$CuInSe_2$
PDT		Post-Deposition Treatment
NaF		Sodium fluoride
TOE		Thermal-Opto-Electronic simulation model
SLG		Soda-Lime Glass
Mo		Molybdenum
CdS		Cadmium sulfide
i-ZnO		Intrinsic Zinc oxide
AZO		Intrinsic Zinc oxide with Aluminum oxide, $ZnO:Al_2O_3$ 1.5 wt.%
BSG		Borosilicate Glass
Ni		Nickel
Al		Aluminum
CCR		Conduction, convection and radiation fundamental heat transfer modes
p	$[Kg/m^3]$	Density
k	$[W/(m\cdot K)]$	Thermal conductivity
C_p	$[J/(kg\cdot K)]$	Heat capacity
ε		Emissivity
h	$[W/(m\cdot K)]$	Convective heat transfer coefficient
Q	$[W/m^2]$	Heat source energy
σ	$[W/(m^2\cdot K^4)]$	Stefan-Boltzmann constant, 5.67037321 $W/(m^2\cdot K^4)$
$T_{solar\ cell}$	[K]	Temperature of the solar cell
q, q_0	$[W/m^2]$	Heat flux vector and inward

n		Normal vector of the boundary
C		Concentration factor
$Area_{solar\ cell}$		Area of the solar cell
AM1.5G		Irradiation standard spectrum (defined in *ASTM G-173)* for terrestrial applications, equivalent to 1000 [W/m^2]
AM1.5D		Irradiation standard spectrum (defined in *ASTM G-173)* for terrestrial applications, equivalent to 900 [W/m^2]
Ga		Gallium
eV	[J]	Electron volt, $1.602176620898 \cdot 10^{-19}$ [J]
GDOES		Glow-discharge optical emission spectroscopy
UV		Ultra-violet light
I	[A]	Current
I_{ph}	[A]	Photo-generated current
I_D	[A]	Current through a diode
I_{Rsh}	[A]	Current through a resistance R_{sh}
I_o	[A]	Diode current under no illumination
J_o	[A/m^2]	Current density under illumination
J_{oo}	[A/m^2]	Current density under no illumination
R_s	[Ω]	Series resistance
R_{sh}	[Ω]	Shunt resistance
q	[C]	Elementary charge constant, $1.6021766208(98) \cdot 10^{-19}$ C
k_B	[J/K]	Boltzmann constant, $1{,}3806488(13) \cdot 10^{-23}$ J/K
I_{sc}	[A]	Short-circuit current
E	[J]	Energy
V_{oc}	[V]	Open-circuit voltage
LED		Light Emitting Diode
n		Ideality factor of a diode
FF	[%]	Fill factor
η	[%]	Efficiency
L_n, L_p	[m]	Diffusion length of electrons and holes
W_p		Semiconductor base thickness
N_A, N_D	[cm^{-3}]	Density of acceptor and donor atoms
D_n, D_p	[cm^{-3}]	Minority-carrier diffusion coefficient of electrons and holes
τ_n, τ_p	[µs]	Minority-carrier diffusion recombination lifetime of electrons and holes
h^+, e^-		Hole and electron
m_n^*, m_p^*	[cm^{-3}]	Effective masses of electrons and holes
E_G	[J]	Energy between the valence band and the conduction band
α, β		Specific constants of a semiconductor device
n_i	[cm^{-3}]	Intrinsic carrier concentration
C-SoSim		Concentrator solar simulator
STC-20°C		Standard Test Conditions at 20°C
x, y, z	[m]	Cartesian coordinate system
θ_x, θ_y, θ_z	[rad]	Polar coordinate system
W	[eV]	Metal work function
Ref.SC		Planar Reference Solar Cell
G_{rate}	[$m^{-3} \cdot s^{-1}$]	Generation rate
λ	[nm]	Wavelength

Φ_s	[$m^{-2} \cdot s^{-1}$]	Photon flux
Q_{abs}	[W/m^3]	Deposited power per unit volume
P_{in}	[$m^{-2} \cdot s^{-1}$]	Total incident power
V_{abs}	[m^3]	Volume
t	[s]	Time
$\hat{\varepsilon}$, ε	[F/m]	Permittivity tensor and scalar
Φ	[V]	Electrostatic potential
ρ	[$C \cdot m^{-3}$]	Space charge density
p, n	[m^{-3}]	Hole and electron concentrations
ρ_p, ρ_n	[m^{-3}]	Trapped carrier density for holes and electrons
R_{rate}	[$m^{-3} \cdot s^{-1}$]	Recombination rate
μ_p, μ_n	[$m^2 \cdot V^{-1} \cdot s^{-1}$]	Carrier mobility for holes and electrons
HZB		Helmholtz-Zentrum Berlin
pn		Hetero-junction, p doped and n doped semiconductor materials
3D		3 dimensions
W		Wolframium
Cr		Chromium
Ta		Tantalum
Nb		Niobium
V		Vanadium
Ti		Titanium
Mn		Manganese
Se		Selenium
Cu		Copper
t	[m]	Thickness of a layer
π		Irrational number, 3.1415926(…)
r	[m]	Radius
V	[m^3]	Enclosed volume
A		Normalization value
σ	[m]	Gaussian standard deviation
FWHM	[m]	Full width at half maximum
TW	[m]	Tower width
$\varnothing$	[m]	Diameter
RMS		Root mean square
RAM		Random Access Memory
I-V	[A vs. V]	Current – voltage dependence
LCPV		Low CPV
AZ nLoF 2070, AZ2070		Negative photoresist
ARC		Anti-reflective coating
LSE		Lamellar-shaped solar cells produced by etching
LSS		Lamellar-shaped solar cells produced by shadowing
SiO_xN_{1-x}		Silicon oxinitridized
PVcomB		Competence Centre Thin-Film- and Nanotechnology for Photovoltaics Berlin
Na		Sodium
RTP		Rapid Thermal Process
In		Indium

KCN		Potassium cyanide
KOH		Potassium hydroxide
CBD		Chemical Bath Deposition
$CdCH_3COO{\cdot}2H_2O$		Cadmium acetate hydrate
NH_3		Ammonia
H_2O		Distilled water
CH_4N_2S		Thiourea
Hg		Mercury
AZ-D		Photoresist developer
DMSO		Photoresist removal
N_2		Nitrogen
RT	[K]	Room temperature, 20°C
LM01#1-4		Lithography mask number 1, sections 1 to 4
LM02#1-3		Lithography mask number 2, sections 1 to 3
PVcomB#50		Lithography mask from PVcomB, model 50
Br		Bromine
HCl		Hydrochloric acid
HNO_3		Nitric acid
H_2SO_4		Sulfuric acid
H_2O_2		Hydrogen peroxide
$MoSe_2$		Molybdenum diselenide
O_3		Trioxygen / Ozone
MoO_3		Molybdenum trioxide
pH		Potential of hydrogen
CGI		Cu/(Ga+In) atomic ratio
GGI		Ga/(Ga+In) atomic ratio
H_2Se		Hydrogen selenide
E_A	[J]	Activation energy
QFLS	[eV]	Quasi-Fermi Level Splitting
PL_{yield}	$[m^{-2}{\cdot}eV^{-1}{\cdot}s^{-1}]$	Photoluminescence yield
SRH		Shockley-Read-Hall recombination
RSS		Round-shaped solar cells produced by shadowing
RSE		Round-shaped solar cells produced by etching

Chapter 1:

Introduction

This chapter presents a brief overview of the current technological limitations and challenges which arise in concentrator photovoltaics. The main motivation in this field is focused on reducing cost of this technology and increasing the concentration factor applied on the solar cell. In this work, different simulations and experiments were analyzed to enhance the output power of the solar cell under different concentration factors and beam profiles. This chapter also explains the objectives and organization of this manuscript.

1.1. Motivation

Global carbon emissions are expected to increase over the next 25 years based on the growing energy demand outside developed countries, specifically, China and India. Models, of the world consumption of energy, project an increasing scenario where fossil fuels will cover over 75% of the world´s total energy demand by 2040 [1]. Natural gas followed by petroleum-based fuels will represent the main energy resources for energy production. However, even when alternative resources are expected to grow faster than fossil fuels, this growth will not cover more than 25% of the demand by 2040. Nevertheless, renewable energy is expected to grow more than any other energy source, followed by nuclear power, over the same period of time. Regarding coal, one of the largest sources of carbon emissions, will remain invariable until 2040 due to the replacement of this energy source with other more energy-efficient resources.

The transportation and industrial sectors are mainly responsible for the use and future demand growth of petroleum-based and liquid fuels. Over 115 million of barrels of crude oil will be used per day by 2040, an increment of 19% in 25 years. Only liquid fuels will provide 192 TWh by

2040, a remarkable amount of equivalent energy [2]. However, in the last years automobile manufacturers have started to offer a catalogue of electric cars to decrease the harmful gas emissions and to comply with increasingly restrictive policy in this field. It is widely accepted that such electric devices do not contribute to global carbon emissions, although this transportation method does not emit harmful gases, the generation of energy for such devices will be provided by the combustion of fossil fuels as the world consumption models depict. Hence, the emission of harmful gases will be localized in the region where this energy is produced. Nevertheless, renewable energy could lessen the amount of harmful gasses emitted if these resources are broadly implemented. As of the end of 2016, the contribution of renewable energy represents only 10% of the total energy demand. Even when the predictions for this kind of energy depict a greater increase in the following years, efforts must be made to boost the integration and expansion of renewable energy to decrease the CO_2 emissions rate over the next decades. Nevertheless, this reduction will not be sufficient to achieve the UN climate conference goals (*COP 23, Bonn*) [3] and to decrease the increasing greenhouse effect. Therefore, global warming will increase in the coming years.

Only the rapid deployment and support of renewable technology will lessen and change this tendency. As of 2016, the main renewable source by installed capacity was hydropower followed by wind energy, solar-thermal energy and solar-photovoltaic energy with a value of 44.3%, 19.7%, 18.4% and 12.3%, respectively [4]. Over the past years, the capacity installed, for solar-photovoltaics increased more than any other renewable technology. As of end of 2016, solar-PV power, wind power, solar-thermal and hydropower represented about 37.6%, 27.5%, 18.6% and 12.5% of the newly installed capacity. The continued drop in prices of the different technology explained this behavior, where solar-PV power was the biggest beneficiary.

Why concentrator photovoltaics?

Photovoltaics is a fast growing market, where silicon-based technology leads the production of energy with respect to other material-based devices. Moreover, the research community is making a huge effort to improve the current efficiency of the solar cells produced in lab scale and for outdoor applications. Figure 1.1 shows the recorded efficiency for different material-based solar cells in lab scale.

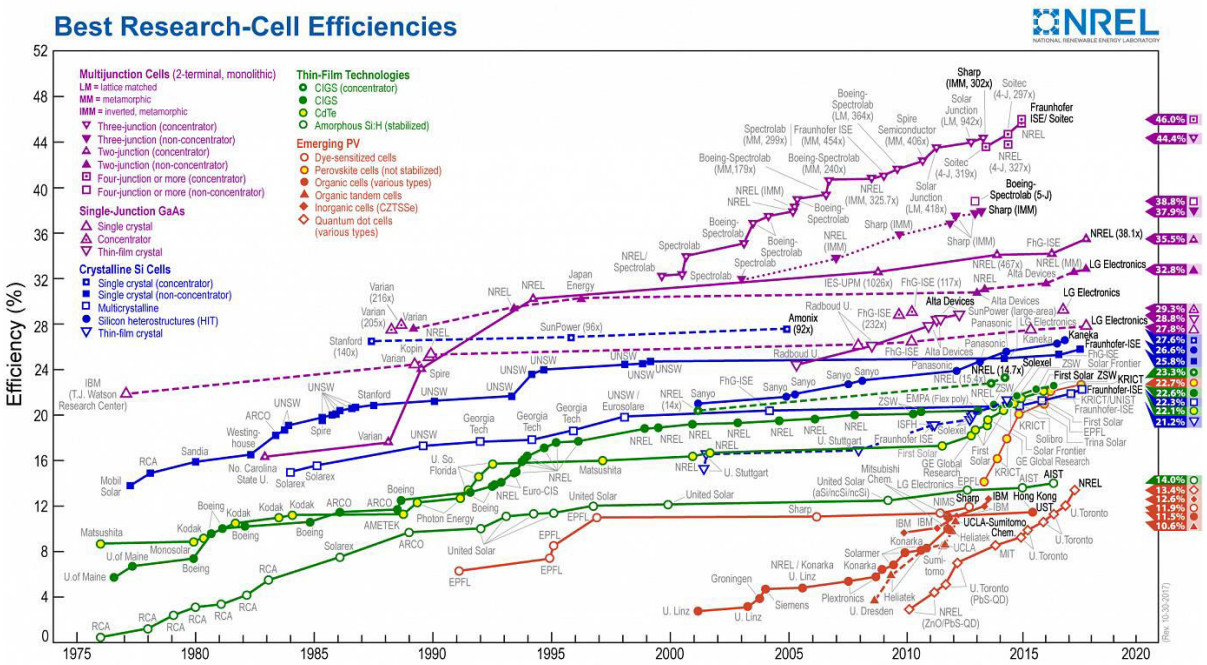

Figure 1.1: Recorded efficiency chart for different material-based solar cells in lab scale between 1975 and 2020 provided by the National Renewable Energy Laboratory (NREL) **[5]**.

As can be observed in Figure 1.1, for the same active area, the maximum efficiency is provided by solar cells with four-junctions or more under concentrated light, followed by non-concentrated devices and with fewer junctions. The power conversion to electricity is over 21% for most of the single-junction cells, above 32% for multi-junction devices and over 44% for multi-junction devices with concentrated light. Concentrator photovoltaic (*CPV*) is a highly efficient energy generator system with a high photovoltaic conversion rate [6]. This cost-effective method for power generation is recommended to be installed in regions with a large fraction of direct solar radiation (*DNI*). Furthermore, CPV modules are installed on trackers, which follow the sun´s path and ensure the illumination of the highly efficient multi-junction solar cells by concentrating sunlight on it with the help of optical elements. For high concentration (*>100 suns, i.e. >100x*) purposes, CPV modules should take into account the different operational and fabrication issues, which are usually present, so that the benefits achieved with concentration are not affected. As an example, these systems should include the alignment tolerances of the small solar cell area used, also the angular acceptance of the lens-cell system, as well as the accuracy of the mechanical tracking of the trackers. Moreover, CPV optical systems produce a uniform beam distribution on the surface of the solar cell when the suitable lenses are selected [7]. Different lens systems were developed for different applications

depending on the selected solar cell technology. High concentration factors require a large surface of the primary lens to guide the sunlight into the active area of the cell. Therefore, for this purpose, either Fresnel lens or mirrors are widely used [7]. Fresnel lens, which consists of a series of concentric grooves patterned into plastic, replaces traditional optical lenses with lightweight devices. However, and due to its nature, such lenses tend to be damaged by atmospheric conditions and sunlight, affecting the light distribution gathered to the cell. This kind of lens produces a non-homogeneous distribution, Gaussian like beam profile, of the light on the sample and also, chromatic aberrations. For single-junction solar cells this chromatic aberration is less dramatic than in multi-junction solar cells because the different diodes need to operate under the same conditions not to decrease the performance of the device. Therefore, a secondary lens system is included in the optical design to avoid different irradiance distributions and chromatic aberrations such as kaleidoscope homogenizers, Köhler-based integrators or conventional-based lenses [8], projecting Tower like beam profiles on the cell. However, one of the last achievements of the CPV community was the implementation of an optical system without chromatic aberration in a plastic-based Fresnel lens [9]. On the other hand, mirror-based concentrators have the advantage that such devices do not exhibit chromatic aberrations. Nevertheless, these devices require a secondary optical element to homogenize the light onto the cell surface [10]. Limits of the optical elements used for CPV applications were previously reported in more detail by Shanks *et al.* [7].

Sunlight is usually gathered to highly efficient solar cells, which are based on III-V semiconductor materials, with a current recorded efficiency over 46% under concentrated light (*508x*) achieved by Fraunhofer-ISE and Soitec [6] in lab scale. These multi-junction solar cells are capable of absorbing and converting sunlight radiation, in a wide wavelength range: from 300 nm up to 2000 nm, into electricity. However, the different layers of the multi-junction solar cells are relatively complex to be synthetized and fabricated. Furthermore, apart from these fabrication issues, the development of III-V-based solar cells relies on compounds listed as elements of risk for current supply [11], specifically, indium and gallium. These reasons are mainly responsible for the higher cost of this technology with respect to other material-based solar cells. Moreover, CPV designs include an active cooling device to minimize the temperature of the cell during the

operation. High concentration factors result in a high absorption in the solar cell of the incident light, part of this energy is converted into electricity but a large amount is exchanged as heat. If no active cooling is applied, the increasing temperature [12] [13] dramatically affects the overall performance of the highly efficient solar cells and, therefore, diminishing the benefit of concentrated light. Different active cooling systems used for CPV applications were previously reported in more detail by Zhangbo *et al.* [14].

However, the final cost of CPV devices is one of the main disadvantages of this technology which affect the integration and expansion of this renewable source of energy [15]. To achieve the price reduction of this technology, efforts must be made to reduce the cost of each element contained in a CPV device. By reducing the focal point of the primary optical element, the CPV module could be more compact and, therefore, implying a reduction of the material needed for the frame which protects lenses and cells from ambient conditions. In addition, by diminishing the focal point, the cost of delivering a module could be reduced due to the possibility of providing more modules within the same space. Also, a reduction of the total weight of the CPV module may reduce the requirements for the tracking system. For high concentration purposes, tracking systems require high accuracy for gathering the incoming light into the solar cell without penalty for the final performance of the cell. Moreover, the fabrication misalignments, such as cell positioning with respect to the focal point of the primary lens, or the inclination of the secondary optical element respective to the surface where it is glued, or the mechanical issues which appear during the tracking of the sun´s path, strongly affect the power conversion of CPV systems. A possible solution to mitigate the effect of these matters could be the use of a large solar cell to reduce the impact of fabrication and operation tolerances. By using a large solar cell, the active area will be properly illuminated whether the system is well positioned in relation to the sun´s path or if any of the discussed issues is present. However, a large solar cell will increase the cost and could mitigate the benefits of lower tracking requirements.

III-V-based solar cells are expensive compared to other material-based cells. Even when these cells provide a great power conversion rate to electricity, the cost per generated watt, a term used for comparison purposes, exceeds several orders of magnitude compared to the single-

junction silicon-based solar cells. Therefore, a suitable solar cell must be selected to reduce the cost of CPV technology, providing an acceptable performance.

As the concentration factor increases, the generated heat rises in the solar cell and, hence, the temperature of the device. Traditional CPV technology include an active cooling system to mitigate the effect of the temperature in the performance of the cell, however, for high concentration factors, the generated heat requires a costly cooling technique to dissipate this heat. By reducing the concentration factor, the temperature of the cell will diminish, but on the same manner, the advantages of light concentration. In order to reduce the cost of CPV technology, it is strongly recommended not to use active cooling systems but to design a device that gets the maximum effect of the heat dissipation by the fundamental heat transfer mechanisms in the structure.

Why micrometer-sized CIGSe concentrator photovoltaics?

Only the rapid deployment and support of CPV technology will lessen the price. Among the advantages of traditional III-V-based CPV devices, on the other hand, the need to reduce drastically the cost of such devices will be hand with hand with other material-based technology. As of the end of 2017, the newly record efficiency reached for $CuInSe_2$ (*CISe*) solar cells by Solar Frontier [16] and for $Cu(In_x,Ga_{1-x})Se_2$ (*CIGSe*) solar cells by ZSW [17] under indoor laboratory measurements were 22.9% and 22.6%, respectively. Chalcopyrite-based solar cells have given a great boost to achieve even greater efficiency recently. One of the latest achievements of the research community is the post-deposition treatment (*PDT*) applied to the finished solar cell by adding alkali metals, specifically, sodium and potassium, to reduce the recombination mechanism of the photo-generated light by passivating the grain boundaries. What started as a method to optimize the performance of solar cells developed at lower temperatures compared to the standard values [18], became a breakthrough in technology for chalcopyrite-based solar cells. The author forecasts, that even higher efficiency will be reached by this method, where the iteration of PDT processes with firstly light metals continuing with heavier metals will boost the final performance of chalcopyrite-based solar cells. As it has been reported, the treatment of chalcopyrite-based solar cells with NaF strongly affected the final performance of the cell [18], but the addition of potassium-based PDT processes was reported

to improve the power conversion to electricity [19]. The effect of potassium in chalcopyrite-based solar cells was previously reported in more detail by Muzzillo *et al.* [20]. Furthermore, by continuing to treat the finished solar cells with heavier alkali-based compounds, greater efficiency is expected to be reached [21]. Moreover, with the latest achievements of the research community, the efficiency gap between III-V-based and chalcopyrite-based solar cells is decreasing. However, in order to produce the same amount of energy, chalcopyrite-based solar cells also require twice as much area as III-V semiconductor materials. Apart from this, the cost of chalcopyrite-based technology is much times lower than for III-V-based devices. In this work, the author proposes the use of low cost chalcopyrite-based solar cells instead.

Chalcopyrite-based solar cells, as III-V-based devices, rely on compounds listed as elements of risk of current supply [11], specifically, indium and gallium. The use of these elements may be reduced by reducing the absorber thickness; however, this reduction leads to a weaker absorption of the sunlight, *i.e.* a decrease in the power conversion to electricity. Nevertheless, this drawback could be minimized by including nanostructures in the solar cell structure [22] [23]. Nanostructures, plasmonic or dielectric structures, are used to redirect sunlight into the absorber and attempt to be absorbed again, enhancing the cell performance despite the reduction of thickness. Although these attempts may reduce the final cost of the solar cell, a great material saving and, therefore, a great price reduction, could be achieved by minimizing the solar cell area combined with light concentration. Micrometer-sized chalcopyrite-based solar cells, specifically, $Cu(In_x,Ga_{1-x})Se_2$ (*CIGSe*), have the potential to reduce cost by integrating optical elements to concentrate sunlight into the cell. Furthermore, by minimizing the solar cell area a huge material saving could be accomplished, but one of the most important achievements of the reduction of the cell area, for CPV applications, is the dramatic reduction of the temperature of the solar cell under concentrated illumination. Due to the advantages offered by miniaturization of the cell area, micrometer-sized solar cells for concentrator photovoltaics are becoming widespread.

Thermal management of heat under concentrated light for micrometer-sized solar cells, specifically, CIGSe solar cells, was briefly reported by Sadewasser *et al.* [24] and was demonstrated in great detail by the author in [13], proving the advantages of cell minimization.

Improved heat dissipation could be extended to other material-based solar cells by adjusting the thermal properties in the thermal model [13]. As an example of cell miniaturization, Albert *et al.* [25] and Gu *et al.* [26] implemented sub-millimeter multi-junction III-V-based solar cells and micro-scale wafer-integrated CPV devices, respectively. Furthermore, in order to access the benefits of the miniaturization of the cell area with concentrated light, some companies are scaling down their products [27] [28], for III-V-based technology, to reduce cost and take advantage of this profitable trend.

Regarding chalcopyrite-based solar cells, specifically, CIGSe technology, only few authors reported remarkable power conversions to electricity by using micrometer-sized solar cells under concentrated light. Lotter *et al.* [29], one of our partners in the European project called *"Cheetah"* for the development of micrometer-sized CIGSe devices, reported an absolute and relative increment of 4.5% and 19.5%, respectively, compared to the performance of the cell under standard test conditions. However, these results were carried out for rectangular-shaped shaded solar cells, where the active area of the solar cell is partially shaded and, therefore, there is no real material saving. On the other hand, previous investigations were carried out via top-down fabrication approaches, using high quality absorbers, which were scaled down to micrometer-sized solar cells. One of the researches that has contributed more to the development of micrometer-sized CIGSe solar cells for CPV applications has been Paire *et al.* [30] [31] [32]. Paire *et al.* reported great results with micrometer-scale CPV prototypes but without a realistic interpretation of why the minimization of the active area can achieve unthinkable results with respect to macroscopic device under concentrated light. Additionally, others authors, such as Reinhold *et al.* [33], Sadewasser *et al.* [24] or Heidmann *et al.* [34], developed either via top-down or bottom-up approaches by using high quality material or in early stage low quality material micrometer-sized CIGSe solar cells for concentrator photovoltaics.

1.2. Objectives

The aim of this Thesis is to investigate micrometer-sized $Cu(In_x,Ga_{1-x})Se_2$ (*CIGSe*) solar cells for concentration purposes. In previous literature, respective to micrometer-scale CPV devices, the research community developed micrometer-sized devices without going deeper into the real circumstances and causes which emphasized the benefits of cell miniaturization. The objectives of this Thesis can be summarized in:

- To investigate the thermal behavior of micrometer-sized CIGSe solar cells under concentrated light. For this purpose, the temperature of the solar cell under concentrated light is investigated in detail by using finite element analysis software [35] for different structures, light concentrations and distributions. Special interest is given to the heat management in the micrometer-scale under concentrated light.

- To fabricate and characterize micrometer-sized CIGSe solar cells for concentration purposes. Proofs of concept were developed via the so-called "*top-down approach*" and characterized by different techniques, especially, current-voltage characterization under concentrated light to obtain the basic output parameters as a function of the irradiation.

- To simulate the basic output parameters of micrometer-sized CIGSe solar cells under concentrated light taking into account the thermal and opto-electronic properties obtained before by using finite element analysis software. A thermal-opto-electronic (*TOE*) model of the fabricated devices was investigated in detail. The aim is to compare the experimental results with the simulated ones and forecast improvements and limitations of this technology.

1.3. Outline of this Thesis

This manuscript is divided in three main sections. The first one, Chapter 2, comprises the theoretical basis and assumptions assumed necessary for the comprehension of the simulations and measurements carried out in this work. Specifically, the second chapter focuses on the thermal simulation properties, current-voltage characterization physics and thermal-opto-electronic simulations.

The second block comprises Chapters 3 and 6. They are focused on the simulation of micrometer-sized CIGSe solar cells under different concentration factors and irradiation profiles by using finite element analysis software. Chapter 3 aims at being the main reinforcement of the benefits of solar cell miniaturization. Furthermore, Chapter 3 summarizes the advantages of the use of micrometer-sized solar cells for concentration purposes due to the better heat management. This chapter is dedicated exclusively to the study of the temperature evolution with concentrated light inside of the solar cell. Moreover, Chapter 3 provides the theoretical basis of heat management to continue and encourage the development of micrometer-sized CIGSe solar cells. Therefore, this chapter is separated from the main block of simulations, Chapter 6, and prior to the development and fabrication of solar cells. The results obtained in this chapter greatly promoted the development of micrometer-sized CIGSe solar cells, and therefore, the manufacture of these devices is described in the following chapters, specifically, in Chapter 4 and 5.

In addition, Chapter 6 is intended to reproduce and simulate exactly the experimental part (Chapters 4 and 5) including the heat management and the opto-electronic properties of the fabricated and characterized solar cells. The sixth chapter is intended to further understand the benefits and limitation of cell miniaturization under concentrated light based on the current fabrication techniques. Furthermore, the results and tendencies obtained are also compared with the measurements carried out in Chapter 5. In addition, this chapter is located at the end of this work since it is based on the results obtained in the thermal studies and in the opto-electronic properties stemmed from the characterization of the solar cell fabricated previously in Chapter 4 and 5.

The experimental part, third section, comprises Chapter 4 and 5. The first is focused on the description of the step-by-step process from the growth of micrometer-sized CIGSe solar cells in the so-called "*top-down approach*". Namely, Chapter 5 describes the different characterization techniques applied to the micrometer-sized CIGSe solar cells and the experimental results obtained. These morphological, elemental composition and distribution results as well as the electrical parameters are described in the fifth chapter and used in the thermal-opto-electronic simulations performed in Chapter 6.

Finally, Chapter 7 points out the main and general conclusions achieved along these chapters while indicating the current limitations and further improvements of this technology presented in this Thesis.

Chapter 2:

Physics

2.1. Introduction

This chapter presents the theoretical basis and a detailed explanation of the assumptions assumed necessary for the comprehension of the simulations and measurements carried out in the following chapters.

2.2. Thermal simulation properties

In the following chapter, different simulations were carried out to determine the temperature effect of the different model elements. Parameters such as substrate thickness, back contact thickness, substrate area, back contact area, absorber area and back contact material were investigated as a function of light concentration with the finite element method (*FEM*) software. Solar cell temperature evolution upon concentration was determined for the different structure modifications.

Thermal properties applied to the different materials used during the thermal simulations are summarized in Table 2.1. The values used in the simulations were based on previous literature and material databases from the FEM software [13] [35] [36] [37]. Moreover, the same thermal properties were selected for the intrinsic ZnO and for the aluminum-doped zinc oxide ($ZnO:Al_2O_3$ 1.5wt.%) layers. The author included and simulated both layers in case that in future works it is desired to modify these values without changing the structure of the thermal model. Note that the thermal parameters of the metal grid refer to a layer composed of nickel. This assumption, instead of a double layer composed of nickel and aluminum, was selected for simulations purposes. The results obtained from the thermal simulations with this layer only will

provide a slightly lower temperature of the solar cell under different circumstances compared with the inclusion of a double layer due to the higher thermal conductivity and emissivity of nickel with respect to aluminum. The selected thicknesses of the layers were determined by the deposition technique as described in Chapter 4. It should be noted that the insulation layer is orders of magnitude larger than the others. However, due to the fabrication process, the selected photoresist and the facilities available, an electrically thinner insulating layer was not possible to perform (see section 4.2.6). Conduction, convection and radiation (*CCR*) fundamental heat transfer modes were included. In the ideal case, an active cooling system was considered keeping the back side at 20°C. However, in the realistic case study no active cooling was implemented but a CCR heat dissipation mechanism was incorporated. A surrounding air gap kept at 20°C was set as boundary condition for CCR heat exchange.

Table 2.1:
Material properties used for the modeling based on [13] [35] [36] [37].

Parameter	Units	Glass substrate	Back contact	CIGSe	Isolation	Buffer layer	i-ZnO	Front contact	Metal grid	Glass cover
Thickness	nm	$3{\cdot}10^6$	800	$2{\cdot}10^3$	$8{\cdot}10^3$	50	130	320	$2{\cdot}10^3$	$1{\cdot}10^6$
Density	kg/m^3	2210	Mo 10200 Cu 8960	5700	2650	5700	5606		8192	2210
Emissivity	-	0.87	Mo 0.2	0.87	0.87	0.87	0.87		0.12	0.87
Thermal conductivity	W/(m·K)	1.4	Mo 250 Cu 400	5	1.7	5	50		6.5	1.4
Heat capacity	J/(kg·K)	730	Mo 138 Cu 385	325	730	325	505		444	730
Convective heat transfer coefficient	W/(m·K)	10.45	-	-	-	-	-	10.45	10.45	10.45

Physics used by the finite element software for the fundamental heat mechanism and boundary conditions were as follows [38]. Thermal conduction heat transfer equation:

$$\rho \cdot C_p \cdot \frac{\partial T}{\partial t} + \nabla \cdot (-k \cdot \nabla T) = Q \qquad \text{[38] (2.1)}$$

where $\boldsymbol{\rho}$ is the material density, C_p and k represent heat capacity and thermal conductivity, respectively, T is the solar cell temperature, and Q is the heat source energy. Thermal radiation heat transfer equation:

$$\varepsilon \cdot \sigma \cdot \left(T_{amb}^4 - T^4\right) = q \qquad \text{[38] (2.2)}$$

where ε and σ represent emissivity and Stefan-Boltzmann constant, respectively. *T* and T_{amb} are the solar cell and ambient temperature, respectively, and *q* is the heat flux. The convective heat transfer equation:

$$h \cdot (T_{amb} - T) = q_0 \quad \text{[38] (2.3)}$$

where *h* represents the conductive heat transfer, T_{amb} and *T* are solar surrounding and cell temperature, and q_0 is the inward heat flux. Surrounding device temperature was selected to be invariable with time and exchanged heat. Therefore, T_{amb}, which stand for the temperature at a distance from the model, was set at 20°C and *h*, which represents the thermal physics occurring between the boundary and T_{amb}, was considered as the conductive heat transfer coefficient. The boundary conditions of the simulation domain fulfill the equation:

$$-\boldsymbol{n} \cdot \boldsymbol{q} = q_0 \quad \text{[38] (2.4)}$$

where $\boldsymbol{n}$ is the normal vector of the boundary, $\boldsymbol{q}$ and q_0 represent heat flux vector and inward heat flux, respectively.

The heat source was applied on the upper surface of the absorber (*CIGSe*) and is partially absorbed in this region based on the simulation approaches. A planar heat source (units: W/m^2) was used instead of a volumetric heat source (units: W/m^3) at the p-type material. The light beam will lose intensity due to absorption and scattering when the beam passes through the solar cell. The absorption of light will not be homogeneous along the cell [39] and a volumetric heat source is therefore not suitable to be used in this study.

The meshing of the desired structure employed a maximum element size of 0.14 mm and a minimum element size of 0.006 mm using a free tetrahedral entity for the geometry. For smaller structures, the FEM adapt the structure to fit enough free tetrahedral elements inside of the layer.

In the ideal case, the solar device was properly and actively cooled to dissipate undesired heat generated with increasing concentration. Hence, the basic model was stacked on a cooling device kept at room temperature (*20°C*) and other heat dissipation mechanisms were not taken into account to simplify the model. Although, including fundamental heat transfer modes:

conduction, convection and radiation (*CCR*), the temperature deviation remains below 0.3%. Hence, the CCR contributions were neglected in the basic model.

Heat management benefits of micrometer-sized solar cells under outdoor operation conditions were analyzed. Furthermore, no active cooling was induced but conduction, convection and radiative heat transfer mechanism were considered in the realistic simulation model. The CCR heat exchange was performed supposing an air surrounding media kept at room temperature.

The concentration factor *C* applied on the model was defined as follows:

$$C = \frac{Area_{substrate}}{Area_{solar\ cell}} \tag{2.5}$$

where $Area_{solar\ cell}$ and $Area_{substrate}$ are the solar cell and substrate area, respectively. Hence, the incoming solar cell irradiance was defined as the concentration factor multiplied by the sun irradiance under standard test conditions (*AM1.5G, 1000 W/m*^{2}). Nevertheless, partial absorption and conversion to heat of the AM1.5G spectrum at the pn-junction was assumed.

Reflection of the different medium was included in the model. However, in a first approximation, the effect of multiple reflections of light in the selected stack of layers was not taken into account, but the first reflection at each individual interface was deducted to the incoming light. Nevertheless, multiple reflections have been considered and implemented in the thermal-opto-electronic model. The reflected power for the different interfaces during the simulations were 8.2%, 4.0%, 0.8%, 6.3% and 1.2% of the incoming light for the Air/AZO, Air/BSG, BSG/AZO, AZO/CIGSe and CIGSe/Mo hetero-interfaces, respectively. The interfaces through the light beam needs to travel for the ideal case were Air/AZO/CIGSe/Mo and for the realistic model were Air/BSG/AZO/CIGSe/Mo. Reflected light at the CIGSe/Mo interface was included as an extra heat source at the absorber layer. Thereby, a 13.2% and a 9.9% of the total beam power was reflected for the basic model and for the realistic one, respectively.

Moreover, sub-band gap energy photons and UV light will not be completely absorbed [39]. Depending on the Ga content, the CIGSe absorber band gap could fluctuate from 1.04 to 1.68 eV [40] determining the maximum amount of energy absorbed by the solar cell. Glow-discharge

optical emission spectroscopy (*GDOES*) characterization of our fabricated solar cells showed an averaged band gap value of 1.185 $\pm$ 0.000(4) eV (see Chapter §5), which was assumed in the subsequent simulations and calculations. Therefore, non-absorber sub-band gap and UV photons were 10.2% and 7.7% of the incoming power, respectively, and will not contribute to heat generation. Besides the solar cell spectral response and the sun spectrum, the maximum light absorption will be 819 W/m^2.

Additionally to the non-absorbed light loses, power conversion to electricity was included in the model. HZB co-evaporation reference solar cells performance present a 16% light conversion to electricity (see Chapter §5) which was taken into account in the following simulations.

Joule heating produced by the passage of the generated PV current through its intrinsic resistance: series and shunt resistance was considered in the model. Solar cell absorbed light converted to electricity will decrease the amount of heat generation, although the ohmic heating contribution will increase cell heating. Joule heating power with concentration remains below 3% of the incoming power due to a reduction of the intrinsic resistance with concentrated light (see Chapter §5).

Taking into account the total light reflection, sub-band gap and UV non-absorbed photons, the power conversion to electricity and the Joule heating contribution, the reference irradiance applied to the basic case and to the realistic one was 600 W/m^2 and 620 W/m^2, respectively. The maximum cell temperature was analyzed for different concentration factors and structure modifications supported by prior considerations.

2.3. Photoluminescence characterization physics

Photoluminescence measurements consist in the detection of the emission of light from a material, in this case a solar cell, which is excited with a light source previously. The thermal equilibrium state of the solar cell or absorber is disturbed by the incoming illumination with an energy larger than the band gap energy. In a typical photoluminescence measurement, by illuminating the absorber with light of sufficient energy, electrons and holes are formed in the conduction and valence bands, respectively, once the photons are absorbed. The recombination

of electrons from higher electronic states with holes from vacant states caused the emission of light. This emission of light, for a high injection regime of photons, depends on the radiative recombination of the material in study. The photon flux, assuming homogenous material properties, flat bands for the quasi-Fermi levels and a narrow emission distribution through the material surface, is defined as:

$$PL_{yield}(E) = \frac{1}{4 \cdot \pi^2 \cdot \hbar^3 \cdot c^2} \cdot \frac{a(E) \cdot E^2}{e^{\left(\frac{(E-\Delta\mu)}{k_B \cdot T}\right)} - 1} \quad [41]\ (2.6)$$

where E represents the photon energy, $a(E)$ and $\Delta\mu$ are the absorptivity and the quasi-Fermi level splitting, respectively. h refers to the Planck constant and c, k_B and T are the speed of light, the Boltzmann constant and the temperature of the material, respectively. The absorptivity is defined as:

$$a(E) = \left(1 - R_f\right) \cdot \left(1 - e^{(-\alpha(E) \cdot d)}\right) \quad [41]\ (2.7)$$

where R_f, $\alpha(E)$ and d are the reflectivity of the front surface of the material, absorption coefficient and the absorber thickness, respectively.

The determination of the photoluminescence yield relies on the knowledge of the optical constants of the material under study. However, the most usual is to ignore these parameters. Therefore, one of the common assumptions is to assume that the absorptivity is constant and equal to unity. By simplifying the dependence of the photon flux with the photon energy, the quasi-Fermi level splitting can be estimated by fitting the high-energy wind of the dependence of the natural logarithm of natural logarithm of PL_{yield}/E^2 versus the photon energy (E). Then, Equation 2.6 can be rewritten to estimate the quasi-Fermi level splitting as:

$$ln\left(\frac{PL_{yield}(E)}{A \cdot E^2}\right) = -\frac{(E-\Delta\mu)}{k_B \cdot T} \quad [41]\ (2.8)$$

where A is a constant, to estimate the value of the quasi-Fermi level splitting and therefore, the maximum achievable open-circuit voltage in the material. For finished solar cells, the open-circuit voltage was expected to be similar to the value of the quasi-Fermi level splitting.

2.4. Current-voltage characterization physics

Solar cells convert light into electrical current. Such devices are called photodiodes (i.e. semiconductors devices), which generate electricity from photons by using the photoelectric effect. A semiconductor diode, usually a pn heterojunction, contains two adjoining semiconductors: a hole excess (*p-type*) and an electron excess (*n-type*) material. These photodiodes allow or hinder the current conduction in a certain direction. By applying light and an external load between the terminals, the photo-generated current can be extracted. Considering the one-diode model circuit shown in Figure 2.2 as representative of the typical behavior of CIGSe solar cells, the basic parameters of the device were determined. A more sophisticated model can be used by including a second ideal-diode in the electrical circuit [42].

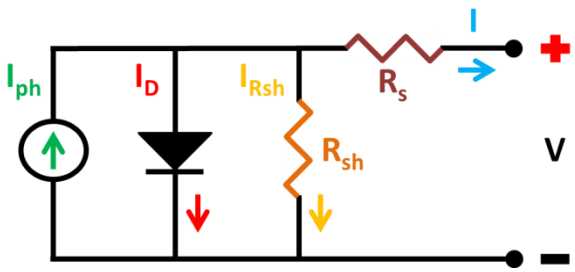

Figure 2.2: One-diode model diagram: (from left to right) photo-generated current, current source symbol, diode current, ideal-diode symbol, shunt resistance current, shunt resistance symbol, series resistance symbol, series resistance, extracted current, terminal voltage and device connections (positive and negative).

Applying Kirchhoff's current law, based on the principle of charge conservation, the extracted current is defined as:

$$I = I_{ph} - I_D - I_{Rsh} \qquad [42]\ (2.9)$$

where I_{ph}, I_D, I_{Rsh}, and I are the photo-generated current, the current through the ideal-diode and through the shunt resistance and finally, the extracted current, respectively.

The complete equation of the equivalent circuit of the one-diode model for CIGSe solar cells, which relates the output current and voltage of the photodiode in operation, is as follows:

$$I = I_{ph} - I_o \cdot \left(e^{\left(\frac{q \cdot (V + I \cdot R_S)}{n \cdot k_B \cdot T} \right)} - 1 \right) - \frac{(V + I \cdot R_S)}{R_{sh}} \qquad [42]\ (2.10)$$

where I_o represents the dark current of the diode, R_{sh} and R_s are the shunt and series resistance, respectively. V refers to the terminal voltage and q, n, k_B and T are the elementary charge constant, the ideality factor of a diode, the Boltzmann constant and the temperature of the heterojunction, respectively.

The current-voltage (*I-V*) characteristic of a solar cell determines the macroscopic parameters of the device. The non-linear dependence of the output current and voltage is shown in Figure 2.3. The dark I-V characteristic curve was obtained by biasing the solar cell with forward and backward voltages in absence of light. In the same manner, the I-V characteristic curves under illumination were performed. Usually, in the photovoltaic research field, the representation of the I-V characteristics curves are inverted for visual purposes (Figure 2.3, quadrant IV). The author will follow this trend and will show the measured and simulated I-V characteristics curves accordingly.

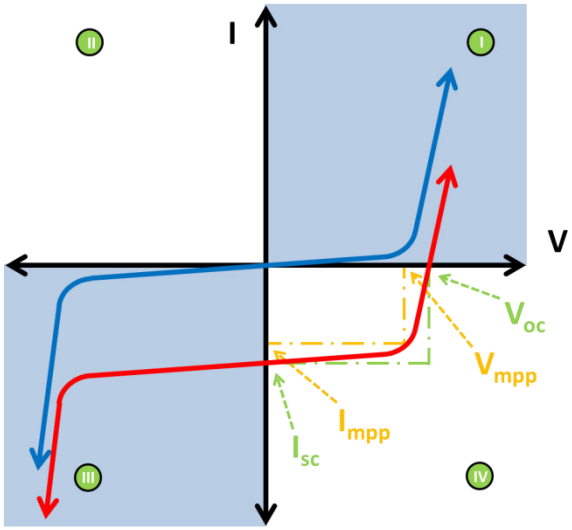

Figure 2.3: I-V characteristic curve of a solar cell. The dark (blue) and under illumination (red) curves are shown. Short-circuit current (I_{sc}), open-circuit voltage (V_{oc}), maximum power point current (I_{mpp}) and maximum power point voltage (V_{mpp}).

The basic parameters of the device are obtained from the dark and illuminated I-V characteristic curves. By measuring the current-voltage dependence with light, different parameters can be obtained. The short-circuit current (I_{sc}) is defined as the net current flowing through the diode when the terminal voltage is zero:

$$I_{sc} = I = I_{ph} - I_o \cdot \left(e^{\left(\frac{q \cdot I_{SC} \cdot R_S}{n \cdot k_B \cdot T}\right)} - 1 \right) - \frac{I_{SC} \cdot R_S}{R_{sh}} \quad \text{[42] (2.11)}$$

The open-circuit voltage (V_{oc}) is defined as the voltage obtained at the terminal contacts when the net current is zero under illumination:

$$0 = I = I_{ph} - I_o \cdot \left(e^{\left(\frac{q \cdot V_{OC}}{n \cdot k_B \cdot T}\right)} - 1 \right) - \frac{V_{OC}}{R_{sh}} \quad \text{[42] (2.12)}$$

An approximation for the open-circuit voltage assuming a high shunt resistance can be adopted:

$$V_{oc} \cong \left(\frac{n \cdot k_B \cdot T}{q}\right) \cdot \ln\left(\frac{I_{SC}}{I_o} + 1\right) \quad \text{[42] (2.13)}$$

Other basic parameters can be extracted from the I-V characteristics curves. The maximum power available from an illuminated solar cell provides the maximum power point current (I_{mpp}) and voltage (V_{mpp}). The fill factor determines the ratio between the maximum power available and the theoretical maximum power delivered from the solar cell, which corresponds to the product of the short-circuit current and the open-circuit voltage:

$$FF = \frac{I_{mpp} \cdot V_{mpp}}{I_{sc} \cdot V_{oc}} \quad \text{[42] (2.14)}$$

The most important basic parameter of a solar cell is the capability to convert light into electrical current. The efficiency (η) is defined as the ratio of the maximum energy provided and the incident energy:

$$\eta = \frac{I_{SC} \cdot V_{OC} \cdot FF}{P_{in}} \quad \text{[42] (2.15)}$$

Due to the different amount of solar cells developed in the past and the different spectral absorptions, solar cells, intended to be compared, need to be measured in the same conditions. For terrestrial applications, two standards (*ASTM G-173* [43]) were defined for solar cells comparisons. The AM1.5 Global (*AM1.5G*) spectrum and the AM1.5 Direct + Circumsolar (2.5°) (*AM1.5D*) spectrum were determined for flat modules and for solar concentrator applications, respectively. Both standards corresponds to the terrestrial irradiation at a zenith angle of 48.19°, representative of the illumination of the central region of Europe. The integrated power

density for each spectrum is 1000 W/m^2 for the AM1.5G and 900 W/m^2 for the AM1.5D. For comparison purposes, between different opto-electronic characterizations, all samples in this work were measured by using the AM1.5G standard spectrum and a device temperature of 20°C.

The dependence of the basic parameters of a photodiode with temperature and under concentrated light is detailed below. If a concentration factor *C* is applied to a solar cell, the photo-generated current is expected to growth linearly by this factor:

$$I_{ph}(C) = C \cdot I_{ph}(AM1.5G) \qquad [42]\ (2.16)$$

Assuming a long-base semiconductor heterojunction, where the diffusion lengths (L_n and L_p, in *n* and *p* regions, respectively) of minority carriers in the semiconductor base are shorter than the base thickness (W_P), the dark current is:

$$I_o = q \cdot A \cdot \left(\frac{D_n}{N_A \cdot L_n} + \frac{D_p}{N_D \cdot L_p}\right) \cdot n_i^2 \qquad for \qquad L_n, L_p \ll W_P \qquad [42]\ (2.17)$$

$$L_n = \sqrt{D_n \cdot \tau_n} \qquad L_p = \sqrt{D_p \cdot \tau_p} \qquad [42]\ (2.18)$$

where n_i is the intrinsic carrier concentration, N_A and N_D are the density of acceptor and donor atoms, respectively. D_n and D_p correspond to the minority-carrier (h^+ and e^-, respectively) diffusion coefficients and τ_n and τ_p are the minority-carrier (h^+ and e^-, respectively) recombination lifetimes:

$$n_i = 2 \cdot \left(m_n^* \cdot m_p^*\right)^{3/4} \cdot \left(\frac{2 \cdot \pi \cdot k_B \cdot T}{h^2}\right)^{3/2} \cdot e^{-\frac{E_G(T)}{2 \cdot n \cdot k_B \cdot T}} \qquad [42]\ (2.19)$$

Here, the effective masses m_n^* and m_p^* will be taken not to depend of the temperature [42].

$$E_G(T) = E_G(0) - \frac{\alpha \cdot T^2}{T + \beta} \qquad [42]\ (2.20)$$

where E_G represents the energy difference between the valence band and the conduction band, α and β are specific constants of a semiconductor device [44]. The dark current dependence with temperature is:

$$I_o(T) = q \cdot A \cdot \left(\frac{D_n}{N_A \cdot L_n} + \frac{D_p}{N_D \cdot L_p}\right) \cdot n_i^2 =$$

$$= q \cdot A \cdot \left(\frac{D_n}{N_A \cdot L_n} + \frac{D_p}{N_D \cdot L_p}\right) \cdot \left(2 \cdot \left(m_n^* \cdot m_p^*\right)^{3/4} \cdot \left(\frac{2 \cdot \pi \cdot k_B \cdot T}{h^2}\right)^{3/2} \cdot e^{-\frac{E_G(T)}{2 \cdot n \cdot k_B \cdot T}}\right)^2 =$$

$$= q \cdot A \cdot \left(\frac{D_n}{N_A \cdot L_n} + \frac{D_p}{N_D \cdot L_p}\right) \cdot 4 \cdot \left(m_n^* \cdot m_p^*\right)^{3/2} \left(\frac{2 \cdot \pi \cdot k_B}{h^2}\right)^3 \cdot T^3 \cdot e^{-\frac{E_G(T)}{n \cdot k_B \cdot T}} = B \cdot T^3 \cdot e^{-\frac{E_G(T)}{n \cdot k_B \cdot T}}$$

[42] (2.21)

The open-circuit voltage dependence with temperature is:

$$V_{oc}(AM1.5G, T) \cong \left(\frac{n \cdot k_B \cdot T}{q}\right) \cdot \ln\left(\frac{I_{sc}(C,T)}{I_o(T)} + 1\right) \approx \left(\frac{n \cdot k_B \cdot T}{q}\right) \cdot \ln\left(\frac{I_{sc}(C,T)}{B \cdot T^3 \cdot e^{-\frac{E_G(T)}{n \cdot k_B \cdot T}}}\right) =$$

$$= \left(\frac{n \cdot k_B \cdot T}{q}\right) \cdot \left[\ln\left(I_{sc}(C,T)\right) - \ln\left(B \cdot T^3 \cdot e^{-\frac{E_G(T)}{n \cdot k_B \cdot T}}\right)\right] = \frac{E_G(T)}{q} - \left(\frac{n \cdot k_B \cdot T}{q}\right) \cdot \ln\left(\frac{B \cdot T^3}{I_{sc}(C,T)}\right)$$

[42] (2.22)

Therefore, the current-voltage dependence of the solar cell with temperature and under concentrated light is:

$$I(C,T) = I_{ph}(C) - I_o(T) \cdot \left(e^{\left(\frac{q \cdot \left(V(C,T) + I(C,T) \cdot R_s(C)\right)}{n \cdot k_B \cdot T}\right)} - 1\right) - \frac{\left(V(C,T) + I(C,T) \cdot R_s(C)\right)}{R_{sh}(C)}$$

[42] (2.23)

The series and shunt resistance dependence with concentration were determined experimentally in this work. Paire *et al.* [31] described a more sophisticated model for the total series resistance as a function of the incident light power and the device temperature. However, further investigations rejected *Paire's* model [45] by providing results close to those presented in this work:

$$R_s(C) \cdot C \cdot I_{sc}(AM1.5G, T) = \left(\frac{n \cdot k_B \cdot T}{q}\right) \quad \text{[45] (2.24)}$$

The short-circuit current increases linearly with concentration as shown:

$$I_{sc}(C,T) = I_{ph}(C) - I_o(T) \cdot \left(e^{\left(\frac{q \cdot I(C,T) \cdot R_s(C)}{n \cdot k_B \cdot T}\right)} - 1 \right) - \frac{I(C,T) \cdot R_s(C)}{R_{sh}(C)} \approx C \cdot I_{sc}(AM1.5G,T)$$

[42] (2.25)

And finally, the open-circuit voltage increases with the logarithm of the concentration:

$$V_{oc}(C,T) = \left(\frac{n \cdot k_B \cdot T}{q}\right) \cdot \ln\left(\frac{I_{sc}(C,T)}{I_o(T)} + 1\right) \approx \left(\frac{n \cdot k_B \cdot T}{q}\right) \cdot \ln\left(\frac{C \cdot I_{sc}(AM1.5G,T)}{I_o(T)}\right) =$$

$$= V_{oc}(AM1.5G,T) + \left(\frac{n \cdot k_B \cdot T}{q}\right) \cdot \ln(C) \quad \text{[42] (2.26)}$$

The ideality factor through current-voltage measurements as a function of the temperature of solar cell and the selected illumination can be determined with the help of the prior equation. By fitting the dependence of the natural logarithm of $I_{sc}(C,T)/I_o(T)$ versus the open-circuit voltage assuming ideal series and shunt resistances, the ideality factor can be estimated. For different concentration factors where the exact temperature of the solar cell is unknown, temperature variations will influence the estimated value of the ideality factor. However, the temperature evolution with concentration was assumed constant to determine the ideality factor, even when this dependence was supposed to affect not only the open-circuit voltage, but also the fill factor, the conversion efficiency and to a lesser extent the short-circuit current density.

From the estimated values of the ideality factor, the activation energy (E_A) can be determined. Two different methods were investigated. The activation energy can be extracted from Equation 2.22 as a function of the temperature and open-circuit voltage by assuming that the activation energy at room temperature is equal to the band gap of the solar cell. On the other hand, by fitting the Arrhenius equation:

$$k = A \cdot e^{\left(\frac{-E_A}{n \cdot k_B \cdot T}\right)} \quad \text{[46] (2.27)}$$

where *k* represents the reaction rate constant. *A* refers to the Arrhenius pre-exponential factor, *n*, k_B and *T* are the ideality factor of a diode, the Boltzmann constant and the temperature of the solar cell. This formula resembles the equation used to describe the current through a semiconductor in the absence of illumination. Therefore, variables *k* and *A* can be exchanged for the net current flowing through the diode (*I*) and the dark current of the diode (I_o), respectively, to estimate the activation energy of the material under study:

$$I = I_o \cdot e^{\left(\frac{-E_A}{n \cdot k_B \cdot T}\right)} \quad \text{[46] (2.28)}$$

2.5. Thermal-opto-electric simulation properties

To obtain accurate simulation results, the 3D model was composed of different units: optical, thermal and electrical modules. All units were linked with a multi-physics toolbox included in the finite element method (*FEM*) software [35]. The optic module was used to estimate the overall solar cell absorption through the study of the electromagnetic wave propagation in optical media. Material heating and heat management due to an energy source were investigated using the heat transfer module (see Chapter §3). Finally, the use of the semiconductor module was applied to calculate the stationary charge carrier transport equations under different concentration factors.

The total absorption for each layer [47] was calculated by applying the AM1.5G solar spectrum normal to the device surface (Further details in Appendix III-1). The generation rate (G_{rate}) for each wavelength (λ) was obtained by calculating the incident photon flux (Φ_s), the total incident power (P_{in}) and the volume power density (Q_{abs}).

$$G_{rate}(x, y, z, \lambda) = \frac{\Phi_s(\lambda)}{P_{in}(x,y)} \cdot Q_{abs}(x, y, z, \lambda) \quad (2.29)$$

where Q_{abs} is the deposited power of the incident rays per unit volume (V_{abs}) of the mesh elements,

$$Q_{abs}(x, y, z, \lambda) = \frac{1}{V_{abs}} \sum_{i=1}^{n} \frac{\partial Q_{abs,i}(x,y,z,\lambda)}{\partial t} \quad (2.30)$$

This amount of deposited ray power $Q_{abs,i}$ can be written as a function of the electric field (E) within the layer as follows,

$$Q_{abs,i}(x,y,z,\lambda)\ \alpha\ |E(x,y,z,\lambda)|^2 \tag{2.31}$$

The total generation rate along the whole device was calculated by integrating over the wavelength spectrum of interest, in this case for CIGSe solar cells, from 300 nm to 1200 nm,

$$G_{rate}(x,y,z) = \int_{300\ nm}^{1200\ nm} G_{rate}(x,y,z,\lambda)\cdot d\lambda \tag{2.32}$$

The spatial generation rate and the integrated power over the AM1.5G spectrum were considered to increase linearly with concentrated light (C),

$$G_{rate}(x,y,z,\lambda,C) = C\cdot G_{rate}(x,y,z,\lambda) \tag{2.33}$$

and no spectral inhomogeneities were taken into account,

$$G_{rate}(z,\lambda) = G_{rate}(x,y,z,\lambda) \tag{2.34}$$

Therefore, the calculated generation rate along the device was supposed to increase linearly with concentration. Consequently, the generation rate divided by the irradiance will be equal to the generation rate calculated at standard test conditions. The generation rate was assumed to change in the z component but to remain identical in x and y axis.

The Poisson equation, continuity equations, as well as the drift and diffusion current equations were considered in the semiconductor simulations. The electrostatic potential (Φ) for a given charge distribution (ρ) in semiconductor devices was calculated through Poisson´s equation,

$$\vec{\nabla}\cdot\hat{\varepsilon}\cdot\vec{\nabla}\Phi = -\rho \tag{2.35}$$

where $\hat{\varepsilon}$ is the permittivity tensor, which can be considered as a scalar (ε) . The space charge density is defined as:

$$\rho = q\cdot\left(p - n + N_D - N_A + \rho_p - \rho_n\right) \tag{2.36}$$

where q is the elementary charge, p and n are the hole and electron concentrations, respectively. N_D and N_A refer to the donor and acceptor impurities, respectively, and p_p and p_n are the trapped carrier densities for holes and electrons, respectively. The continuity equations for charged impurities, electrons and holes, can be written as:

$$\vec{\nabla} \cdot \overrightarrow{J_n} - q \cdot \frac{\partial n}{\partial t} - q \cdot \frac{\partial p_n}{\partial t} = q \cdot (G_{rate} - R_{rate}) \tag{2.37}$$

$$\vec{\nabla} \cdot \overrightarrow{J_p} + q \cdot \frac{\partial p}{\partial t} + q \cdot \frac{\partial p_p}{\partial t} = -q \cdot (G_{rate} - R_{rate}) \tag{2.38}$$

where R_{rate} refers to the recombination rate. Continuous quasi-Fermi levels were set as boundary condition for the continuity equations. Recombination mechanisms were included in the simulations. In CIGSe solar cells the dominant recombination through defects is driven by Shockley-Read-Hall (*SRH*) trap-assisted recombination [48] [49] [50]. SRH recombination mechanism is the predominant recombination mechanism due to the multi-crystalline nature of the absorber. The Shockley-Read-Hall recombination is defined as:

$$R_{rate} = R_{SRH} = \frac{p \cdot n - N_i^2}{\tau_p \cdot (n + N_i) + \tau_n \cdot (p + N_i)} \tag{2.39}$$

where τ_n and τ_p are the electrons and holes lifetimes, respectively, and N_i refers to the intrinsic carrier concentration at equilibrium.

Furthermore, EDX analysis and PL measurements pointed to the presence of a strongly localized recombination mechanism at the cell edge (see Chapter §5, section 5.3.2.1 and 5.3.3.1). Therefore, the perimeter was affected by the etching process. For simulations purposes, a SRH recombination rate greater than in the CIGSe bulk material was settled to the cell perimeter. The lifetime value implemented along the perimeter was 10^{-1}x lower than the lifetime for the bulk absorber.

The electric current for electrons and holes can be expressed in terms of the drift and diffusion of charge carriers as:

$$\overrightarrow{J_n} = q \cdot n \cdot \mu_n \cdot \vec{E} + q \cdot D_n \cdot \vec{\nabla} n \qquad \overrightarrow{J_p} = q \cdot p \cdot \mu_p \cdot \vec{E} - q \cdot D_p \cdot \vec{\nabla} p \tag{2.40}$$

where μ_n and μ_p are the carrier mobilities for electrons and holes, respectively, and D_n and D_p refer as the diffusion coefficients for electrons and holes, respectively.

$$D_n = \frac{k_B \cdot T}{q} \cdot \mu_n \qquad\qquad D_p = \frac{k_B \cdot T}{q} \cdot \mu_p \tag{2.41}$$

The solar cell temperature was selected according to the output of the thermal module as detailed in Chapter §3.

Chapter 3:

Thermal simulations

3.1. Introduction

Besides the strengths of CPV technology: high efficient devices, high concentration factors, stable energy production due to tracking capabilities and low payback time [51], concentrator photovoltaics have different weaknesses. As an example, countries with low direct normal irradiance (*DNI*) are not suitable for CPV applications because the lens system cannot focus light into the solar cell. Furthermore, high concentration systems need high tracking accuracy and frequent cleaning not to mitigate PV performance. But the main factor reducing the overall performance is the cell temperature working regime. Heat dissipation and cell temperature have demonstrated a high impact on the design of CPV systems. Active cooling is required for PV with high concentration factors increasing the module cost and the maintenance routines. Micrometer-sized solar cells were previously analyzed by Paire *et al.* [30] and Nielson *et al.* [52] showing the good disposition to enhance efficiency and to boost the cell performance with concentrated light. Sadewasser *et al.* [24] demonstrate lightly the benefits of reducing cell size for concentration purposes. However, there has been no detailed micrometer-sized solar cell temperature study, to corroborate the advantages of reducing cell size and increasing concentration factor. To understand in more depth the advantages of cell minimization, it is essential that a thermal study of the solar cell behavior under concentrated light is investigated. Hence, prior to develop and fabricate a real device, the heat management of the desired devices under different circumstances was researched.

3.2. Model structure

The hypothesis that micrometer-sized CIGSe solar cells offer improved heat dissipation needs to be demonstrated. To undertake this enterprise, the PV cell temperature behavior will be analyzed under different conditions and concentration factors using finite element analysis software [35].

Investigative simulations were carried out, varying different structure elements, to find out the best configuration for high concentration ratios. To accomplish these simulations, the simplest scenario was firstly taken into account and its complexity was gradually increased.

The basic structure (Figure 3.1a) was designed according to photovoltaic large scale industry: a 3 mm thick soda-lime glass (*SLG*) substrate [53], laying on it an 800 nm thick Mo layer [54] [55] [56] and a 2 μm CIGSe absorber layer [57]. Buffer (*CdS*) and front contact (*i-ZnO/AZO*) layers are overlooked and a glass cover was not included in the ideal case structure.

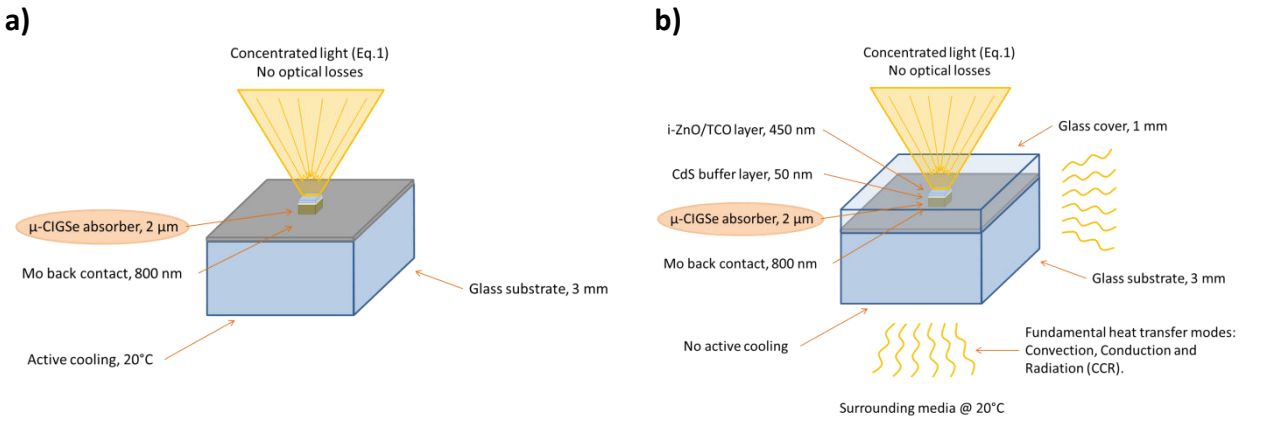

Figure 3.1: 3D sketch of the CPV device; **a)** ideal case: basic structure with active cooling (rear side at 20°C), **b)** realistic case: solar module without active cooling but with fundamental heat transfer mechanisms (convection, conduction and radiative heat dissipation to surrounding media at 20°C) [13].

An ideal model could only be representative of indoor measurements and laboratory prototypes; therefore, a complex model needs to be considered to represent real devices. Figure 3.1b shows the solar cell module for a realistic case. Here, a 50 nm thick n-type (*CdS*) layer and a 450 nm thick front contact (*i-ZnO/AZO*) sheet were included. The non-ideal structure was encapsulated with a 1 mm thick borosilicate glass cover (*BSG*) or lens (plastic or BSG) array

for protection against environmental conditions (mainly humidity) and for light concentration purposes.

As a result of the ideal and realistic model studies and the posterior fabrication of real micrometer-sized solar cells, it was necessary to investigate new thermal simulations including the fabrication process parameters. Round- and lamellar-shaped micrometer-sized solar cells were produced either shadowing the absorber with a certain mask (Shaded) or etching the CIGSe layer (Etched). For further fabrication details see chapter §4.

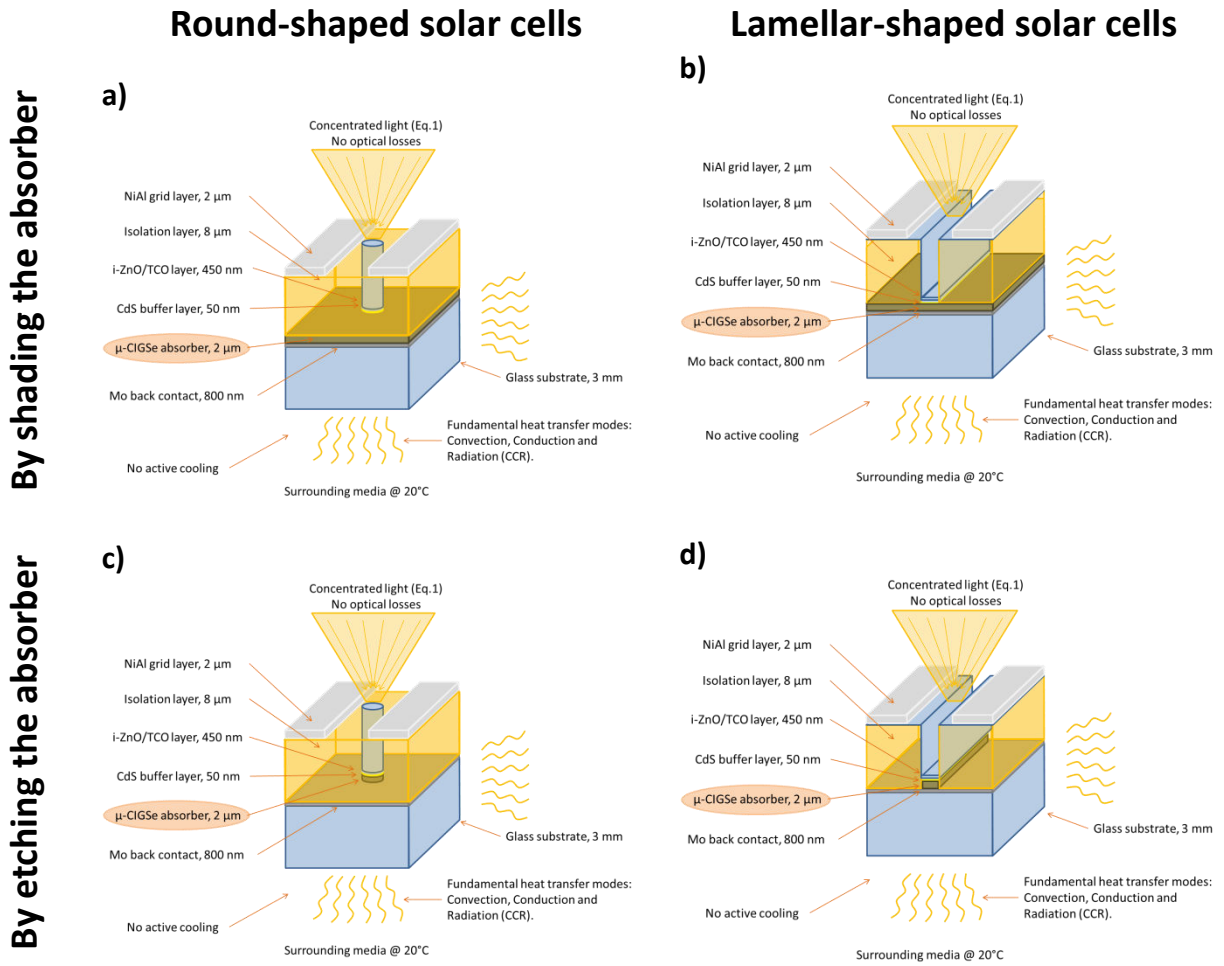

Figure 3.2: 3D simulation sketch of the CPV fabricated device; **a)** round-shaped solar cells by shadowing the absorber, **b)** lamellar-shaped solar cells by shadowing the absorber, **c)** round-shaped solar cells by etching the absorber and **d)** lamellar-shaped solar cells by etching the absorber.

3.3. Results and Discussion

3.3.1. Ideal case: study of different substrate thicknesses and back contact properties with active back interface cooling

Based on the ideal case model (Figure 3.1a), solar cell temperature evolution with concentration was investigated for different structures. Parameter variations were performed to find the best structure to enhance the solar cell heat dissipation. Different glass substrate thicknesses are available in the market [58] for different purposes. Thereby, the glass substrate thickness contribution to the solar cell heat dissipation was examined by modifying the SLG thickness.

Heat management of squared shaped solar cells laying on different substrates was investigated. For each glass thickness, from 3 mm down to 0.5 mm, different PV areas were analyzed, from 1 mm^2 down to 1 μm^2. Therefore, the concentration factors considered were from 10^0x up to 10^6x, respectively.

High temperatures are not suitable for solar cell applications. CPV devices are used to decrease cell temperature with active cooling systems, which increases the final price of CPV technology. Below 150°C the CIGSe solar cells are in a reliable temperature range, but the pn-junction [59] [60] stability in the long term increases if the cell operates under 100°C.

Figure 3.3a shows the stationary maximum cell temperature value with concentration for different glass thickness. Cell temperatures below 150°C were found for low (10^0x) to high (10^5x) concentration factors, and PV temperature values above 150°C up to 480°C (not shown) were generated for concentrations over 10^5x. The heat management of the different substrate thicknesses was slightly improved by decreasing the glass thickness. The back contact layer was set to have the same area as the absorber in this simulation. Therefore, the lateral heat dissipation was performed by the glass substrate, for which thermal conductivity remains invariable for each glass thickness modification. Furthermore, undesired heat cannot be properly dissipated to the bulk material due to the low substrate thermal conductivity. Thermal gradient lines are shown in Figure 3.4b for the ideal solar cell device. Thinner glass substrates enhance heat dissipation due to a reduction of heat gradient paths. Reducing the distance between the active cooling systems to the solar cell will improve the heat dissipation because

short gradient lines are more desirable to cool down the cell than long ones. Long gradient paths are present at the solar cell perimeter (Figure 3.4a); nevertheless, most of the glass volume was not employed to reduce the solar cell temperature.

The lateral heat dissipation of glass is the main limiting factor to enhance the heat management. The simulation model consist of different layers, one of them is the back contact layer which is on the substrate. Molybdenum exhibits better thermal properties than glass and could properly spread the generated heat along the substrate surface. In prior simulations, the absorber and back contact area were identical. Therefore, the heat spreading using the Mo layer was limited by the concentration factor. The higher the concentration factor the smaller the cell and back contact area, thereby the insignificant molybdenum layer was used to dissipate the undesired heat at high concentration factors. At high irradiation factors, the back contact layer needs to present a major role of heat dissipation to spread the generated heat along the substrate surface and therefore reduce the solar cell temperature. Hence, different back contact areas under different light fluxes were investigated. The maximum cell temperature for different concentration factors was researched for a back contact size equal to the cell area and for a Mo area equal to the substrate surface regardless of the cell area. Figure 3.3b presents a significant heat dissipation improvement by increasing the back contact area. Furthermore, the lateral heat dissipation was driven by the molybdenum layer instead of the glass substrate. Using the back contact for this purpose, the solar cell temperature at high concentration factors drops from 480°C (not shown) to 289°C at 10^6x. The back contact heat management allows the structure to dissipate the generated heat from the cell properly, shortening the gradient lines between the surface and the active cooling device. Thus, high concentration factors, $<4\cdot10^5$x and $<2\cdot10^5$x, could be applied to micrometer-sized solar cell without damaging the pn-junction for temperatures below 150°C and 100°C, respectively .

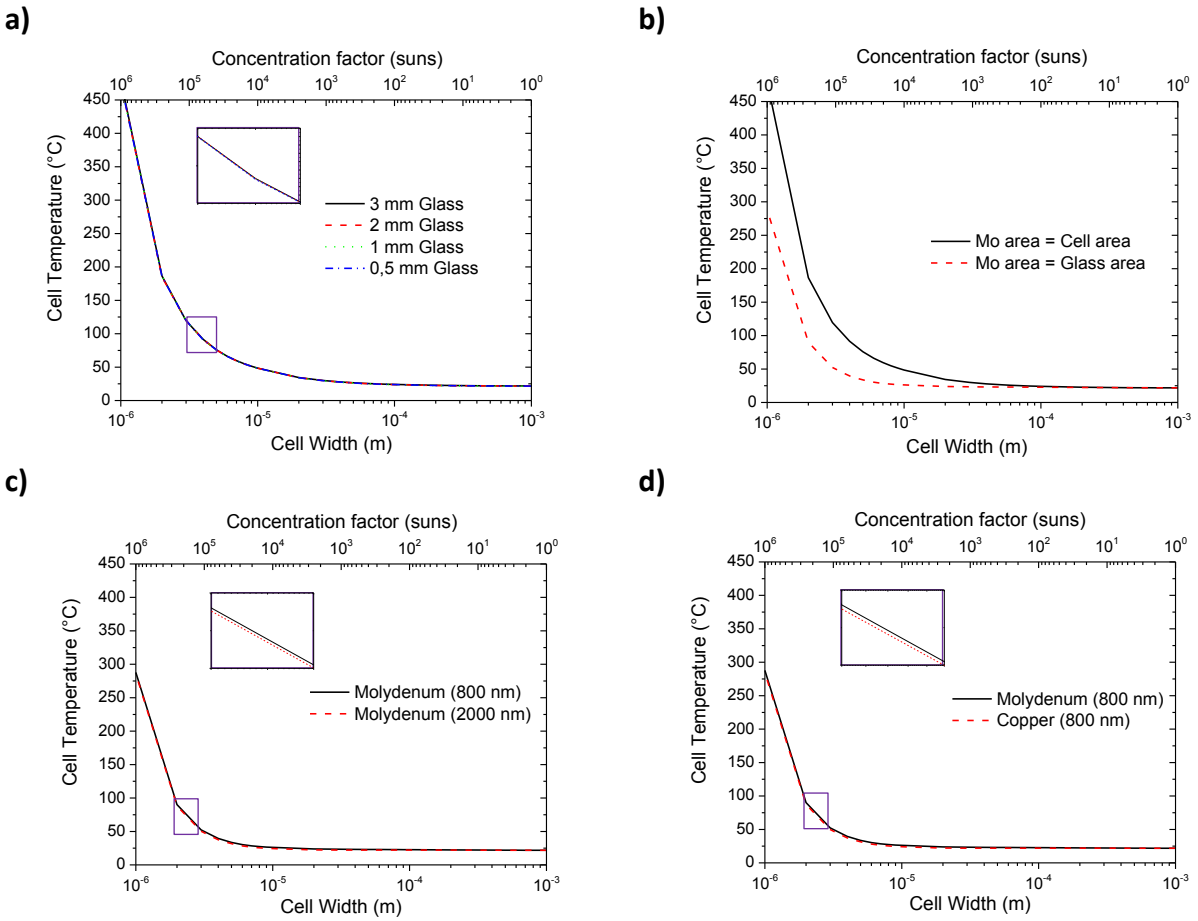

Figure 3.3: Maximum stationary temperature on micrometer-sized CIGSe solar cell under different concentration factors, varying structure parameters and fixing the substrate area (1 mm^2): **a)** reducing glass thickness (back contact area equal to cell size), **b)** increasing back contact area (3 mm thick substrate), **c)** increasing back contact thickness (back contact area equal to substrate size and 3 mm thick substrate), and **d)** changing back contact material (back contact area equal to substrate size and 3 mm thick substrate) [13].

A 3D isothermal surface cross section and enlargement (Figure 3.4a) of the ideal model with a back contact area equal to the cell area and 3 mm thick substrate is shown. Lateral heat dissipation increasing the back contact area would encourage the heat spreading along the substrate surface. Short gradient paths improve the cell temperature cooling better than long ones. In Figure 3.4b, long temperature gradient lines are exhibited due to the scant lateral glass heat conduction.

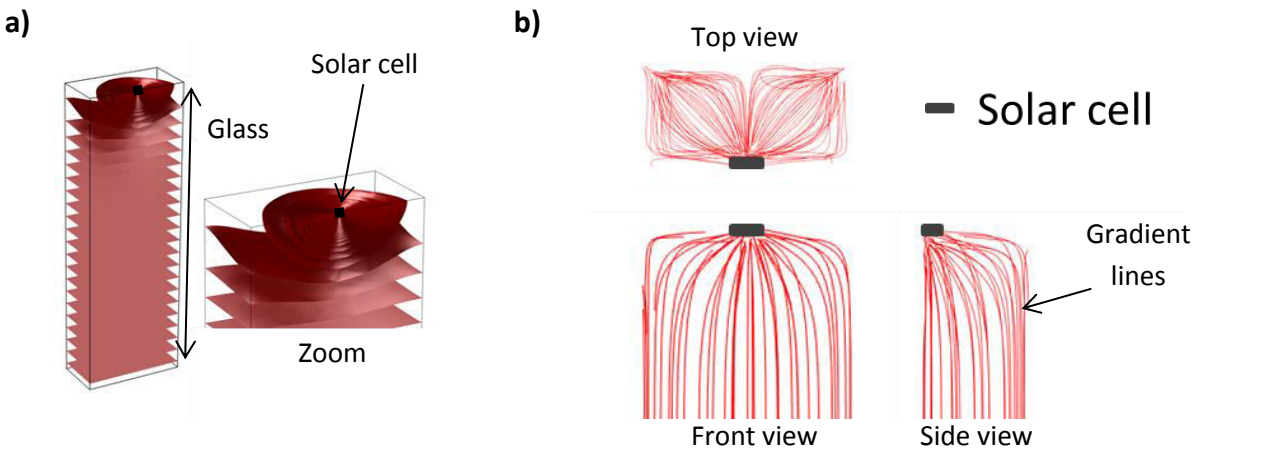

Figure 3.4: Ideal model heat management; **a)** 3D isothermal cross section and a zoom in, **b)** thermal gradient lines plotted for different views: side, top and front, for the device structure: a 3 mm thick glass substrate (with an area of 1 mm^2), an 800 nm molybdenum layer and a 2 μm thick CIGSe absorber (back contact area equal to absorber size) [13].

Improved heat dissipation management was achieved by expanding the back contact area. Due to the improvement of heat dissipation, the back contact layer area will be equal to the glass substrate area for further simulations. Lateral heat conduction may be expected to be improved by increasing the back contact metal thickness. A thermal comparison by augmenting the molybdenum thicknesses was simulated under concentrated light. 800 nm thick and 2000 nm thick molybdenum layers were used for further improve the heat dissipation of the cell. Figure 3.3c shows a slight improvement of the heat dissipation. Moreover, a slight improvement of the stationary cell temperature with increasing back contact thickness under different levels of sun concentration was observed in Figure 3.3c. A thicker metal layer improves the heat dissipation reducing the cell temperature. Nevertheless, thicker Mo back contact layers could easily be delaminated or detached from the substrate and remove the materials deposited on it [61], reducing the benefits of the slight heat dissipation gain. Furthermore, an even thinner back contact could be sufficient to spread the generated heat along the Mo/Glass interface to the detriment of the electrical properties of the back contact. Therefore, a compromise was found between the advantages and disadvantages of modifying the thickness of the back contact. Hence, for further thermal analysis, the back contact layer was set to cover the entire substrate surface with a final thickness of 800 nm.

The solar cell temperature has demonstrated a high dependence on the back contact layer properties. The heat management of the solar cell might be reinforced replacing the current metal contact with a better thermally conductive material enhancing the lateral heat spreading

along the substrate surface. Nevertheless, such material should resist the absorber fabrication conditions under a high temperature reactive atmosphere. In addition, the new material must be chemically and structurally stable to avoid contamination of the solar cell with undesired impurities. Different back contact metals (W, Mo, Cr, Ta, Nb, V, Ti and Mn) were investigated by Orgassa *et al.* [62]. In particular, W and Mo turned out to have the best performance due to less absorber/back contact interface passivation and less Se reactivity compared to the others metals in the study. However, both materials are listed as current supply risk elements [11]. An alternative to molybdenum could be copper (Cu), since it has better conductive properties compared to Mo. Moreover, Cu has a very low supply risk, it is part of the absorber and therefore used in the following production process. Here, the Mo back contact was replaced with a better conductive material to improve the heat management of the solar cell. The effect of a Cu back contact over the entire substrate surface under different concentration factors was investigated. The stationary temperature of the solar cell was assessed using the ideal model. In Figure 3.3d, a slight improvement of the final solar cell temperature was achieved as a result of replacing Mo with a better conductive material. A modest approximation of heat dissipation is that thicker or better conductive back contacts are equivalent:

$$k \cdot t = const \tag{3.1}$$

where *k* represents thermal conductivity and *t* is the back contact thickness.

Therefore, a better conducting back contact enhances the cooling capability but due to the substrate thermal properties any noticeable improvement could be appreciated. Hence, a Mo back contact was selected for further thermal analysis covering the entire substrate surface with a final thickness of 800 nm.

3.3.2. Realistic case: study of different cooling approaches and cell-substrate ratios

Heat dissipation of the solar cell for high concentration PV systems has demonstrated a high impact on the design of CPV cooling systems. Therefore, a complete cooling circuit to reduce the cell temperature is needed, increasing the final cost of the CPV module. Thermal simulations

were investigated using the basic model where active cooling was applied. Here, a complex model was considered to obtain accurate simulation results. Conduction, convection and radiation (*CCR*) of heat were included in the model. A surrounding material at room temperature was set as boundary condition for radiation and convection modes and no active cooling at the rear interface was assumed.

Two scenarios were investigated: when the realistic model is actively cooled and when the generated heat is solely dissipated by the three fundamental modes of heat transfer. The realistic model was composed of a 3 mm thick glass substrate, an 800 nm molybdenum layer (which covers the whole surface), a 2 μm thick CIGSe absorber, a 50 nm thick buffer layer (*CdS*), a 450 nm thick transparent conductive layer (*AZO*) and 1 mm thick glass cover, compare Figure 3.1b. The heat management of the solar cell for both scenarios was investigated for different concentration factors. The maximum solar cell temperature was found to be significantly higher when the CCR modes were applied (Figure 3.5). This result was expected within the simulations and the fact that actual CPV devices are mainly being refrigerated by an active cooling system and helped by the CCR heat dissipation mechanisms. However, in both studies, even for high concentration factors (>10^5x) the maximum solar cell temperature is reported to remain below the unstable pn-junction temperature range. The breakdown temperature for CIGSe solar cell usually occurs in the range from 150°C to 225°C [60]. Above these values, the solar cell performance and layer stability is endangered. For temperatures below 150°C, the performance of the cell is enhanced by concentrating light. Nevertheless, the higher the temperature of the solar cell the worse the electrical performance. However, a compromise needs to be found between the concentration factor and the output power to enhance the overall solar cell performance.

Regarding the cell stability, in both cases, high concentration factors (>10^5x) could be applied to micrometer-sized solar cells (<$2 \cdot 10^{-5}$ m) leading to a high material saving (>10^5x). Therefore, active cooling is not required but desirable for micrometer-sized solar cells in order to boost the electrical performance. Additionally, the CPV cost using micrometer-sized solar cells could be reduced avoiding active cooling due to the benefits of cell miniaturization.

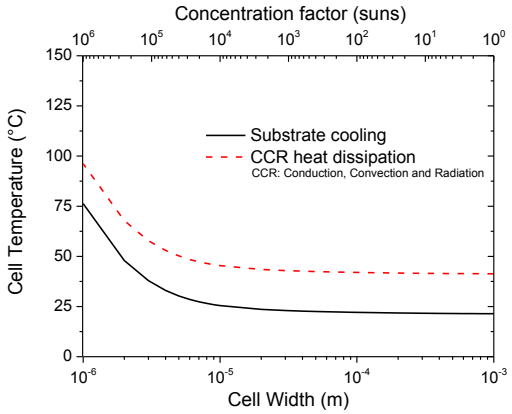

Figure 3.5: Maximum temperature of CIGSe-solar cell under different concentration factors for different heat dissipation methods: substrate back ideal cooling system and conduction, convection and radiation (CCR) heat transfer mechanism for the device structure: a 3 mm thick glass substrate (with an area of 1x1 mm^2), an 800 nm molybdenum layer (with an area of 1x1 mm^2), a 2 μm thick CIGSe absorber, a 50 nm thick buffer layer (CdS), a 450 nm thick transparent conductive layer (AZO) and 1 mm thick glass cover (with an area of 1x1 mm^2) [13].

Thermal simulations including convection, conduction and radiation heat transfer mechanisms exhibited higher temperatures in comparison with only active cooling without CCR modes. However, prior simulations were performed fixing the glass substrate area, 1 x 1 mm^2. Here, the maximum stationary temperature (Figure 3.6a) was investigated for the realistic model by changing cell and substrate sizes. Thereby, the maximum concentration factor was determined as the substrate-cell ratio shown in Equation 2.5. Varying the substrate area keeping constant the cell size or changing the cell area preserving substrate size will increase or diminish the irradiation value. Different substrate widths (from 10^{-5} to $3 \cdot 10^{-3}$ m) were simulated keeping the solar cell size constant, and on the contrary, different solar cell widths (from 10^{-6} to 10^{-3} m) were studied maintaining the substrate area constant. The heat management of the cell was analyzed for the non-ideal case by changing PV and substrate sizes assuming no active cooling and the CCR modes were included.

An isothermal surface graph is shown in Figure 3.6a, where the maximum stationary temperature of the cell is presented for different substrate and cell areas combinations. Note that the possible combinations, where the solar cell was bigger than the glass, were not taken into account but a fixed temperature was assumed in the graph. In Figure 3.6b, an isoconcentration factor map was plotted for the same dependence, to display the concentration factor distribution. The isothermal graph is superimposed on Figure 3.6b (white lines) to be able to determine the best possible configuration. Here, the increasing irradiation with concentration

produces a rising temperature on the micrometer-sized solar cell. Heat dissipation was enhanced for low concentration factors (from 1x to 10x) where either larger substrate and cells lengths were used or shorter substrate and cell lengths were simulated. Increasing the glass length to larger values by keeping the solar cell size over 10^{-5} m the maximum growth of the cell temperature is lower than the concentration factor. In this region, medium to high irradiation values (from 10x to $3.7 \cdot 10^{5}$x) could be reached, where the device stays in a dependable temperature range below 150°C (Figure 3.6a) suitable for CPV applications. Only for high concentration factors, higher than 10^{5}x, is the cell temperature above the breakdown lower limit.

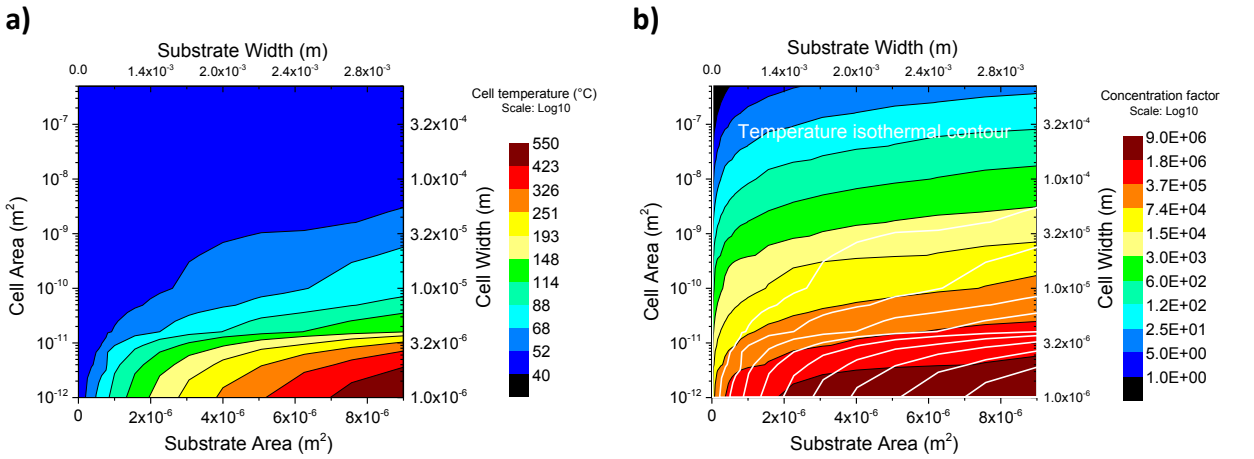

Figure 3.6: a) Maximum temperature and **b)** established concentration factor on CIGSe solar cell changing substrate and cell area ratio (overlapped in white Figure 3.6a). Realistic model: SLG (3 mm / ΔLxΔW mm^2) / Mo (800 nm / ΔLxΔW mm^2) / CIGSe (2 µm / ΔlxΔw $µm^2$) / CdS (50 nm / ΔlxΔw $µm^2$) / TCO (450 nm / ΔlxΔw $µm^2$) / BSG (1 mm / ΔLxΔW mm^2), CCR heat dissipation mechanisms and no active cooling applied [13].

During the thermal simulations, different substrate-cell area ratios could be used to enhance the solar cell performance by dissipating the generated heat but no ultimate conclusion about the best ratio could be deduced. Nevertheless, low to high concentrations (from 1x to $3.7 \cdot 10^{5}$x) appear feasible for application to the micrometer solar cells. Under these illumination factors, the solar cell remains at a reliable temperature operation range. Despite the thermal results obtained, the device fabrication will restrain the minimum size of the micrometer-sized CIGSe solar cell. Based on this limitation, the substrate dimensions would be selected to enhance the heat dissipation of the cell.

3.3.3. Realistic case: study of different illumination profiles

Low to high concentration factors are feasible to be applied on micrometer-sized CIGSe solar cells due to improved heat management compared to macroscopic devices [33]. However, the light concentration on the cell was assumed to be ideal and without optical loses. Although, real systems have to be taken into account as is the incorporation of micro-lenses to concentrate the incoming light onto the absorber. Usually, macroscopic CPV technology employs lenses or mirrors to focus sunlight onto the solar cells [7]. Besides obtaining a higher performance, the use of additional optics to focus sunlight has also raised the cost of concentrated photovoltaics compared to conventional photovoltaic devices [63]. While this allows a more efficient PV energy generation; however, concentrating light employs direct sunlight rather than diffuse light requiring tracking systems [64]. Fresnel lenses, parabolic mirrors, reflectors or luminescent concentrator systems are widely used for light concentration. Furthermore, current CPV technology is strongly sensitive to misalignment, irradiation profiles and the mismatch of the light spectrum, apart from other factors. Moreover, the CPV cost is driven up based on these requirements. However, for a cheap device increasing angular tolerance of illumination, simplifying tracking systems, reducing focal length and lowering the number of optical elements is strongly required [7].

Even when current CPV systems requires high standards, CPV optical systems often do not produce a uniform flux density distribution at the output aperture [7]. One of the last achievements of the CPV community was the implementation of an optical system without light spectrum mismatch in a plastic based Fresnel lens [9]. However, a good concentrator system should be able to tolerate misalignment, various irradiation profiles and light spectrum mismatch, providing an acceptable performance. Two types of lens systems are widely used for CPV applications, which provide either a Gaussian like light distribution image or a Tower like irradiation profile image.

The heat management of the solar cell was examined for different beam profiles. Here, the three fundamental heat dissipation mechanisms were included in the model and no active cooling was assumed. Concentrated light was applied to the realistic model using different light

distributions: Planar distribution, Gaussian like beam and Tower like profile. The Gaussian like distributions are produced by a single optical element usually Fresnel concentrator lenses. Although, Fresnel images are not as sharp as the equivalent simple spherical lens due to diffraction at the edges of the ridges [65]. On the other hand, Tower like distributions are desirable for high concentration photovoltaics due to the homogeneous irradiation along the high efficient III-V solar cells. Nevertheless, an optical system with more elements is required for the Tower like profile with either a beam homogenizer after the primary lens or a secondary lens system to spread the light uniformly along the solar cell [8] [66]. The Planar distribution refers to the ideal flat irradiation.

Different illumination profiles were applied on a 100 µm diameter solar cell implemented in the non-ideal simulation model. Figure 3.7a shows selected Gaussian beam distribution applied in the simulation and in Figure 3.7b the Tower like profiles used are plotted for different concentration factors. Based on the selected geometry, the substrate-cell area ratio presents a concentration factor of 127x. Furthermore, the volume contained below the different beam profiles is taken to be equal, considering that the solar cell receives the same amount of energy regardless of the shape of the Gaussian or Tower beam. For the Tower like beam the normalization was straightforward due to the rectangle shape of the profile:

$$C_1 \cdot Area_1 = C_2 \cdot Area_2 \;\rightarrow\; \frac{C_1}{C_2} = \frac{\pi \cdot r_2^2}{\pi \cdot r_1^2} = \left(\frac{r_2}{r_1}\right)^2 \;\rightarrow\; C_2 = C_1 \cdot \left(\frac{r_1}{r_2}\right)^2 \tag{3.2}$$

where *C* is the concentration factor and *r* is the Tower beam radius.

But for the Gaussian case the normalization was calculated as follows. The volume enclosed by a Gaussian beam and the volume confined for a certain radious are detailed in the following equations:

$$V = \iint_{-\infty}^{+\infty} f(x,y) \cdot dxdy = 2 \cdot \pi \cdot A \cdot \sigma_x \cdot \sigma_y \tag{3.3}$$

$$\text{where } f(x,y) = A \cdot e^{-\left(\frac{(x-x_0)^2}{2\cdot\sigma_x^2} + \frac{(y-y_0)^2}{2\cdot\sigma_y^2}\right)} \tag{3.4}$$

$$\int_0^{2\cdot\pi} \int_0^r f(r,\theta) \cdot r \cdot dxd\theta = -2 \cdot \pi \cdot A \cdot \sigma^2 \cdot \left[e^{-\left(\frac{r^2}{2\cdot\sigma^2}\right)} - 1\right] \tag{3.5}$$

$$V_1 = V_2 \;\rightarrow\; A_1 \cdot \sigma_1^2 \cdot \left[e^{-\left(\frac{r^2}{2\cdot\sigma_1^2}\right)} - 1 \right] = A_2 \cdot \sigma_2^2 \cdot \left[e^{-\left(\frac{r^2}{2\cdot\sigma_2^2}\right)} - 1 \right] \tag{3.6}$$

where V is the volume enclosed by the Gaussian beam, A the normalization factor, r and σ represent the solar cell radius and the Gaussian standard deviation, respectively.

a) **b)**

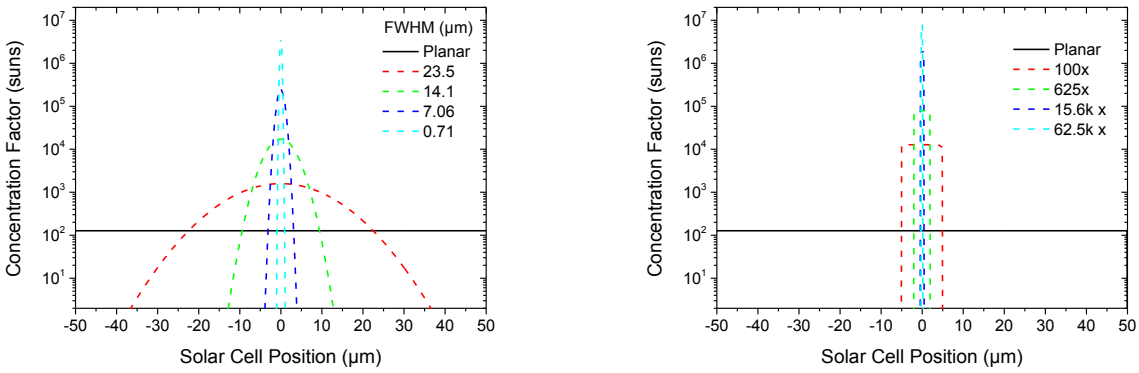

Figure 3.7: a) Gaussian like beam profile **[13]** and **b)** Tower like beam profile along the solar cell surface as a function of the full width at half maximum (FWHM) and the Tower size, respectively. Realistic model: SLG (3 mm / 1x1 mm^2) / Mo (800 nm / 1x1 mm^2) / CIGSe (2 µm / ∅ 100 $µm^2$) / CdS (50 nm / ∅ 100 $µm^2$) / TCO (450 nm / ∅ 100 $µm^2$) / BSG (1 mm / 1x1 mm^2), CCR heat dissipation mechanisms and no active cooling applied.

Thereby, the maximum stationary temperature of the solar cell was simulated for the different beam profiles. The heat dissipation was analyzed for a variety of Gaussian standard deviation values from 100 to 0.01 µm, in terms of full width at half maximum (FWHM) from 235 to 0.02 µm. The full width at half maximum is defined as follows:

$$FWHM = 2 \cdot \sqrt{2 \cdot ln2} \cdot \sigma \tag{3.7}$$

where σ is the Gaussian standard deviation.

Tower like beam distributions were employed to analyze the temperature management of the cell for a variety of Tower widths (TW) values from 50 to $5{\cdot}10^{-3}$ µm, in terms of relative concentration factor from 10^0x to 10^8x. Note that the concentration factor of the Planar distribution is 127x, therefore, the Tower concentration values were incremented by this factor.

The temperature distributions along the solar cell diameter are shown in Figure 3.8a-b for the incident Gaussian and Tower beams, respectively. Narrow beam profiles produce highly

localized heat onto the cell which could lead to a hot point and produce a shunted cell if the temperature value is above 150°C. Moreover, using narrow Gaussian or Tower like beams could help to simplify module fabrication, device assembly and system operation requirements. Hence, higher design tolerances are provided using narrow illumination profiles helping to mitigate the effect of lens misalignment and facilitating the operation of the tracking systems.

Nevertheless, flat irradiation profiles are desirable for heat dissipation and lower the solar cell temperatures as the simulations depicted. Although, even for tiny FWHM values (< 0.1 µm) and TW values (< 0.1 µm), the maximum solar cell temperature remains below 100°C boosting the cell tolerance against focusing elements.

a) **b)**

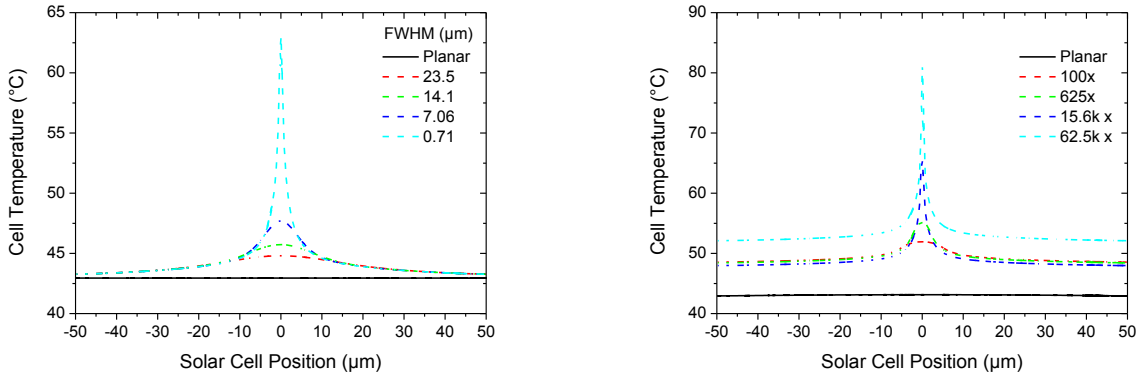

Figure 3.8: Temperature profile along the solar cell surface as a function of the incident **a)** Gaussian like beam profile (FWHM) **[13]** and **b)** Tower like beam profile (TW). Realistic model: SLG (3 mm / 1x1 mm^2) / Mo (800 nm / 1x1 mm^2) / CIGSe (2 µm / ∅ 100 $µm^2$) / CdS (50 nm / ∅ 100 $µm^2$) / TCO (450 nm / ∅ 100 $µm^2$) / BSG (1 mm / 1x1 mm^2), CCR heat dissipation mechanisms and no active cooling applied.

The maximum temperature of the solar cell was plotted as a function of the irradiation distribution applied on the realistic model. Figure 3.9a-b illustrate the temperature behavior according the applied beam properties. This performance was fitted using different equations as a function of the selected parameters to predict the maximum temperature of the solar cell as a function of the beam characteristics. For the Gaussian beam distribution, the evolution of the maximum temperature of the solar cell was intended to depend on the Gaussian standard deviation of the illumination profile and the temperature of the micrometer-sized CIGSe solar cell under standard test conditions. Furthermore, the concentration factor extracted from the shape of the Tower like distribution was selected as the fitting parameter as well as the temperature of the solar cell under one sun to determine the change of the temperature with

concentrated light. This approximation resulted in a good correlation for the Gaussian distribution but a rough approximation was implemented for the Tower like beam profile. The maximum temperatures obtained as a result of the thermal simulations of the Gaussian distribution were fitted using the following formula:

$$\boldsymbol{T_{\,under\,Gaussian\,Beam} = T_{Flat\,Beam} \cdot \left[1 + e^{-\frac{3}{2}} \cdot \frac{e^{-\sigma}}{\sqrt{\sigma}} \right]} \qquad \text{[13] (3.8)}$$

where $T_{Flat\ Beam}$ is the solar cell temperature for a uniform beam, and σ represents the standard deviation (Gaussian RMS width expressed in μm, value applied in equation without units).

On the other hand, the fitting of the Tower distribution temperature results was difficult to implement an equation as a function of the Tower properties. Therefore, the following equation was obtained providing rough temperature values in comparison with the simulated ones. Although, the equation provided could give an idea of the expected maximum temperature for a certain concentration.

$$T_{under\,Tower\,Beam} = T_{Flat\,Beam} \cdot \left[1 + C^{\frac{2}{3}} \right] \qquad (3.9)$$

where $T_{Flat\ Beam}$ is the solar cell temperature for a uniform beam, and *C* represents the concentration factor applied.

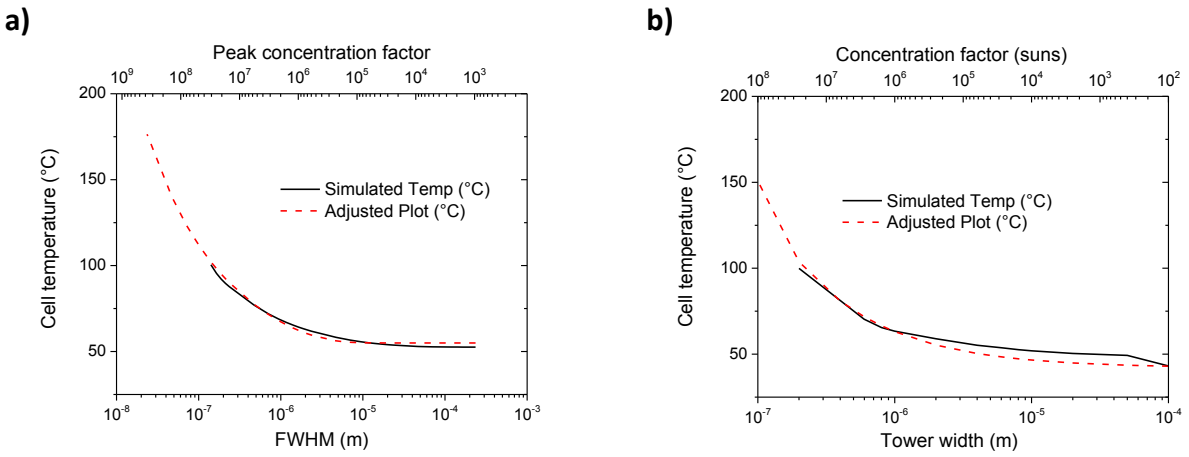

Figure 3.9: Maximum temperature of the solar cell and a fitting plot as a function of the incident **a)** Gaussian like beam profile (FWHM) **[13]** and **b)** Tower like beam profile (TW). Realistic model: SLG (3 mm / 1x1 mm^2) / Mo (800 nm / 1x1 mm^2) / CIGSe (2 μm / ∅ 100 μm^2) / CdS (50 nm / ∅ 100 μm^2) / TCO (450 nm / ∅ 100 μm^2) / BSG (1 mm / 1x1 mm^2), CCR heat dissipation mechanisms and no active cooling applied.

Any kind of simulation presents different limitations due to the code used to solve the desired equations, the speed of calculation and the resources available to perform the simulations. One of the main problems resides in the limited RAM memory resources [67]. The mesh size of the dense mesh matrix in the simulation model was defined to avoid overloading of the simulation, therefore, narrow spot beams cannot be studied and are neglected in our simulations, in particular FWHM or TW values below 500 nm.

Nevertheless, assuming that prior equations follow the temperature behavior of the cell for narrow beams, profiles with a FWHM or TW lower than $4 \cdot 10^{-2}$ μm or $1 \cdot 10^{-1}$ μm respectively, are expected to produce localized temperatures higher than 150°C. Hence, for a Gaussian standard deviation below 0.017 μm the stability of the solar cell, it is uncertain what could lead to a shunted cell. A FWHM above $4 \cdot 10^{-2}$ μm or a TW above $1 \cdot 10^{-1}$ μm will provide the best thermal performance when a micrometer-sized CIGSe solar cell is illuminated with a Gaussian beam or a Tower like profile.

3.3.4. Real device characterization study

According to our thermal studies high concentration factors, up to 10^5x, are feasible for application on micrometer-sized CIGSe solar cells. A real device was fabricated and analyzed under different illumination fluxes. Therefore, it was necessary to investigate new thermal simulations including the fabrication process parameters and the I-V characterization conditions. The methodology to measure the I-V characteristic curve of the solar cell was using a LCPV solar simulator, which was capable of concentrating light up to 150 suns by illuminating a 50 x 50 mm^2 area. Thereby, the solar cell and surrounding material was illuminated instead of a sole cell. The cell temperature will increase with concentration for a certain period of time until the stationary temperature is reached. Furthermore, the I-V characteristics of the solar cell will be influenced by the solar cell temperature under concentration. The thermal evolution during a set of time and concentration factor was investigated for a 200 μm diameter solar cell. Additionally, the total simulated area was in accordance with the micrometer-sized solar cells pitch employed in the lithography process (3 mm). Therefore, the periodic boundaries were

established around the 3 x 3 mm^2 model, specifically, symmetry to consider multiple solar cells. Figure 3.2a-d show the solar device structure used for the thermal simulations.

a) **b)**

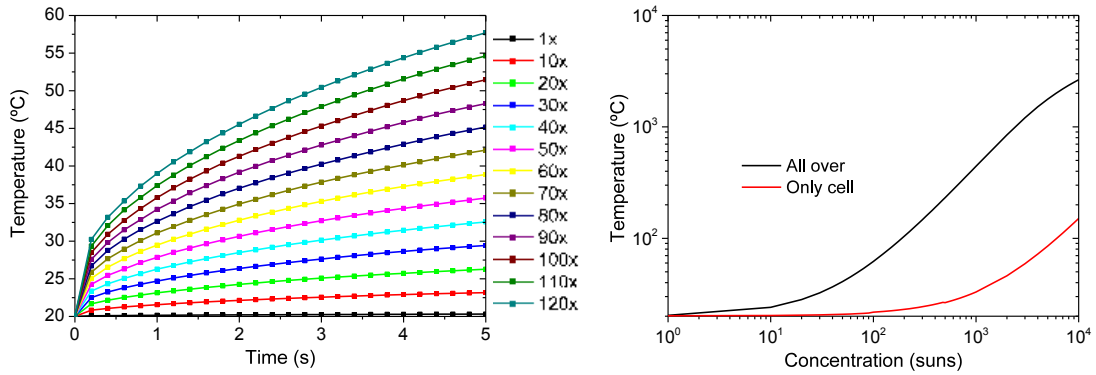

Figure 3.10: a) Cell temperature evolution during a set of time and concentrated light, active area and surrounding are illuminated. **b)** Stationary temperature evolution with concentrated light for the cases: "*All over*" active area and surrounding are illuminated, and "*Only cell*" only active area is illuminated. Realistic model: SLG (3 mm / 3x3 mm^2) / Mo (800 nm / 3x3 mm^2) / CIGSe (1.7 µm / ∅ 200 µm^2) / isolation layer (5 µm / 3x3 mm^2 excluding PV area) / CdS (50 nm / 3x3 mm^2) / TCO (450 nm / 3x3 mm^2) / NiAl (two lamellar-shaped contacts on the solar cell sides, 1.35x3 mm^2 each). Without glass cover and antireflection layer, CCR heat dissipation mechanisms and no active cooling applied.

The cell temperature evolution through time depicted a fast temperature increment within the first seconds of the measurement followed by a saturation level (not shown), Figure 3.10a. The temperature gap, between a fully illuminated device and sole illuminated cell, increases with concentration (Figure 3.10b). Moreover, the effect of the temperature dependence with time and concentration on the solar cell performance will be further analyzed in the following chapters. Hence, the solar cell temperature evolution will influence the analysis of the I-V characteristic curve and the results of the opto-electronic simulations.

3.4. Conclusions

Besides the advantages of CPV technology, generated heat under concentration represents one of its main weaknesses. Heat dissipation and temperature operation of the solar cell have demonstrated a high impact on the design of CPV modules. Moreover, current CPV technology requires active cooling to dissipate the generated heat with concentrated light. However, solar cell minimization has shown a good disposition to enhance heat dissipation and to boost the performance of the micrometer-sized CIGSe solar cells with concentration.

As far as the author knows, there has been no detailed micrometer-sized solar cell temperature study, with the exception of the light contribution by Sadewasser *et al.* [24], to corroborate the benefits of reducing cell size and increasing concentration factor. The heat management of the desired device structures under different circumstances was investigated to understand in more depth the advantages of CPV minimization.

Here, two different thermal models were investigated: the basic and the realistic case. The first represents a model for indoor measurements although it could be used for other specific applications under certain assumptions. The objective of the realistic model was to illustrate the temperature behavior of a micrometer-sized solar cell for outdoor applications. Additionally, the non-ideal case was intended to represent a non-active cooled device to demonstrate the real benefits of CPV miniaturization.

According to the finite element method simulations, CPV design parameters as the back contact material or substrate thickness have minor contributions to dissipate the generated heat. However, the properties of the back contact such as thermal conductivity, area or thickness present an important role to reduce the temperature of the solar cell. Heat dissipation is improved by increasing the back contact functionality.

High concentration factors, up to 10^5x, are feasibly applied on micrometer-sized CIGSe solar cells depending on the presented thermal studies. Solar cell temperature remains below the pn-breakdown range for concentrations below 10^5x produced for PV cells width above 20 μm for a 3 mm wide substrate and above 3.2 μm width for a 0.5 mm wide substrate. Different cell designs are possible to increase the light flux on the cell maintaining the absorber in a reliable temperature operation range.

Different illumination profiles were investigated. Although homogeneous irradiation beams along the solar cells surfaces are desirable in order to decrease cell temperature, CPV operational requirements could be reduced by applying different illuminations beams as Gaussian and Tower like shapes. Narrow beam profiles produce highly localized heat onto the cell which produces a highly located temperature increment. Nonetheless, using Gaussian or Tower like beams could simplify CPV module fabrication, device assembly and operational

requirements. Furthermore, for tiny FWHM values (< 0.1 μm) and TW values (< 0.1 μm) the maximum cell temperature remains below 100°C boosting the cell tolerance against the effect of lens misalignment or the issues of the tracking systems. Moreover, profiles with a FWHM or TW lower than $4 \cdot 10^{-2}$ μm or $1 \cdot 10^{-1}$ μm, respectively, are expected to produce localized temperatures lower than 150°C.

In the following chapters, further analysis will be conducted to prove the benefits of these thermal studies including an opto-electronic model, where I-V simulations under concentrated light will be investigated for different scenarios.

Chapter 4:

Fabrication

4.1. Introduction

In the previous chapter, thermal simulations have shown the feasibility of concentrating high fluxes of light on micrometer-sized solar cells. The minimization of solar cells exhibited an improved heat dissipation mechanism capable of avoiding the use of external devices for active cooling. The temperature of the solar cell was simulated for different circumstances: as a function of the irradiance and design parameters. Moreover, fundamental heat transfer mechanisms were taken into account in the model as of other boundary conditions such as: no active cooling, reflected light, non-absorbed photons (sub-band gap and UV energy photons), power conversion to electricity and Joule loss.

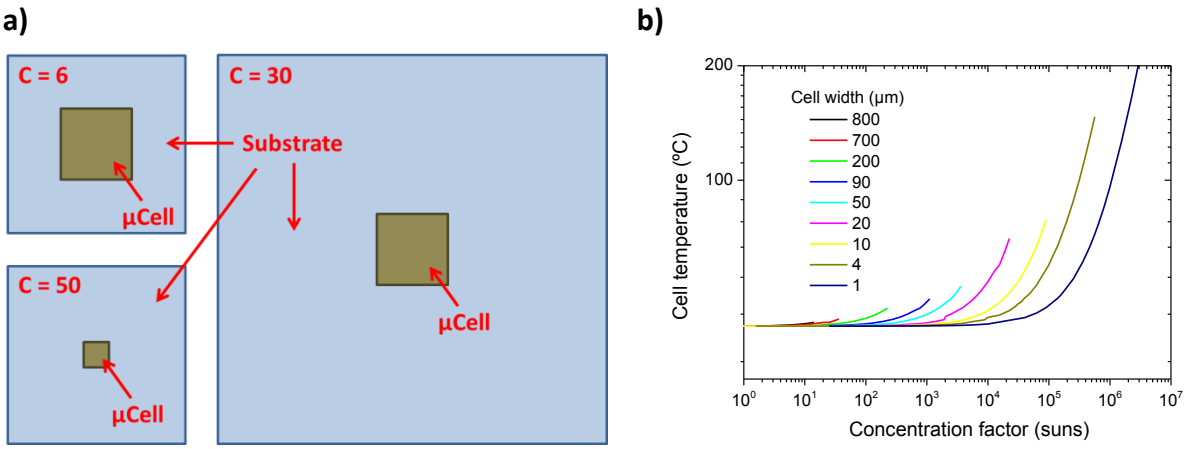

Figure 4.1: a) Substrate or cell size modification example of the different possible area variations. **b)** Maximum temperature on CIGSe solar cell changing substrate and cell area ratio for the device structure: a 3 mm thick glass substrate, an 800 nm molybdenum layer (with an area equal to the substrate area), a 2 µm thick CIGSe absorber, a 50 nm thick buffer layer (CdS), a 450 nm thick transparent conductive layer (AZO) and 1 mm thick glass cover (with an area equal to the substrate area).

Micrometer-sized (< 1 mm^2) solar cells displayed an improved heat dissipation mechanism when the solar cell area was reduced compared with large areas (Figure 1.1a-b). Heat dissipation was

enhanced using larger substrate and smaller cells. Hence, solar cell minimization has the advantage of better thermal management than macroscopic devices under concentrated illumination.

Thereby, as a result of these investigations, micrometer-sized $Cu(In_xGa_{1-x})Se_2$ (*CIGSe*) solar cells were fabricated and characterized under concentrated light to confirm the thermal simulations and posterior opto-electronic simulations. This chapter is focused on the description of the fabrication process from the growth of micrometer-sized CIGSe solar cells in the so-called "*top-down approach*".

4.2. Solar cell fabrication process

Micrometer-sized CIGSe solar cells were fabricated for subsequent characterizations under concentrated AM1.5G light and for comparison with thermal and opto-electronic simulations. The fabrication of the micrometer-sized solar cell combined different processes. On a 3.2 mm thick soda lime glass substrate, an 800 nm Mo layer was deposited by magnetron sputtering followed by a 1.7 μm thick CIGSe layer. A three stage co-evaporation process, by co-evaporation of elemental copper, indium, gallium and selenium materials, was used to form CIGSe absorbers (Figure 4.2a-I). Once a planar absorber was created, a circular array pattern (7.0 μm thick, truncated-cone shape) was imprinted on the CIGSe surface based on a photolithography process (Figure 4.2a-II). Using a negative photoresist (*MicroChemicals, AZ nLoF 2070*) and a post development annealing, a hard coating was induced (Figure 4.2a-II). The photoresist/CIGSe surface was exposed to an acid-based solution (Piranha) and only the unprotected CIGSe was removed but not the photoresist (partially time-resistant against this chemical bath) (Figure 4.2a-III). Afterwards, the remaining photoresist was cleared away using a lift off process (Figure 4.2a-IV). This procedure is called "*top-down approach*". To avoid possible short-circuits, a photoresist coating was employed to isolate the molybdenum areas left exposed after the etching process. A negative array pattern was imprinted on the CIGSe/Mo surface overlapping the edges of the micrometer-sized absorbers (Figure 4.2a-V). A smaller diameter was used for the second mask pattern to avoid short-circuits at the cell perimeter and an alignment tolerance

was also included. The isolation ring around the cell overlaps 9.3 ± 0.1 µm the active area. The cell structure was finished using a double thick CdS buffer layer (90 nm) created by a standard chemical bath deposition, an isolation barrier of 130 nm thick intrinsic zinc oxide layer (i-ZnO) and a 290 nm thick AZO front contact layer, were deposited by magnetron sputtering (Figure 4.2a-VI). A conductive Ni/Al (10 nm / 2 µm) grid was deposited onto the pre-patterned cell by evaporation using a lamellar-shaped mask for lithography applications (Figure 4.2a-VII). The lamellar width was selected to avoid overlapping and to include alignment deviations. Photo-generated current was extracted along the cell sides using the Ni/Al grid. The distance between the active area and the Ni/Al paths was approximately one half of the cell radius. Anti-reflective coatings (*ARC*) were not applied to the micrometer-sized cells and no glass cover was included. Figure 4.2a shows the fabrication process line of this top-down approach.

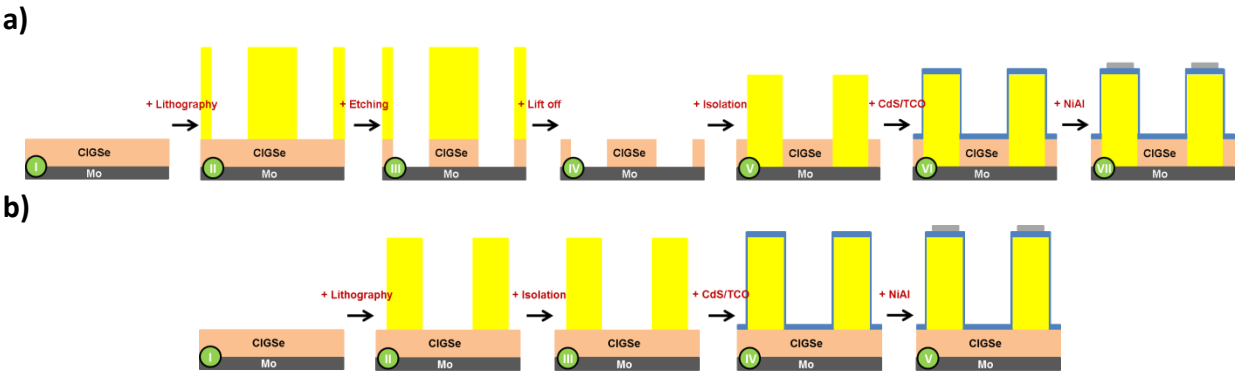

Figure 4.2: Micrometer-sized solar cell fabrication process steps, top-down approach, by **a)** etching and **b)** shadowing the absorber.

Arrays of micrometer-sized solar cell were produced by this technique. Additionally, micrometer-sized solar cells were fabricated without etching the absorber but by shadowing the CIGSe material with the photoresist (Figure 4.2b-I-V). In the same manner, lamellar-shaped solar cells were fabricated by etching (*LSE*) and by shadowing (*LSS*) the absorber. The fabrication processes is explained in more detail hereunder.

4.2.1. Back contact (Mo) fabrication process

On a Soda Lime Glass (*SLG*) substrate a silicon oxinitridized (SiO_xN_{1-x}) barrier layer was deposited by magnetron sputtering at PVcomB (*Competence Centre Thin-Film- and Nanotechnology for Photovoltaics Berlin*) facilities by M. Hartig. The SiO_xN_{1-x} layer was used to reduce the diffusion

of the SLG elements into the solar cell, especially, the diffusion of sodium (*Na*). Na is reported to strongly affect the solar cell performance; therefore, a controlled sodium content layer was added. Following the deposition of the barrier layer, a molybdenum bilayer was sputtered (*Leybold Optics Dresden, DC A600V7 tilted 7°*). A 50 ± 5 nm thick Mo bonding layer was firstly deposited followed by a 580 ± 5 nm thick conductive layer. Due to the inclusion of a barrier layer, a 70 ± 5 nm thick sodium content controlled layer was sputtered from a Mo:Na (1.3 wt.%) sputtering target and protected from posterior processes with a 50 ± 5 nm thick Mo layer. The back contact layers were deposited by applying 5.0 ± 0.1 kW under an argon atmosphere of $5.00 \pm 0.01 \cdot 10^{-3}$ mbar.

4.2.2. Absorber (CIGSe) fabrication process

Two different processes were used to fabricate the $Cu(In_x,Ga_{1-x})Se_2$ (*CIGSe*) absorber: sequential and co-evaporation process. A two-step sequential process was firstly employed for the absorber formation by evaporating elements in a vacuum chamber and the posterior selenization in a rapid thermal process (*RTP*) oven. However, CIGSe absorbers produced with this technique presented inhomogeneities with a radial distribution. Here, the absorbers produced by sequential process were not taken into account in this Thesis (Further details in Appendix II-1).

The formation of CIGSe using elemental precursors was widely investigated [68] [69]. The evaporation or sputtering of elemental materials was mainly used by the research community previously. Other deposition techniques, like electrodeposition [70] or inkjet printing [71], were used to produce the p-type layer. However, here, a highly controlled process was employed for the absorber formation. An HZB standard co-evaporation process was selected for the CIGSe fabrication. Co-evaporation of Cu, Ga, In and Se elemental components were deposited at high temperature in a vacuum chamber to produce the CIGSe layer (*HZB, PVD-A*) by T. Köhler (Further details in Appendix II-1). CIGSe absorbers produced with this technique presented a homogeneous distribution. Further analyses and processes carried out on the fabricated layers are shown in the subsequent sections.

4.2.3. Buffer layer (CdS) fabrication process

The buffer layer was fabricated using an HZB improved formula by T. Köhler, B. Heidmann, C. Ferber and M. Kirsch. Prior to deposit the cadmium sulfide (*CdS*) layer, a potassium cyanide (*KCN*) treatment was applied to the CIGSe surface. A 10% KCN solution was employed for 3 minutes to remove CIGSe secondary phases at the absorber surface. 5.000 ± 0.010 g of KCN powder (*Merck, >96% purity*) were dissolved in 50.0 ± 0.5 ml distilled H_2O and the same amount of potassium hydroxide (*KOH*) (*Merck, >85% purity*). After the KCN treatment, CdS was deposited by a chemical bath deposition (*CBD*) technique. For the formation of cadmium sulfide, cadmium acetate hydrate ($CdCH_3COO{\cdot}2H_2O$) (*Merck, 99.0% purity*) was dissolved in ammonia (NH_3) (*Merck, 30% purity*): 0.440 ± 0.010 g of $CdCH_3COO{\cdot}2H_2O$ per 100 ml of NH_3. Additionally, another ammonia solution was diluted in H_2O (ratio 1:2). Also, a thiourea (CH_4N_2S) (*Merck, 99.9% purity*) solution was diluted in distilled H_2O: 7.685 ± 0.010 g of CH_4N_2S per 100 ml of H_2O. The 200 ml solution to produce the CdS layer was composed of 15.0 ± 0.5 ml of cadmium acetate hydrate/ammonia, 15.0 ± 0.5 ml of ammonia/H_2O, 20.0 ± 0.5 ml of thiourea/H_2O and 150.0 ± 0.5 ml of distilled water. The final 90 ± 5 nm thick CdS layer was obtained by repeating this process twice. The sample was inside the chemical bath for 7.0 ± 0.1 minutes at 60 ± 2 °C in each cycle.

4.2.4. Window layer (i-ZnO/AZO) fabrication process

Transparent window layers were deposited onto the CdS surface. Intrinsic zinc oxide (*i-ZnO*) and an aluminum-doped zinc oxide (*AZO*) were sputtered (*Von Ardenne, VISS300*) by M. Kirsch and C. Ferber. Intrinsic ZnO and an AZO ($ZnO{:}Al_2O_3$ *1.5 wt.%*) sputtering targets were used. Both layers were deposited by heating up the substrate to 150 ± 3 °C under a chamber pressure of 8.00 ± 0.01 $\cdot 10^{-3}$ mbar. A 130 ± 5 nm thick i-ZnO layer and a 290 ± 5 nm thick AZO film were deposited by applying a power density of 1.5 and 2.5 KW, respectively. The electrical properties of these layers were measured with four point probe equipment. The deposited layers exhibited a film resistivity of 0.390 ± 0.006 mΩ·cm for i-ZnO sheets and 0.145 ± 0.002 mΩ·cm for AZO thin-films.

4.2.5. Front contact (Ni/Al) fabrication process

To promote the extraction of the photo-generated current, a front contact metal grid was deposited (HZB, PVD) by M. Kirsch. A 10 ± 1 nm thick nickel (Ni) bonding layer was firstly deposited followed by a 2000 ± 10 nm thick aluminum (Al) conductive layer. Nickel layers were deposited by e-beam and Al films by evaporation. A photolithography mask was used to pattern the desired Ni/Al metal grid on the micrometer-sized solar cells.

4.2.6. Lithography process

Micrometer-sized CIGSe solar cells were patterned with MJB-3 lithography equipment from the Karl Suss company (Figure 4.3). The system was composed of a 350 W mercury (*Hg*) arc lamp and its power supply. Additionally, a vacuum system was used to hold the lithography mask and the sample. A *xyz* micrometer-platform, to align the sample respect to the mask, and a controller unit were included in the lithography setup. The controller unit operated the process parameters such as illumination time, vacuum pressure or lamp power. The photoresist was deposited and distributed with a spin coater (*SPS, Spin150*). A hotplate (*Prazitherm, PZ28-1*) was employed to bake the deposited photoresist (Figure 4.3).

a) **b)**

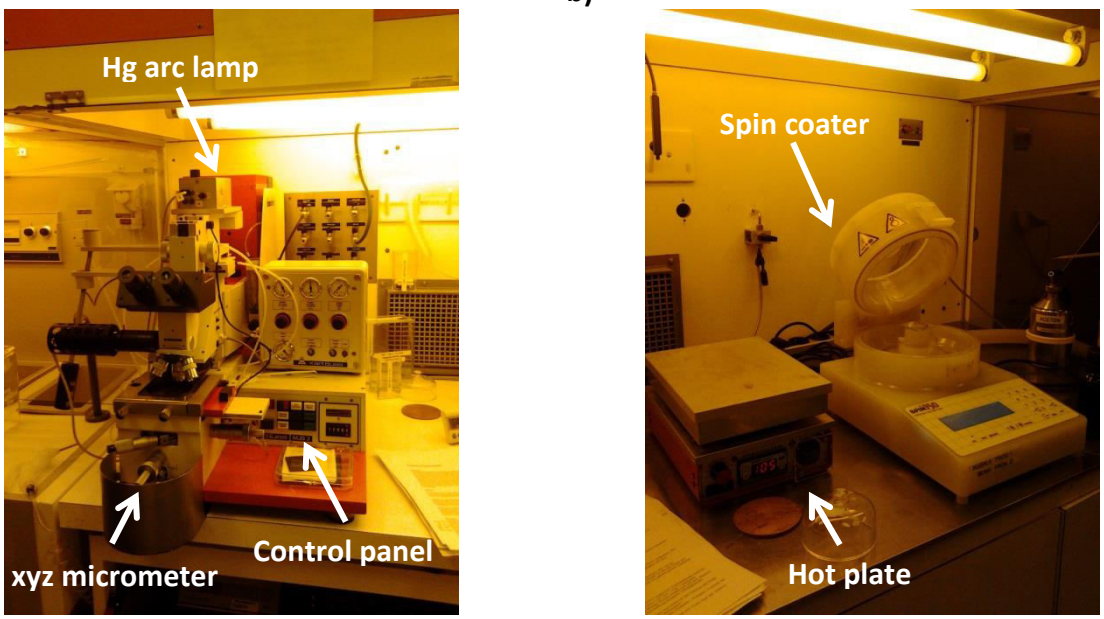

Figure 4.3: Lithography setup used to pattern the sample surface, **a)** the MJB-3 lithography equipment from the Karl Suss company and **b)** the hotplate (left) from the Prazitherm company and the Spin150 spin coater (right) from the SPS company.

Three chemical products were used to create a lithography pattern onto the solar cells surface: the AZ nLOF 2070 negative photoresist (*AZ2070*), the AZ developer (*AZ-D*) and the TechniStrip Micro D350 (*DMSO*). These products were brought from the MicroChemicals company. The selection of a negative photoresist was made based on the advantages of the negative photoresist respective to the positive resin [72] [73]. The negative resist exhibits a better adhesion to flat surfaces than the positive resins; furthermore, the negative photoresist resistance against chemical baths is higher than the other type of photoresist [73]. A different variety of curing epoxy resins were present in the market, accelerator molecules like amines or anhydrides or phenols or thiols were included into the epoxy to increase the epoxy curing reaction [73]. A phenol-based resin was selected for the developing of the micrometer-sized solar cell due to its higher resistance against chemicals and an elevated operating temperature [72]. The author selected the AZ2070 negative photoresist from the AZ20XX series. This phenoplast photoresist presented a high optical absorption in the ultra violet (*UV*) spectrum (Figure 4.4a). Where the absorption peak matches part of the emission spectra of mercury-vapor (Hg) arc lamps (Figure 4.4b). Specifically, the AZ2070 absorption peak corresponds to the Hg i-spectral line emission, 365 nm. Hence, the h-line (405 nm) and g-line (436 nm) are partially absorbed but the diffraction effect produced in the photoresist was negligible. The Hg emission peaks, 546 nm and 579 nm, were filtered in the MJB-3 optical system with a cold mirror and only the i-spectral line passed through the complete system due to a 365 nm interference filter [74].

The final thickness of the selected resin relies upon the deposition method. The photoresist layers were spread on the samples using a spin coater. Moreover, the negative photoresist thickness strongly depends on the viscosity of the phenol-based resin. The most suitable parameters found for the spin coater deposition for our applications were: an acceleration ramp of 1300 $\pm$ 20 rpm, a spinning speed of 2850 $\pm$ 5 rpm and a process time of 20.0 $\pm$ 0.1 s. The process was repeated twice to ensure the homogeneity of the deposited photoresist. The resin specifications present a wide thickness range from 6 to 15 µm for the AZ nLOF 2070 negative photoresist [75]**.** However, with the stated process parameters, the substrates were covered with a 7.0 $\pm$ 0.5 µm thick resin layer. Furthermore, thinner layers could be developed by mixing

the photoresist with acetone. Small amounts of acetone dissolved into the resist, induce a viscosity change, the greater the acetone content, the lower the viscosity value. Nevertheless, the viscosity variation produced radial inhomogeneities on the sample surface, leading to a cone like layer distribution. Therefore, no acetone was used during the formation of the photoresist layers.

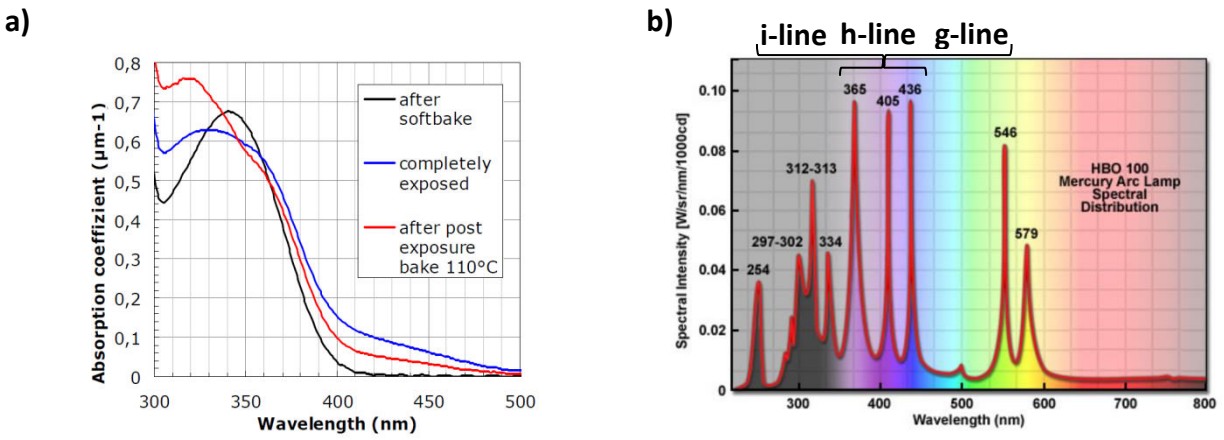

Figure 4.4: a) Optical absorption of the AZ nLOF 2070 negative photoresist **[75]** and **b)** spectrum of a Hg-vapor arc lamp **[76]**.

The deposition of the photoresist layer composed different processes. The surface of the samples was cleaned with a nitrogen (N_2) flow followed by a baking process at 105 ± 2 °C during 60 ± 2 seconds to desorb the water attached to the surface. A posterior cooling down with a nitrogen flow was performed. The entire surface of the substrate was covered with resin once the samples were placed in the spin coater. A short period of time, 30 ± 2 seconds, was allowed for the photoresist to spread and homogenize throughout the sample before, between and after the two-cycle spinning process. Following the spin coater process, a pre-baking process was carried out. The sample was heated up to 105 ± 2 °C during 7.0 ± 0.1 min. During this process, the sample was protected with a cover to avoid dust contamination. A N_2 flow was used to cool down the sample to room temperature afterwards. For the AZ2070 photoresist a rehydration waiting time is not required [75], but in the long-term (up to 24 hr.), the epoxy behavior deteriorates dramatically. Hence, all lithography processes were carried out within minutes between pre-baking step, UV illumination, post-baking step and layer development.

Different lithography masks were designed for the fabrication of micrometer-sized solar cells. The masks for the round-shaped solar cells were tailored to be fabricated by the Technische

Universität Berlin (*LM01#1-4*) and by the E. Rose Fotomasken Mikroelektronik company (*LM02#1-3*). Additionally, lamellar-shaped patterns were tailored to be fabricated by PVcomB (*PVcomB#50* to *#400*, in steps of *#50*) (Further details in Appendix II-2). The photoresist structure was modified by illuminating the sample through the desired lithography mask. In addition, the sample or pre-patterned sample was aligned with the help of alignment marks included in the lithography masks. Furthermore, the gap between the sample and the mask was reduced gradually and the position of the sample was corrected to match the mask marks. A thin air layer was induced in the final approximation of the sample to the mask, where the position of the sample referred to the marks was complicated to maintain. Therefore, due to the lithography process accuracy, there was a mismatch between different patterns, some of which were slightly displaced from the expected positon (Figure 5.8). Hence, during the overlapping of a pre-patterned substrate and the subsequent lithography mask some areas were well positioned and others not, producing short-circuited solar cells.

The photoresist was illuminated during 50 ± 1 s and after the UV irradiation procedure, a post-bake process was carried out. The sample was heated up to 110 ± 2 °C during 2.0 ± 0.1 min. During this process, the sample was protected with a cover to avoid dust contamination. A N_2 flow was used to cool down the sample to RT. Following the post-bake, the non-developed photoresist was removed in an AZ developer bath. The sample was submerged in the solution during 2.25 ± 0.10 min. The solution was slightly stirred during this period to ensure the removal of the non-developed photoresist. The patterned substrate was cleaned with deionized water and dried with a N_2 flow. Depending of the lithography pattern used, positive (+) or negative (-) type, the imprinted pattern had an edge with a truncated-cone (+) or an inverted truncated-cone (-) shape in the case of the round-shaped masks or a truncated-pyramid (+) and an inverted truncated-pyramid (-) in the case of lamellar-shaped masks.

Once the pattern was developed, two types of hard coating were induced for different purposes. A short-term hard bake was employed to ensure the layer stability against the Piranha-based etching solution. A long-term hard bake was induced to isolate the molybdenum layer from the subsequent layers, avoiding possible short-circuits of the solar cell. Other layers for electrical isolation were investigated (Further details in Appendix II-2), but the best

performances were obtained with the use of the AZ2070 photoresist. The samples were heated from room temperature to 133 ± 2 °C during 10.0 ± 0.1 min for the short-term case and cooled down without being removed from the hot plate, which was switched off once the heating time was over. The samples with the isolation layer were heated up to 200 ± 5 °C during 10.0 ± 0.1 min with an identical cool down process as the short-term hard bake. The processed samples were cooled down during 1.0 ± 0.1 hour.

To remove the undesired photoresist, samples were submerged in a DMSO solution during 60 ± 10 s. The bath was slightly stirred during this period to ensure the complete removal of the resin.

4.2.7. Etching process

Different solutions were investigated to etch selectively the CIGSe absorbers. Only limited literature references contained methods to pattern CIGSe material. The most extended method was with a bromine-based (*Br*) solution, either for surface finishing or for defects removing [77] or for bulk material etching [78]. Nevertheless, due to the Br toxicity, other etching mixtures were investigated such as Aqua Regia-based and Piranha-based solutions. The Aqua Regia-based solution was composed of a mixture of hydrochloric acid (*HCl*) (*Sigma-Aldrich, 32% purity*) with nitric acid (HNO_3) (*Sigma-Aldrich, 65% purity*) [79]. CIGSe material was removed by this technique; nonetheless, the back contact was completely etched. Therefore, the molybdenum layer was removed, impeding the connection of the back contact layer, i.e. the extraction of the photo-generated current. Moreover, to prevent electrical isolation of the back contact of the cell due to the etching treatment, another solution was investigated. The Piranha-based [80] solution used, was a mixture of sulfuric acid (H_2SO_4) (*Carl Roth, 96% purity*) with hydrogen peroxide (H_2O_2) (*Th. Geyer, 30% purity*). Despite the fast etching kinetics, the mixture was dissolved in distilled water (H_2O). However, the etching ratio was selected to remove the absorber material within seconds without damaging the protecting layer. A 2:1:1 ratio for H_2SO_4, H_2O_2 and H_2O, respectively, was found suitable for material removing. The reactivity of the etching solution decreased with time, being stronger after mixing the chemical products and weaker after a longer period. In this case, the same batch of samples was used and processed

with the same solution. The etching process was visually controlled; a white colored layer appeared on the molybdenum surface when the solution reaches this layer. This sudden color change was due to the solution of the $MoSe_2$ layer produced during the selenization process. The $MoSe_2$ layer reacted with the Piranha-based solution being dissociated into Mo and Se_2, which bound with O_3 and H_2, respectively. Moreover, the molybdenum trioxide (MoO_3) was responsible for the final colored layer, apart from the contribution of the light white H_2Se bubbles generated during the etching before reaching the pure Mo. The etching time for the first samples was below 10 seconds and up to 60 s for the last samples of the batch. Only the exposed CIGSe areas not protected with photoresist were removed. The photoresist was partially time-resistant against this chemical bath after the short-term hard bake process and was removed easily with a DMSO solution or acetone.

4.3. Conclusions

In this work, micrometer-sized $Cu(In_x,Ga_{1-x})Se_2$ solar cells were fabricated for concentration purposes by different techniques, the combination of lithography and chemical etching processes being the most suitable for solar cell miniaturization.

The accuracy of the lithography process and the kinetics of the etching bath influenced the final size of the active area of the cells. Two trends were clearly observed for shaded and etched cells. The first, for shaded solar cells, produced larger diameters or widths than the expected values and the second, for etched solar cells, induced smaller sizes. This opposite behavior influenced the minimum achievable size of the fabricated cells. Thus for round-shaped solar cells, the minimum diameter achieved was 30 µm for shaded cells and 50 µm for etched absorbers.

Chapter 5:

Characterization

5.1. Introduction

Finally different micrometer-sized solar cell arrays were produced by etching or shadowing the absorber. Different sizes were fabricated and characterized, 23 diameter types and 7 identical sizes per sample for the round-shaped solar cells and 5 width types and 7 identical sizes for the lamellar-shaped solar cells. The characterization methods used to measure the morphology, the element composition and distribution and the electronic properties of the fabricated solar cells are detailed below. These characterization results are used in the thermal-opto-electronic simulations performed in Chapter §6.

5.2. Characterization techniques

5.2.1. SEM characterization

Morphology characterizations were manly determined with a scanning electron microscope (*SEM*) (*Zeiss, Gemini II*) by B. Heidmann. All SEM pictures presented in this work were formed by detecting back scattering electrons coming from the sample in study.

5.2.2. Element composition (EDX) and distribution (GDOES) characterizations

The element composition and distribution was determined by two techniques: energy-dispersive X-ray spectroscopy (*EDX*) and glow-discharge optical emission spectroscopy (*GDOES*).

5.2.2.1. Element composition (EDX) characterization

The analytical method to determine the elemental composition of the sample was characterized by EDX (*Zeiss, Gemini II*) by B. Heidmann collecting different re-emitted X-rays from the excited elements. The depth of the X-rays penetration depends on the energy of the incident beam and the density of the material in study. In the same manner, the spatial resolution was related with both parameters. Typical depths for chalcopyrite absorbers are up to 500 nm for 10 keV energetic incident beams. Monte-Carlo simulations using high acceleration voltages reported a large excitation volume and a low spatial resolution [81].

5.2.2.2. Element distribution (GDOES) characterization

The depth distribution of the elements was measured by GDOES (*Spectruma, GDA 650*) by the group of C. Kaufman ablating the surface of the absorber and measuring the X-rays re-emission of the excited elements ejected during the etching. The depth distributions were obtained as a function of the ablation time, well known for this material and technique.

5.2.3. Electrical (PL, IV-T, I-V) characterization

For the electrical characterization, different techniques were used: photoluminescence (*PL*), current-voltage characteristic curve as a function of the temperature (*IV-T*) and as a function of the concentrated light (*I-V*).

5.2.3.1. PL characterization

PL measurements, and the posterior analysis, were determined at room temperature conditions by J. A. Marquéz Prieto, where the solar cell was illuminated by a 660 nm laser with the equivalent power to one sun. Furthermore, the illumination on the sample corresponded to the amount of photons absorbed by the cell if irradiating with the AM1.5G spectrum. PL measurements were calibrated with an absolute photon hyperspectral imaging setup; hence, the PL yield can be obtained from the photoluminescence light.

5.2.3.2. IV-T characterization

IV-T characteristic curves were measured in a cryostat (*CryoVac*) in four-point configuration by A. Villanueva Tovar. The cryostat integrated a sample holder which was heated while a constant

flow of liquid nitrogen cooled down the sample to obtain the desired temperature. A solar simulator (*Oriel, VeraSol*) with LED light sources was used to simulate the AM1.5G solar spectrum. The light intensity was fine-tuned by adjusting the light intensity of the LEDs. Current-voltage (*I-V*) measurements were performed in a temperature range from 320 K down to 100 K in steps of 10 K. I-V curves were analyzed and fitted using the one-diode circuit model under dark light and illumination and the two-diode model for 6 suns [42]. The series and parallel resistances were neglected in light I-V curves. Therefore, the ideality factors (*n*) were estimated from the dependence of the short-circuit current and the open-circuit voltage obtained for each light intensity and temperature. Ideality factors close to the unit represent thermionic emission, below two mainly corresponds to Shockley-Read-Hall (*SRH*) recombination and above for tunneling by field emission [82] [83].

5.2.3.3. I-V characterization under concentrated AM1.5G illumination

A steady state system based on xenon lamp technology was used for I-V characterization under concentrated light. Through the use of reflectors, special air mass filters and integrating optics light beam properties were modified to achieve CPV solar simulator Class AAA system specifications. Standard specifications for solar simulators for photovoltaic testing were defined by the ASTM Interational (*E927-10(2015)* [84]) and the solar simulator performance requirements were determined by the International Electrotechnical Commission (*IEC 60904-9 2nd Edition* [85]). A modified *PET SS50AAA* solar simulator (*C-SoSim*) was employed to characterize micrometer-sized solar cells, which was capable of tuning the concentration factor from 1 sun up to 130 suns within a wide concentration range (Figure 5.5a). This cell testing device fulfills the requirements specified under Class A: the non-uniformity of the irradiance over the area of illumination must be ≤ 2%, the short term temporal instability of irradiance must be ≤ 0.5% and the long term temporal instability of irradiance must be ≤ 2%, and the spectral match must be ± 2.5% or better respective to the AM1.5G spectrum. Besides those requirements, and to complain with STC specifications, the total intensity was 1000 W/m^2 for the AM1.5G spectrum but the cell temperature was 20°C (*STC-20°C*) instead of the standard temperature, 25°C. In addition to the internal concentration factor feedback, an external power meter (*Thorlabs, S314C*) was used to ensure the desired light flux on the cell. Furthermore,

homemade optical filters were developed to tune the light intensity smoothly. The optical system was composed of stacked substrates of thin borosilicate glass [86]. Depends on the required attenuation, the selected filter was filled with a certain amount of slides to produce the expected absorption of light. Additionally, an active cooling device was incorporated to the setup to keep the temperature of the solar cell at room temperature. Moreover, the positon of the solar cell respect to the solar simulator and lens system was controlled by a 6-axis-parallel kinematic positioning system (*Newport, HXP50 Hexapod*). This equipment allowed a minimum motion step of 0.1 µm, 0.1 µm, 0.05 µm, 0.005 mdeg, 0.05 mdeg and 0.1 mdeg for the 6-axis (*x, y, z,* θ_x, θ_y, θ_z), respectively. The Hexapod was controlled by referencing its position with the lens holder, where three measuring probes (*Keyence, GT2-P12K*) defined the lens holder plane. By correcting the plane of the solar cells, a smooth approximation to the holder plane was performed. Here, the output of the solar cell was measured in each movement to find out the highest short-circuit current position, which corresponds to the best alignment point. I-V characteristic curves were measured by contacting the front metal grid and the back contact with point probes (*Cascade, DPP105-M-AI-S probe positioner + SQ-155-264-01 needles*). Measurements using a single-point contact at the terminals provide I-V curves with a lower fill factor and therefore, a lower efficiency respective to a measurement where two-point contacts are used [87]. Moreover, single-point contacts primarily cause a reduction of the FF but can also reduce the V_{oc} and J_{sc} measured values. The back contact terminal was covered with indium to ensure a good ohmic contact between the point probe and the material. In addition, the point probes used to measure the I-V characteristic curves were an alloy of beryllium and copper. The light flux was adjusted by measuring the I-V curve of a calibrated monocrystalline silicon solar cell (*ISE/S Brachmann*) to comply with STC. For higher concentration factors, an external power meter (*Thorlabs, S314C*) was used to control the irradiation on the solar cell. The maximum illuminated area provided by the C-SoSim was a 50 x 50 mm^2 surface.

The following methodology for I-V measurement was used to characterize the solar cells performance under concentrated light. Before measuring the I-V characteristic curve, 1.0 ± 0.1 s stabilization time was taken to avoid any interference coming from the internal solar simulator mechanism (shutter, filter wheels, lamp stabilization). 120 points along the I-V curve were

evaluated with an integration time of 1 ms for each measurement. The averaged time in which the solar cell was being measured rose to 3.0 ± 0.1 seconds: stabilization time, integration time, number of points and electronics stabilization.

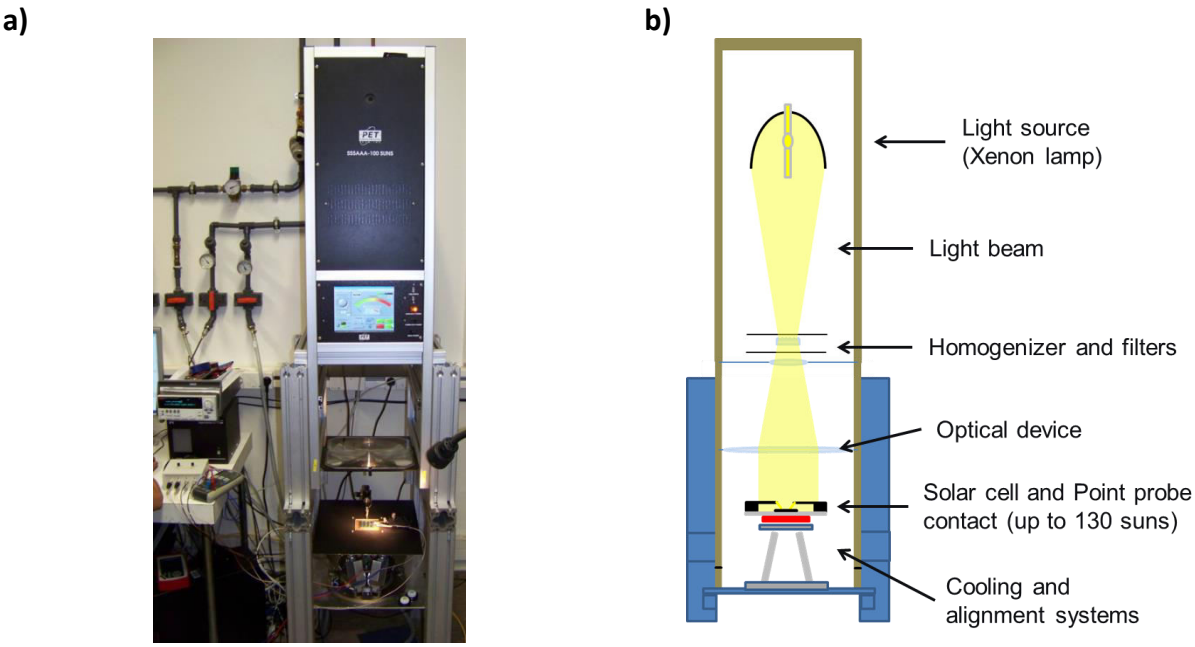

Figure 5.5: a) Modified PET SS50AAA solar simulator for I-V measurements under concentrated light and **b)** the sketch of the selected setup.

Based on the capabilities and limitations of the C-SoSim, there was no possibility to measure the I-V characteristics shining light only on the solar cell without the addition of a suitable micrometer-sized lens array. Hence, the active area of the solar cell and the surrounding surface were illuminated during the measurement. Thermal simulations reproducing the measurement setup exhibited a thermal evolution upon time and applied concentration factor for the selected solar cell (see Chapter §3, section 3.3.4). Therefore, the increasing temperature with time will affect considerably the PV performance. I-V characteristic curves will be influenced by rising undesired heat. This temperature increment can be avoided using a flash lighting system to prevent unwanted heating during the measurement. However, due to the available resources, a steady state solar simulator was used to perform PV characterizations. To minimize the effect of heating in the I-V basic parameters, the I-V curves were measured by varying the terminal voltage from a positive value to a negative value during the measurement time. Lower FF values, therefore efficiencies, were expected to be measured in such conditions. Another possibility to reduce the effect of heating during the measurement was characterizing each

point of the I-V characteristic curve individually. However, due to the characteristics of the solar simulator, the stabilization time, the number of points and the amount of solar cells to be measured, the author opted for a complete and continuous characterization of the I-V dependence at once.

5.3. Characterization results

5.3.1. SEM measurements

SEM pictures were analyzed for the different process steps for the round- and lamellar-shaped absorbers and solar cells. Due to the lithography process accuracy, the alignment tolerances and the etching kinetics, the real solar cell diameter or width differed from the defined sizes of the lithography masks. Figure 5.6a shows the expected (*LM02#1*) and the measured (*AZ2070*) diameters of the photoresist deposited on the absorber material, prior to be etched and after the developing process. The solar cell diameters were found to be greater than the expected values for sizes smaller than ∅ 100 µm and to be smaller for patterns above that value. This behavior could be explained due to the near-field diffraction of the coherent illumination through the aperture of the lithography mask. The distance between the mask and the absorber was defined by the thickness of the deposited photoresist, in this case, 7.0 ± 0.5 µm thick. The Fresnel diffraction approximation of the near-field [88] could explain the tendency shown in Figure 5.6a rather than the far-field diffraction. But with the exception of the measured diameters below 100 µm, the near-field diffraction explains such behavior. Figure 5.6b depicts the expected (*LM02#2*) and measured diameters of the resulting absorber material available after the shading process (*Shaded*) and after the etching process (*Etched*). The resulting sizes of the shaded solar cells were bigger than the expected ones; here, the diffraction in the near-field range of the incident light through the negative of an aperture produces a wider pattern. The lithography pattern LM02#1 was inverted with respect to the LM02#2 mask. Therefore, the diffraction effect was supposed to be the opposite for each case; the first with narrow round-shaped patterns and the second with wider diameters. Figure 5.6c-Shaded depicts the area increment as a function of the expected diameter, where a trend was clearly observed. The

deviation between the expected areas and the measured increased linearly (up to 14%) for large diameters and gradually (up to 50%) for small sizes.

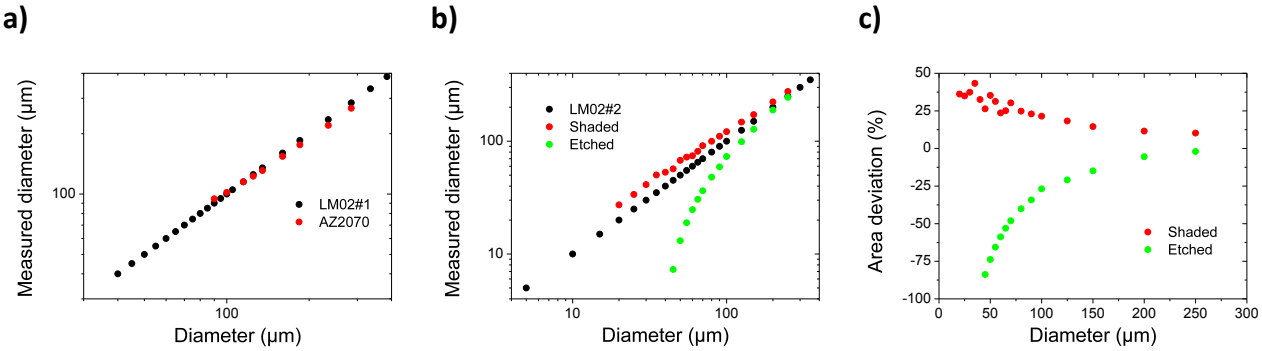

Figure 5.6: a) Expected (*LM02#1*) and measured (*AZ2070*) diameters of the deposited photoresist on the absorber material after the developing process, **b)** expected (*LM02#2*) and measured diameters of the resulting absorber material available after the shading process (*Shaded*) and after the etching process (*Etched*) and **c)** area deviation respect of the expected values for round-shaped shaded (*Shaded*) and etched (*Etched*) solar cells.

Figure 5.6b-Etched shows the SEM measurements of the available absorber material after the etching process. By comparing The trend found was linearly dependent on the previous pattern (*LM02#1*), where a minimum value was experimentally observed. No solar cells with a diameter less than 50 µm were obtained due to the lateral etching kinetics. The depth of the lateral etching was determined by comparing the different diameters of the photoresist pattern deposited to protect the CIGSe material and the available absorber material after the etching process. The etching ratio normal to the absorber surface was approximately 8 times lower than its perpendicular, i.e. 1.7 $\pm$ 0.1 µm depth vertical etching versus 13.7 $\pm$ 1.3 µm depth lateral etching. A reason to explain this behavior could be a preferential etching direction, which may depend on the CIGSe crystalline orientation [89]. CIGSe crystallize in the chalcopyrite structure during the absorber formation. In the experiments, greater lateral etching, in comparison to vertical etching, was observed during the ablation time. Therefore, the absorber material, which remained after the etching process, was smaller than the mask pattern. In Figure 5.6c-Etched, the reduction of the cell area dropped drastically as the size of the cell decreased. This trend depicted a limitation in the fabrication process, where a minimum cell size was produced.

SEM pictures of the selected diameters of the round-shaped solar cells are shown in Figure 5.7a-c for quantitative illustration. The photoresist pattern produced using the lithography mask LM02#1 presented a uniform round-shaped shape and a droplet like geometry (Figure 5.7a).

Nevertheless, the island like shapes were not produced from the surface tension of the photoresist laying on the absorber but due to the effect of the near-field diffraction during the UV curing of the resin. On the other hand, the application of the LM02#2 mask for isolation purposes produced a uniform layer with a smooth edge rather than a sharp profile. The photoresist pattern presented a truncated-cone like geometry in case of using the LM02#1 mask and an inverted truncated-cone like structure if the LM02#2 mask was applied. Round-shaped shaded and etched samples were isolated by patterning the CIGSe surface with the LM02#2 mask. Furthermore, the final cell size was reduced by the isolation mask, decreasing the cell radius by about 9.3 ± 0.1 µm.

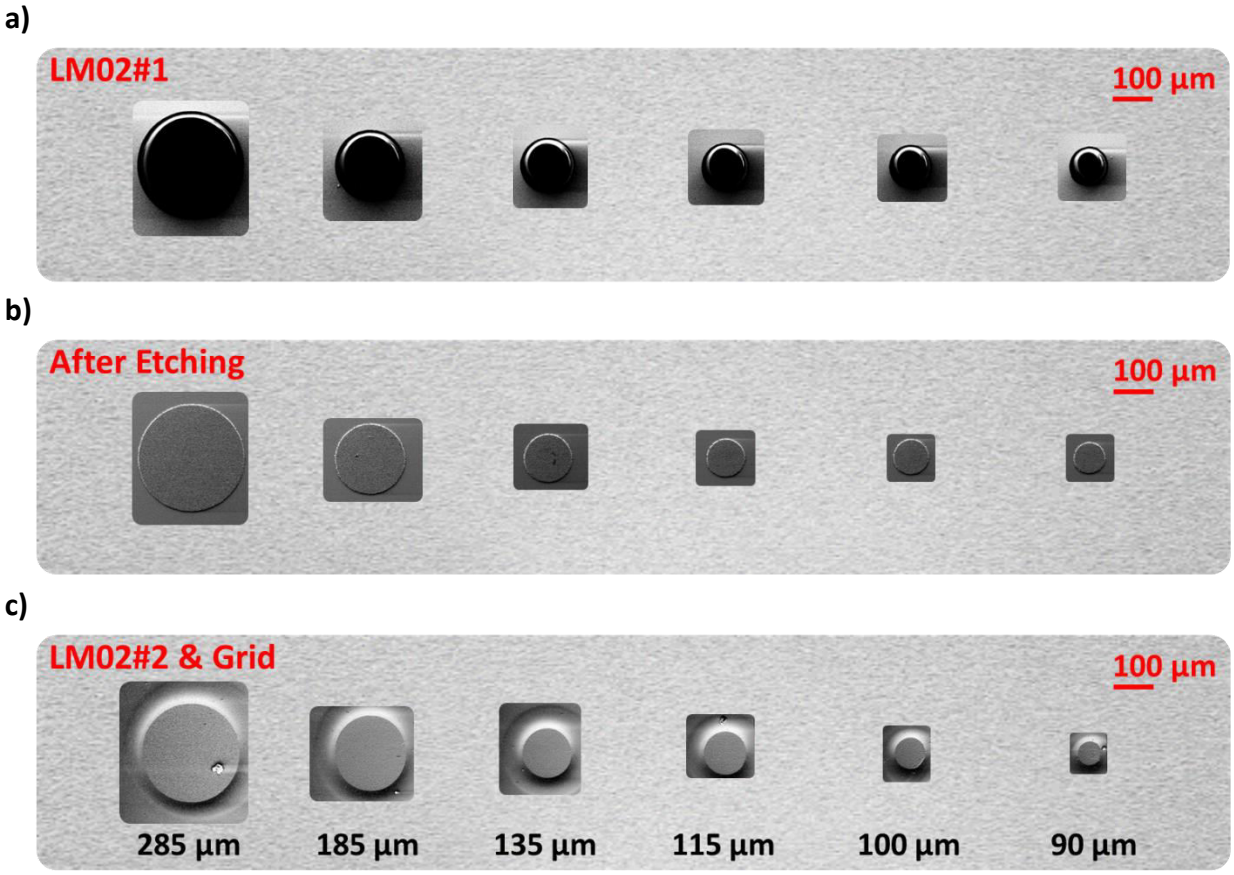

Figure 5.7: SEM pictures of the round-shaped etched solar cells **a)** after the lithography process using the LM02#1 mask, **b)** after the etching process and **c)** after the isolation process using the LM02#2 mask, for the selected diameters: 285 µm, 185 µm, 135 µm, 115 µm, 100 µm and 90 µm.

In Figure 5.7a-c, the progressive area reduction in each process step is shown for the selected diameters: 285 µm, 185 µm, 135 µm, 115 µm, 100 µm and 90 µm. Previously, Paire *et al.* [90] reported chalcopyrite micrometer-sized solar cells produced by a bromine-based chemical

etching, where the etching was not isotropic with a preferential lateral direction. However, the reduction of the cell size due to the lateral etching was about 1 µm in contrast to the values found with our method. Nevertheless, the pH of the solution and the etching ratio was reported to display an important role for the absorber reduction. Hence, and in order to improve the current limitations of our fabrication process, further investigations are necessary to increase the etching capabilities.

To illustrate the degree of misalignment of the lithography process, different SEM pictures are shown in Figure 5.8 for a variety of cell diameters. The selected pictures correspond to a single sample with 23 diameter types and 7 identical sizes, specifically 18 positions are shown. Here, the fabrication tolerances, the effect of the mask-sample interaction and the overlapping resolution between different masks can be appreciated. Regarding the tolerances included, the expected distances between the active area and the Ni/Al grids was approximately half the radius of the cell, which can be appreciated in Figure 5.8. However, the real distance was found to be not symmetrically distributed respective to the cell sides. The overlapping resolution helped by the alignment marks contained in the lithography mask, was found to be below 5 µm. The *xyz* micrometer-platform allowed a fine tune of the cell position referred to the mask. However, the main limiting factor was the approximation of both surfaces. During the elevation of the sample, a thin air film remained between the mask and the sample. By continuing to elevate the sample holder, the interaction between the thin air layer and the sample provoked an uncontrolled movement of the sample. It was found that this movement rotated with respect to a sample corner, where the photoresist used to accumulate due to surface tensions. Furthermore, a vacuum holder was used to prevent any sample movement. However, the forces applied during the sample elevation and the limitations of the vacuum equipment allowed such movements. In Figure 5.8, the effect of the thin air layer was clearly observed for smaller diameters (see positions below #16), where this rotational movement caused the cell-mask overlapping to increase along the same row.

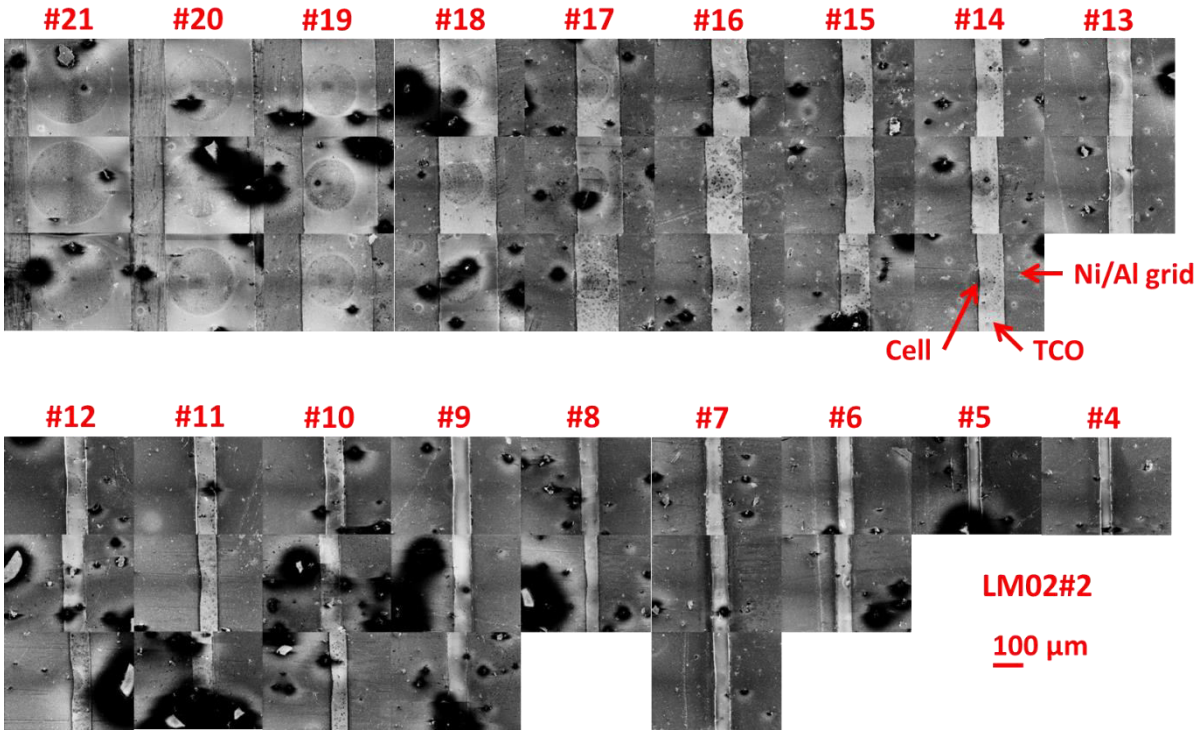

Figure 5.8: SEM pictures of the round-shaped etched solar cells for the selected positions: #21 with ∅ 285 µm, #20 with ∅ 235 µm, #19 with ∅ 185 µm, #18 with ∅ 160 µm, #17 with ∅ 135 µm, #16 with ∅ 125 µm, #15 with ∅ 115 µm, #14 with ∅ 105 µm, #13 with ∅ 100 µm, #12 with ∅ 95 µm, #11 with ∅ 90 µm, #10 with ∅ 85 µm, #9 with ∅ 80 µm, #8 with ∅ 75 µm, #7 with ∅ 70 µm, #6 with ∅ 65 µm, #5 with ∅ 60 µm and #4 with ∅ 55 µm.

In the same manner, lamellar-shaped solar cells were fabricated either by shadowing or by etching the absorber material. For this purpose, different masks were used but the rotational movements were minimized due to the use of large samples. Furthermore, the alignment was improved based on the mask marks and the lamellar-shaped of the pattern, which allowed a fine tune of the sample-mask positon. For qualitative illustrations, Figure 5.9a-b show SEM pictures of the lamellar-shaped shaded and etched samples. All fabricated lamellar-shaped samples had a final width of 140 $\pm$ 10 µm.

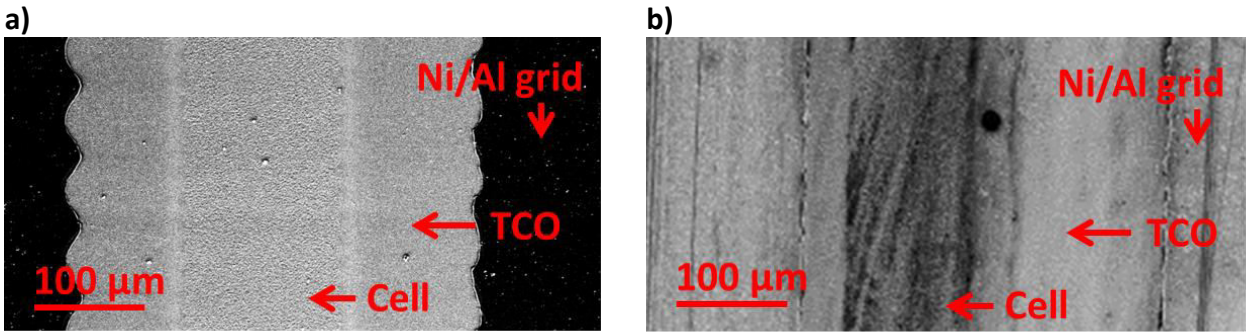

Figure 5.9: SEM pictures of the lamellar-shaped **a)** shaded solar cells using the PVcomB#140 and PVcomB#350 masks and **b)** etched solar cells using the PVcomB#200, PVcomB#140 and PVcomB#350 masks.

Hence, all measurements, where the area of the solar cell influences the results, were corrected with the corresponding cell size measured by SEM.

5.3.2. Element composition (EDX) and distribution (GDOES) measurements

5.3.2.1. Element composition (EDX) measurements

In this work, all superficial EDX results were extended to the entire CIGSe bulk layer. Figure 5.10a-b show EDX characterizations of a round-shaped etched absorber, where the elemental distribution for each of the detected species is depicted. The same absorber was evaluated by measuring the perimeter (Figure 5.10a) and center (Figure 5.10b) distributions of elements. CIGSe compositional characteristics were previously reported for highly efficient solar cells as the CGI (*Cu/(Ga+In)*) and GGI (*Ga/(Ga+In)*) atomic ratio. CGI and GGI ratios in the range of 0.7 to 1.0 and 0.25 to 0.5, respectively, are desirable for the CIGSe formation [6]. In this case, the stoichiometry found in the etched absorber for CGI and GGI were 0.85 and 0.33, respectively, representative of the typical depth of EDX measurements.

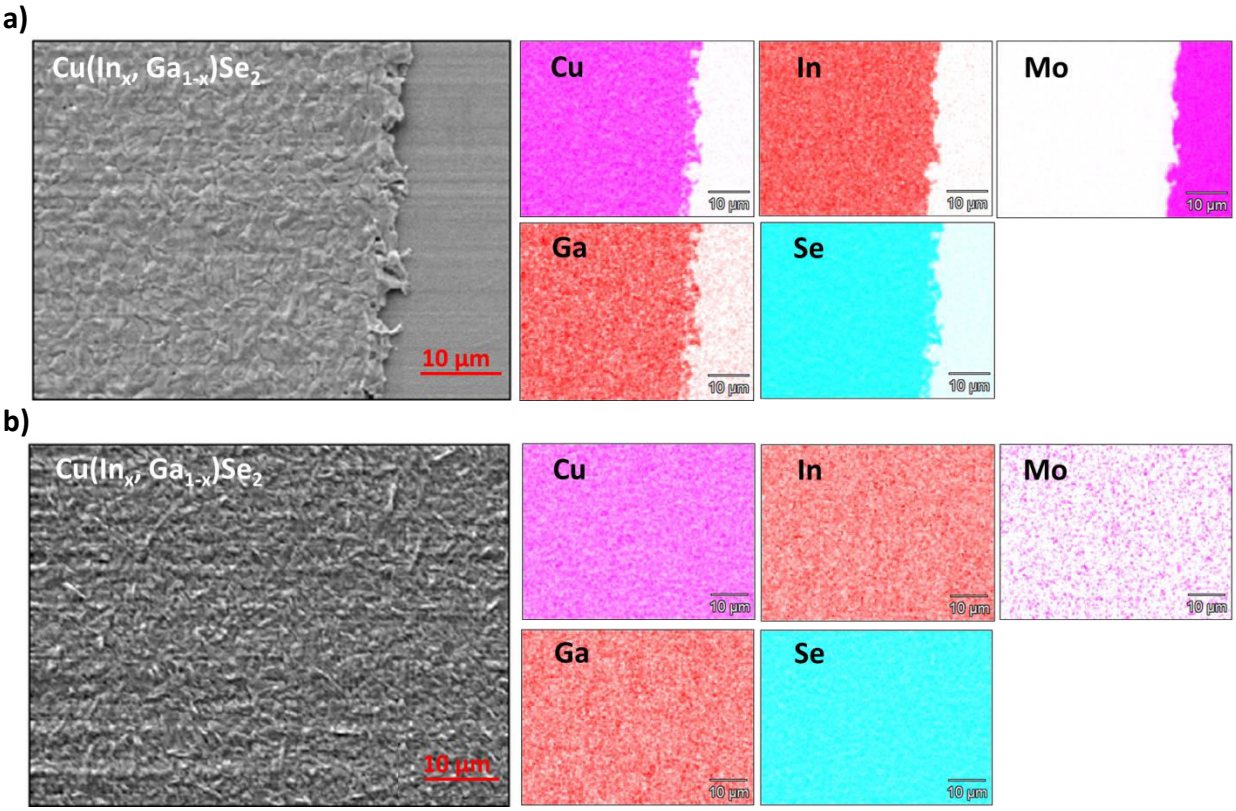

Figure 5.10: EDX characterization of a round-shaped etched absorber **a)** at the edge and **b)** in the middle. SEM picture of the analyzed area and the corresponding results for each detected element: Cu, In, Ga, Se and Mo.

The distribution of copper, gallium and indium elements was homogeneous along the absorber (Figure 5.10a-Cu-Ga-In). However, a slight reduction of the selenium amount at the absorber perimeter was appreciated (Figure 5.10a-Se). A possible explanation for this lack of selenium at the edge could be the effect of the etching solution, which strongly reacts with this element to form hydrogen selenide (H_2Se). This reduction was observed in a 5 to 10 µm wide ring at the edge of the etched CIGSe layer. Therefore, a reduction of the Se content along the perimeter will influence the optical and electrical performance of the solar cell.

5.3.2.2. Element distribution (GDOES) measurements

Control solar cells, i.e. planar references, were fabricated with the same process parameters, avoiding the active area reducing steps. A GDOES analysis was performed to measure the grading of the band gap through the thickness of the reference absorber. A slightly noticeable grading was observed, with a minimum band gap of 1.128 $\pm$ 0.005 eV in a valley centered at 0.575 $\pm$ 0.010 µm from the pn-junction interface. A maximum band gap value resulted at the rear interface of the absorber, 1.261 $\pm$ 0.005 eV at 1.700 $\pm$ 0.010 µm depth, where Ga tends to accumulate [91] (Further details in Appendix II-3).

5.3.3. Electrical (PL, IV-T, I-V) measurements

5.3.3.1. PL measurements

Figure 5.11a depicts the photoluminescence detected for one wavelength. The spectrally resolved image shown, corresponds to the highest PL intensity detected. A PL spectrum with a Gaussian shape distribution centered at 1.132 $\pm$ 0.010 eV and a FWHM of 0.100 $\pm$ 0.010 eV was measured for a solar cell with a diameter of 235 $\pm$ 5 µm (not shown). Moreover, the obtained PL band gap was in good correlation with GDOES measurements. Figure 5.11b shows the estimated PL yield (PL_{yield}) from PL spectrums as described in Chapter §3, section 2.3.

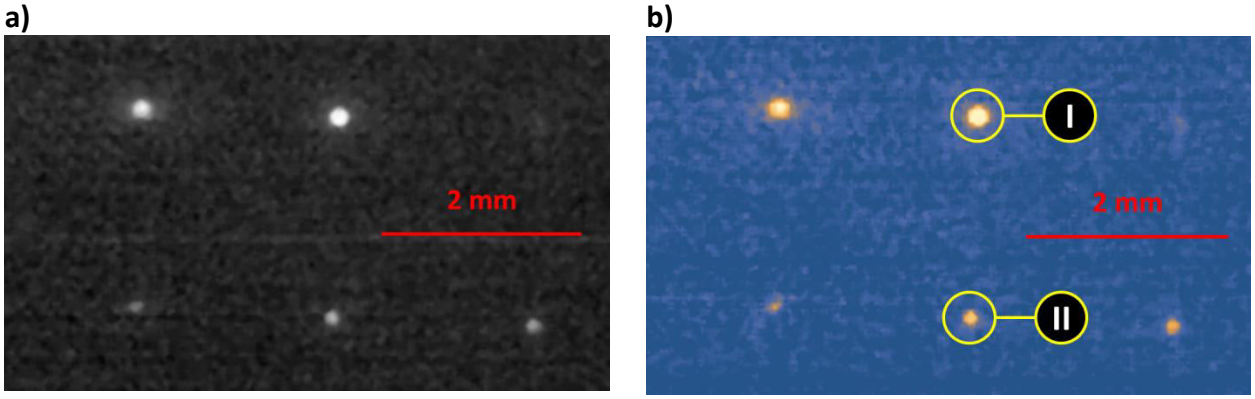

Figure 5.11: PL measurements of the round-shaped etched solar cells, **a)** detected photoluminescence and **b)** estimated PL yield after being illuminated, for the selected positions: #20 with ∅ 235 µm and #19 with ∅ 185 µm,

Modeling the absolute PL spectrums allows the calculation of the quasi-Fermi level splitting (*QFLS*) and the estimation of the maximum achievable open-circuit voltage (Figure 5.12) is feasible [41]. Enlargement of the photoluminescence yield (Figure 5.11b) is depicted in Figure 5.12 for the selected positions: #20 and #19 with a cell diameter of 235 ± 5 µm and 185 ± 5 µm, respectively. *QFLS* was estimated by fitting the high-energy wind of the dependence of the natural logarithm of PL_{yield}/E^2 versus energy (E) [41]. From the obtained slope, the intercept at the *y-axis*, which corresponds to zero energy, provides the quasi-Fermi level splitting for a certain temperature. The value of the slope divided by the Boltzmann constant corresponds to the temperature of the heterojunction. The estimated *QFLS* represents the maximum achievable V_{oc} in the absorber under study. Once measuring full devices instead of absorbers, the open-circuit voltage was expected to be similar to the *QFLS* results.

Enlargement of the PL yield depicted a homogeneous region in the center of the cell and on the edge a reduction in value (Figure 5.12-I). Moreover, for the smaller cell, there was a reduction of the PL yield along the cell radius, where a maximum value was found at the center and a minimum at the edge (Figure 5.12-II). Comparing both cells, a small reduction of the cell diameter provoked a complete different PL yield. Moreover, the estimated *QFLS* of the cells presented a similar behavior, where the larger cell exhibits a truncated-cone like distribution of the V_{oc} and the smaller cell depicted a cone like distribution of the open-circuit voltage. This behavior could be explained by the lack of Se along the cell perimeter due to the etching process. Hence, a Cu-rich perimeter was expected in this area, where the selenium content was reduced. The device performance was reported to strongly depend on the final copper content

of the absorber [92] [93]. Therefore, low-efficiency regions were expected to be present at the absorber perimeter. Opto-electronic properties of the micrometer-sized solar cells were affected by the different fabrication processes; therefore for simulation purposes, additional boundary conditions were necessary to implement to reproduce such behavior on the edges.

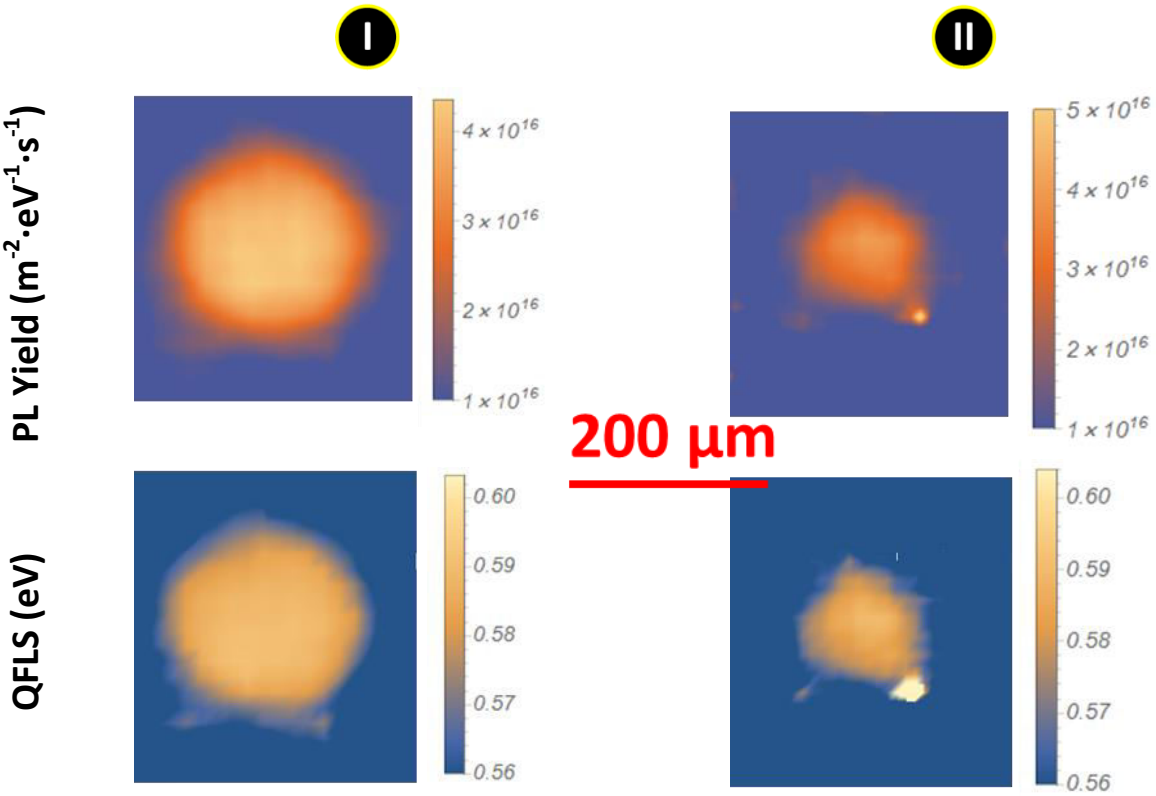

Figure 5.12: PL yield and QFLS estimation for the selected positions: **(I)** #20 with ∅ 235 µm and **(II)** #19 with ∅ 185 µm,

PL measurements estimated the potential of the fabricated solar cells. By improving the optical setup to increase the resolution of the measurement, information in more depth could be extracted from this technique for comparison with other analytical characterizations.

5.3.3.2. IV-T measurements

IV-T characterizations were performed on the sample, measured as in Figure 5.12-I, a solar cell with a diameter of 235 µm (position #20). Light intensity was changed from 10^{-3} suns up to 1 sun; furthermore, concentrated light was applied to the solar cell to simulate an increasing injection regime of photons. The concentration factor was set to 6.0 ± 0.1 suns, the maximum irradiation available without modifying the IV-T characterization tool. As Figure 5.13 show, the open-circuit voltage dependence with the settled temperature increased with the natural

logarithm of the concentration factor. However, the V_{oc} differed when the standard IV-T characterization tool was used and when an optical system was incorporated to concentrate light up to 6.0 ± 0.1 suns. For this case, the increasing irradiation on the cell generated a V_{oc} decrement observed at lower temperatures and higher concentrations. Therefore, the equipment was not able to maintain the cell temperature at the settled illumination during the measurement. Thereby, the characterizations with the modified IV-T setup were not taken into account for temperatures below 220 K.

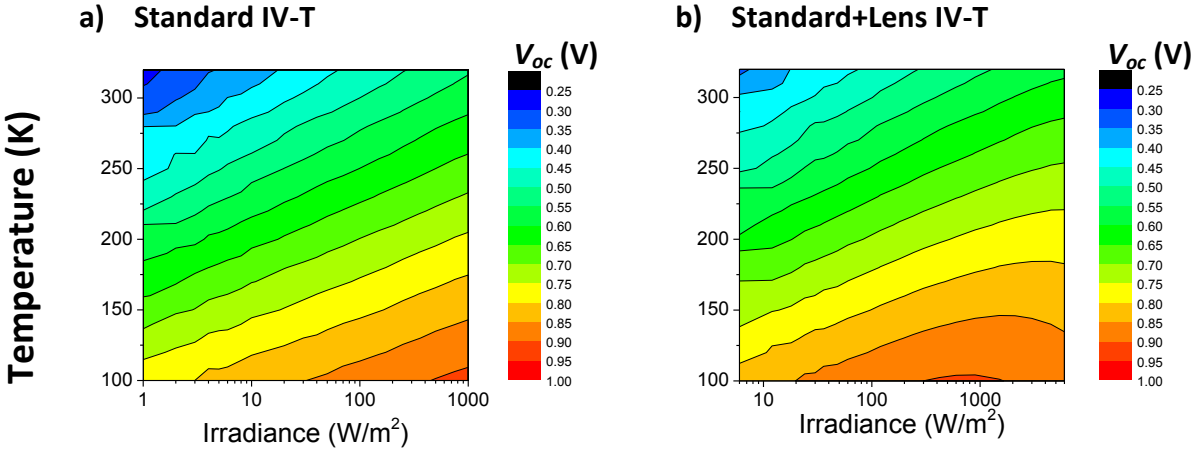

Figure 5.13: Open-circuit voltage dependence with concentrated light by using **a)** the standard IV-T equipment and **b)** with the incorporation of a lens system to concentrate light up to 6 suns.

The evolution of the ideality factor with temperature and concentrated light is shown in Figure 5.14a. The estimation of the ideality factor was obtained as described in Chapter §2, section 2.4, assuming ideal series and shunt resistances. For solar cells under different concentration factors, where the exact value of the temperature was unknown, the temperature of the semiconductor was assumed constant. Therefore, temperature variations will influence the estimated value of the ideality factor. In those cases, obtained ideality factors were only an approximation of the real values. At room temperature, the ideality factor increases with light but for lower temperatures this difference slightly increases. A trend can be appreciated in Figure 5.14a, where the dependence of n with temperature tends to increase the difference between the value of the ideality factor at room temperature and at lower temperatures. Therefore, the expected results with the modified setup should not be over 2. However, and due to the equipment limitations, this assertion cannot be backed up with facts.

The ideality factor was expected to decrease for higher temperatures and concentration factors remaining in range below 1.5. Figure 5.14b shows the estimated ideality factors of the round- and lamellar-shaped solar cells under concentrated light. With the exception of a LSE solar cell and the results estimated for diameters below 50 µm, the ideality factor remains below 1.5 for temperatures above room temperature, as noted before. The n value over 1.5 found for LSE cells corresponded to the worst I-V performance measured (see section 5.3.3.3.2).

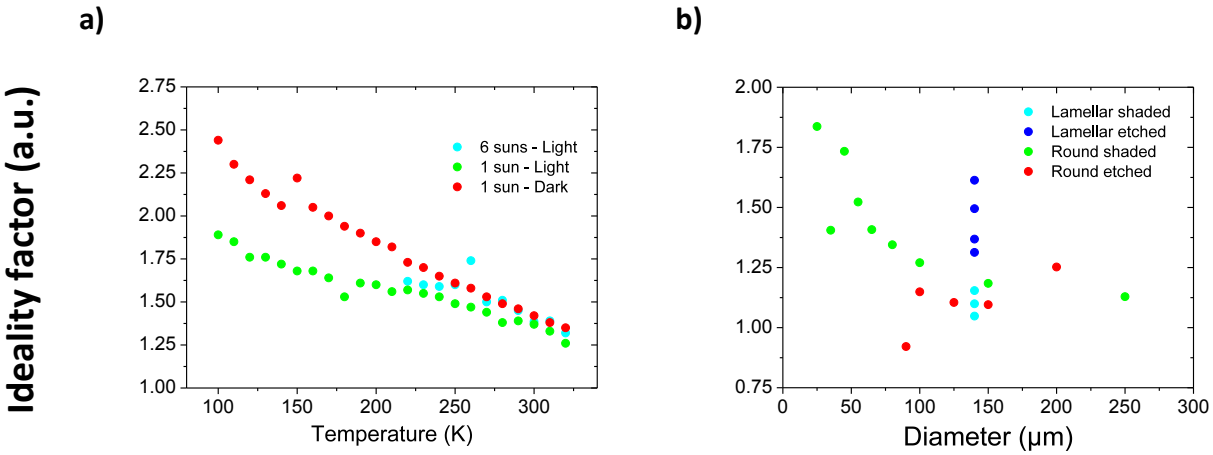

Figure 5.14: Estimated ideality factors **a)** for a solar cell with a diameter of 235 µm for given temperatures and different concentration factors and **b)** for round-shaped and lamellar-shaped solar cells when the absorber was either shaded or etched for different diameters under concentrated light.

Additionally, the estimated values of n for diameters below 50 µm corresponded to cells with low performance respect to the same cell group (see section 5.3.3.3.2). Therefore, under-performed cells were expected to present an increased ideality factor respect to their cell group and in the same manner, the activation energy was expected to follow the same behavior as the ideality factor. Hence, a reduction of the absorption of the incident spectrum was expected due to the increasing value of the activation energy by decreasing cell diameter, i.e. less photo-generation current.

In addition, an opposite trend was found for round-shaped solar cells, which absorber was shaded (*RSS*) respect to etched CIGSe (*RSE*) (Figure 5.14b). The ideality factor was found to reduce with the diameter of the cell in contrast with the behavior presented by RSE cells. Furthermore, shaded cells featured a lower ideality factor than etched samples. A possible explanation for this deviation could be the effect of the lack of selenium at the edge, therefore, recombination mechanisms increased in this region by augmenting the ideality factor.

From the estimated values of the ideality factor, the activation energy (E_A) was extracted from two different methods as described in Chapter §2, section 2.4. In Figure 5.15 the E_A was extracted from the V_{oc} extrapolation, while in Figure 5.15b, the slope of the Arrhenius plot represented by the product of the ideality factor and $ln(J_o/J_{oo})$ versus the inverse of the temperature provided E_A. The estimated activation energies were 1.131 ± 0.050 eV (1 sun) and 1.127 ± 0.050 eV (6 suns) by the V_{oc} extrapolation, and 1.065 ± 0.050 eV, 1.049 ± 0.050 eV and 1.102 ± 0.050 eV by the Arrhenius plot for each characterization (dark IV-T, under illumination: standard IV-T and with an optical system), respectively. For comparison with GDOES and PL characterizations, the obtained value under standard test conditions (1 sun) was taken into account. Therefore, the estimated value was in agreement with previous characterizations of the solar cell. However, the accuracy of the E_A results estimated through the IV-T measurements is low, but its comparison provides useful information. Therefore, E_A results estimated from the V_{oc} extrapolation differed very little between them as of the Arrhenius results. Moreover, even when the ideality factor changes with light and temperature, the activation energy with concentrated light was supposed to remain constant.

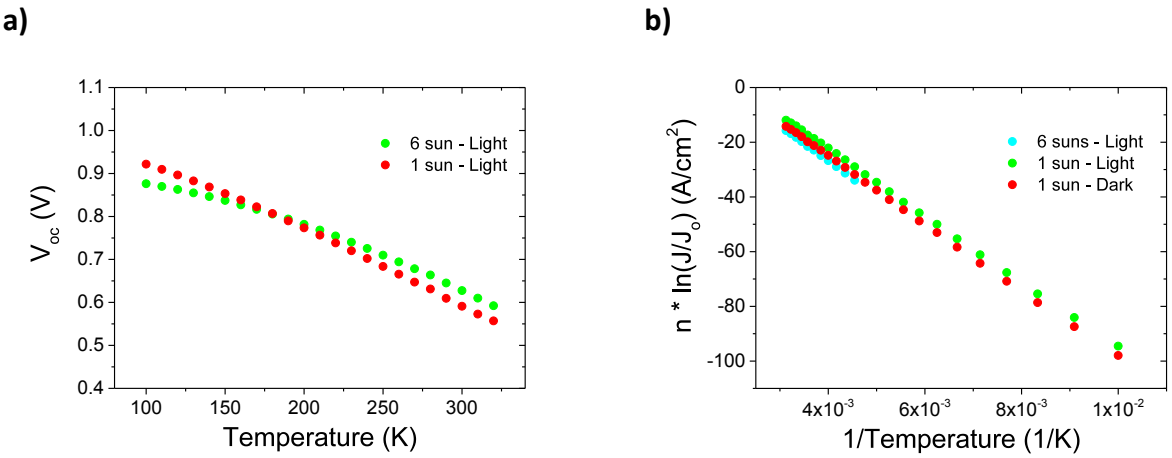

Figure 5.15: Estimated activation energy by **a)** the extrapolation of Voc respect to the solar cell temperature and **b)** the Arrhenius plot represented by the product of the ideality factor and $\ln(J_o/J_{oo})$ versus the inverse of the temperature.

These behaviors observed for the ideality factor influenced the optical and electrical performance of the solar cell and, therefore, they are taken into account in the simulations. Moreover, the ideality factor was assumed constant in the thermal-opto-electronic simulations as a result of these results.

5.3.3.3. I-V characteristic curves

5.3.3.3.1. I-V measurements under AM1.5G illumination

All solar cells, planar, round- and lamellar-shaped, were characterized under standard test conditions at 20°C (*STC-20°C*). Electrical parameters obtained from I-V measurements of planar reference solar cells presented a short-circuit current density (J_{sc}) of 32.8 ± 0.5 mA/cm^2 and an open-circuit voltage (V_{oc}) of 0.647 ± 0.010 V. A fill factor (*FF*) of 70.1 ± 1.1 and a 14.9 ± 0.4% total power conversion to electricity, i.e. efficiency (η), were calculated. In the same manner, round-shaped solar cells were measured. Figure 5.16 depicts the evolution of the open-circuit voltage (V_{oc}) and the short-circuit current density (J_{sc}) as a function of the cell diameter. The open-circuit voltage remained constant for diameters above 100 µm for shaded and etched cells (Figure 5.16-V_{oc}). However, shaded cells presented a lower diameter threshold respect to etched samples, 30 ± 5 µm and 50 ± 5 µm, respectively. Below these values, no sample with such characteristics presented an electrical response. Additionally, the short-circuit current density measured as a function of the cell diameter exhibited the same behavior as the V_{oc} (Figure 5.16-J_{sc}). However, values above 40 mA/cm^2 were unrealistic and above 45 mA/cm^2 impossible to be obtained. Values of the short-circuit current above 40 mA/cm^2 were obtained as a result of an underestimation of the active area of the solar cell. Nevertheless, a clear trend for both types of cell finishing was observed. Firstly, the open-circuit voltages measured for different cell sizes exhibited a gap with respect to obtained values under STC-20°C for reference solar cells. Either the best shaded or etched absorbers presented a drop in V_{oc} in about 5.0 ± 0.6% and 7.0 ± 1.0%, respectively, for larger cells. A first theory that could explain this drop was the current losses through the photoresist layer. The deposited resin was expected to electrically isolate the absorber (shaded) or the back contact (etched) from the posterior layers like CdS and AZO. However, and due to the large area covered by the photoresist with respect to the cell size, the intrinsic resistance of the resin reduced the detected voltages by leaking photo-generated current through it. The space between the front grid and the active area was approximately one half of the cell radius, what corresponds to an area slightly larger than the cell area. Therefore, part of the photo-generated current leaked through this area reducing the cell performance. Nevertheless, due to the alignment tolerances of the lithography process, in

some cases the active area was close to the Ni/Al grid reducing the electrical path between source and collector, thereby, decreasing the electrical losses. Although this argumentation could explain the reduction of the V_{oc} and J_{sc} by decreasing cell diameter, it cannot completely support the behavior of round-shaped etched cells. Moreover, in those cases, the V_{oc} remained below the Ref.SC values, this suggested the presence of another mechanism of loss.

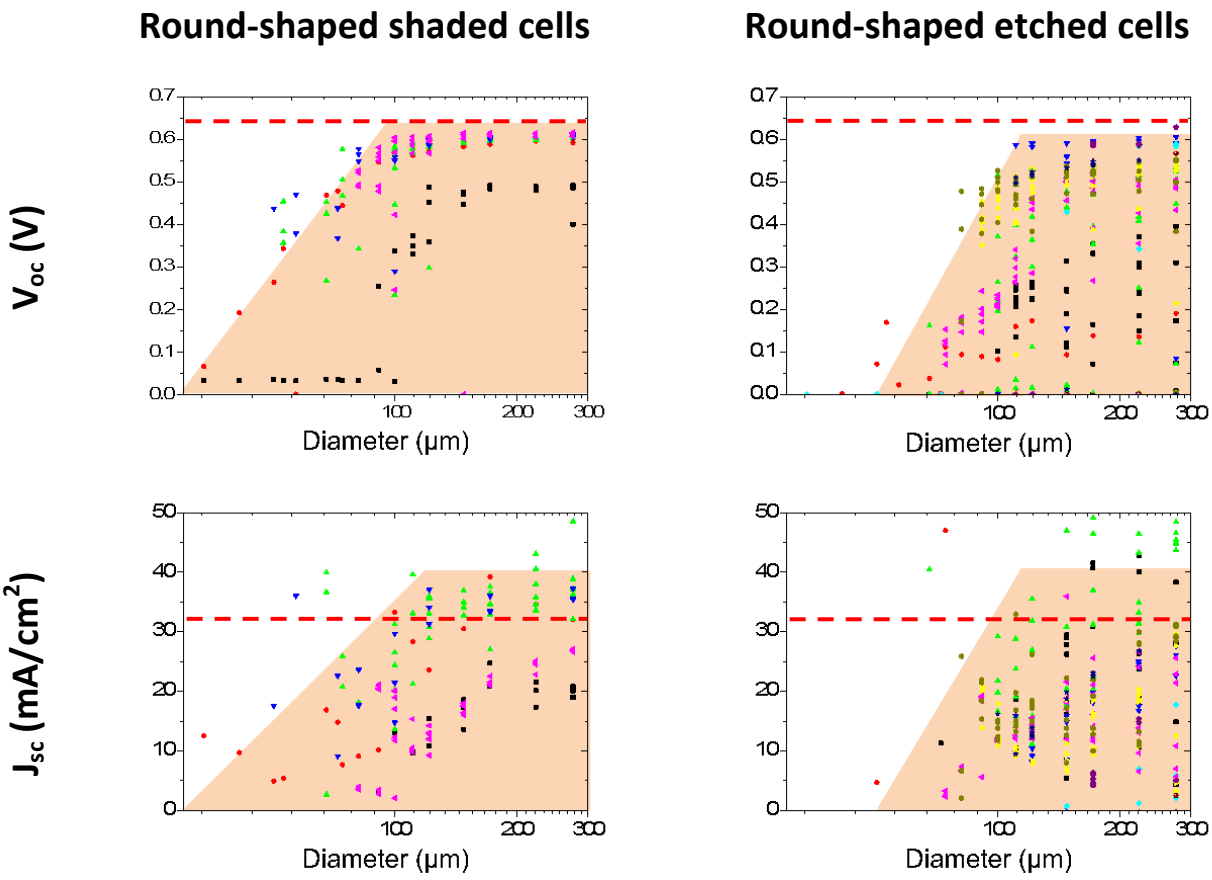

Figure 5.16: Open-circuit voltage (V_{oc}) and short-circuit current density (J_{sc}) measurements as a function of the diameter for round-shaped solar cells (by shadowing or etching the absorber material) under standard test conditions at 20°C. Dashed line corresponds to the values of the reference solar cell. The same color and shape of the different points correspond to solar cells produced in the same sample.

Our hypothesis to clarify the drop in J_{sc} and in V_{oc} is related with the weight of the perimeter recombination with respect to the cell area of the micrometer-sized solar cells the drop in J_{sc} and V_{oc}, was related to the micrometer-sized cell perimeter and the decreasing ratio between the cell area and perimeter with cell minimization (Figure 5.16). The recombination mechanism at the cell edge will affect the overall performance due to an increasing perimeter-area ratio. Furthermore, the relation between the cell perimeter and the PV area correspond to the inverse of the cell radius. The smaller the radius, the more weight the perimeter component has, which

implies more weight of the recombination effect. One reason that could explain the faster reduction of the V_{oc} with respect to the shaded samples was the modification of the absorber band gap. Fluctuations in the Ga content will provoke a decreasing V_{oc} as the In content increases in the $Cu(In_x,Ga_{1-x})Se_2$ solar cell [40]. However, EDX analysis of a round-shaped etched absorber at the edge and in the middle presented an homogeneous distribution of Cu, Ga and In (as seen in section 5.3.2.1). Nevertheless, EDX analysis on the cell perimeter presented a lack of selenium on the edge due to the effect of the etching solution, which strongly reacted with selenium to form hydrogen selenide (H_2Se). Therefore, the reduction of the Se content along the perimeter, i.e. Cu/Se rich perimeter [94], influenced the electrical performance of the solar cell. This reduction was observed in a 5 to 10 µm wide ring at the edge of the etched CIGSe layer in EDX and PL analysis (section 5.3.3.1). The effect of reducing cell area by chemical etching provokes non uniform edges [95] and therefore, the recombination mechanism at the cell edge increases. Moreover, CIGSe defect density is intended to be the main cause of the cell voltage drop, for which a major contribution is due to Schokley-Read-Hall (*SRH*) recombination mechanism [96]. This phenomenon can clarify the reduction of the J_{sc}, V_{oc}, *FF* and implied the overall efficiency of the device with absorber minimization with respect to the reference and the shaded cells. The assumption of a highly localized recombination mechanism at the perimeter of the micrometer-sized solar cell was taken into account for the modelling and was turned out to be appropriate (see Chapter §6).

Another explanation for this behavior could be described by a decrease of the metal work function value (*W*) at the Mo/CIGSe interface in an ideal Schottky contact case. But even when the work function is sensitive to the doping level we will not consider a variation on this parameter to explain the change in the open-circuit voltage. Neither a process nor treatment was performed on such interface.

Figure 5.17 shows the measured values corresponding to the lamellar-shaped solar cells. Here, only one size was investigated as seen in section 4.2. The maximum achievable open-circuit voltage remained constant for the different cells, yet the best shaded or etched devices presented a drop in V_{oc} in about $6.0 \pm 0.8\%$ and $8.0 \pm 1.1\%$, respectively, compared to obtained values under STC-20°C for reference solar cells. As the round-shaped cells, a drop in the V_{oc} was

observed due to the electrical losses through the isolation material and the recombination at the edge. Moreover, the drop in V_{oc} was more pronounced for the etched samples as a result of a higher recombination at the edge, where a lack of selenium was presented. The measured values of the short-circuit current density correlated with those measured for round-shaped cells. There was a slight decrease in the J_{sc} of the etched samples with respect to the shaded samples caused by the edge recombination losses. In the same manner, values of the short-circuit current above 40 mA/cm^2 were unrealistic to be obtained. Therefore, the area for those solar cells was underestimated.

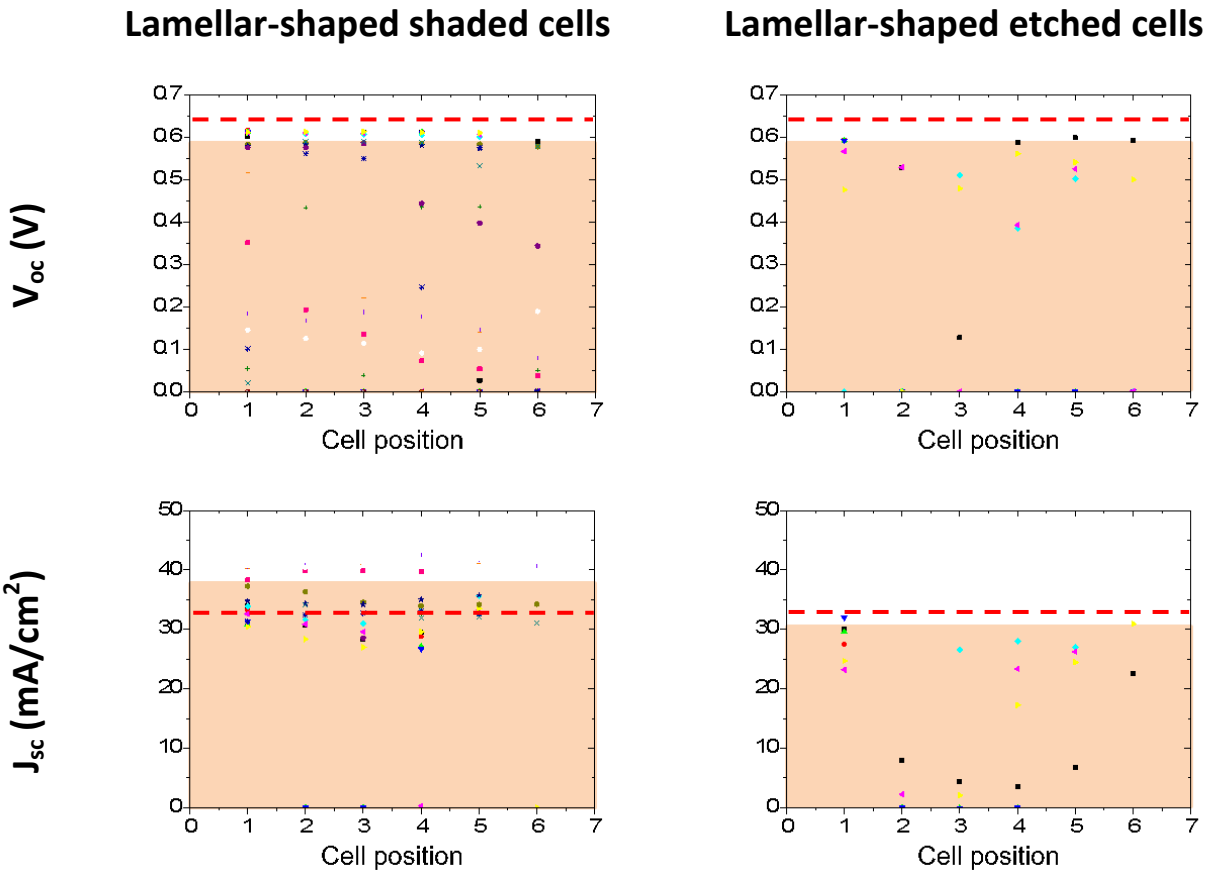

Figure 5.17: Open-circuit voltage (V_{oc}) and short-circuit current density (J_{sc}) measurements for lamellar-shaped solar cells (by shadowing or etching the absorber material) under standard test conditions at 20°C. Dashed line corresponds to the values of the reference solar cell. The same color and shape of the different points correspond to solar cells produced in the same sample.

This behavior, observed for round-shaped and lamellar-shaped solar cells, needs to be taken into account into the opto-electronic simulations. The hypothesis of a higher Shockley-Read-Hall recombination mechanism along the perimeter of the cell needs to be confirmed. Hence, the

electron lifetime at the edge of the absorber decreases, diminishing the solar cell performance and the weight of the SRH recombination increases by reducing the cell diameter.

5.3.3.3.2. I-V measurements under concentrated AM1.5G illumination

I-V characteristic curves were measured under concentrated light, as described in section 5.2.3.3, for the solar cells with the best performance under STC-20°C.

Round-shaped solar cells

In Figure 5.18, the open-circuit voltage and the short-circuit current density are shown as a function of the concentrated light for different PV sizes. Regarding the V_{oc}, a comparable trend was observed for each cell size, where the voltage under STC-20°C correlated with the behavior seen in previous section (5.3.3.3.1). The V_{oc} increased with the logarithmic of the concentration factor up to 50x, yet for diameters of the solar cell below 100 µm, the evolution of the V_{oc} with concentration was affected by the recombination mechanisms (Figure 5.18-V_{oc}). A hypothesis that could explain this behavior was the net reduction of the recombination losses with concentration by enhancing the measured V_{oc}. The open-circuit voltage increased with concentration reaching a maximum value in the range of 40x to 50x and in the range of 20x to 40x for shaded and etched cells, respectively. The limitations of the C-SoSim, as mentioned in section 5.2.3.3, avoided the sole illumination of the active area of the solar cell. Therefore, the cell area and surroundings were illuminated increasing the total amount of energy on the sample. This increase of energy provoked a thermal heating of the cell augmenting the temperature with respect to the initial settings (see Chapter §3, section 3.3.4). Hence, one possible explanation of the maximum V_{oc} achievable could be the effect of the temperature on the cell performance. The temperature increase at low concentration factors (<10x) was limited, but above the temperature of the cell increased drastically (see Chapter §3, section 3.3.4). This temperature evolution with concentration was supposed to affect not only the open-circuit voltage, but also the fill factor, the conversion efficiency and to a lesser extent the short-circuit current density. Apart from the temperature evolution of the device under concentrated light, EDX and PL characterizations revealed the effects of Piranha-based etching featured in a 5 to 10 µm wide ring at the edge of the etched CIGSe layer. The shortage of selenium, affected the

electrical performance of the solar cell which also explained the difference in numbers of the maximum open-circuit voltage for shaded and etched cells. Micrometer-sized solar cells with a higher recombination mechanism, i.e. etched devices, presented a maximum achievable V_{oc} in a lower concentration range.

A linear evolution of the short-circuit current density under concentrated light was observed (Figure 5.18-J_{sc}). As shown before, a trend of the J_{sc} as a function of the diameter of the cell was noted. Here, the effect of the recombination, on the edge, with cell minimization in the final performance, increased as the cell size decreased. Therefore, the electrical losses provoked J_{sc} values lower than the Ref.SC and even lower as the diameter decreased. Regarding the J_{sc}, no upper limitation with concentration was found with the available characterization tool.

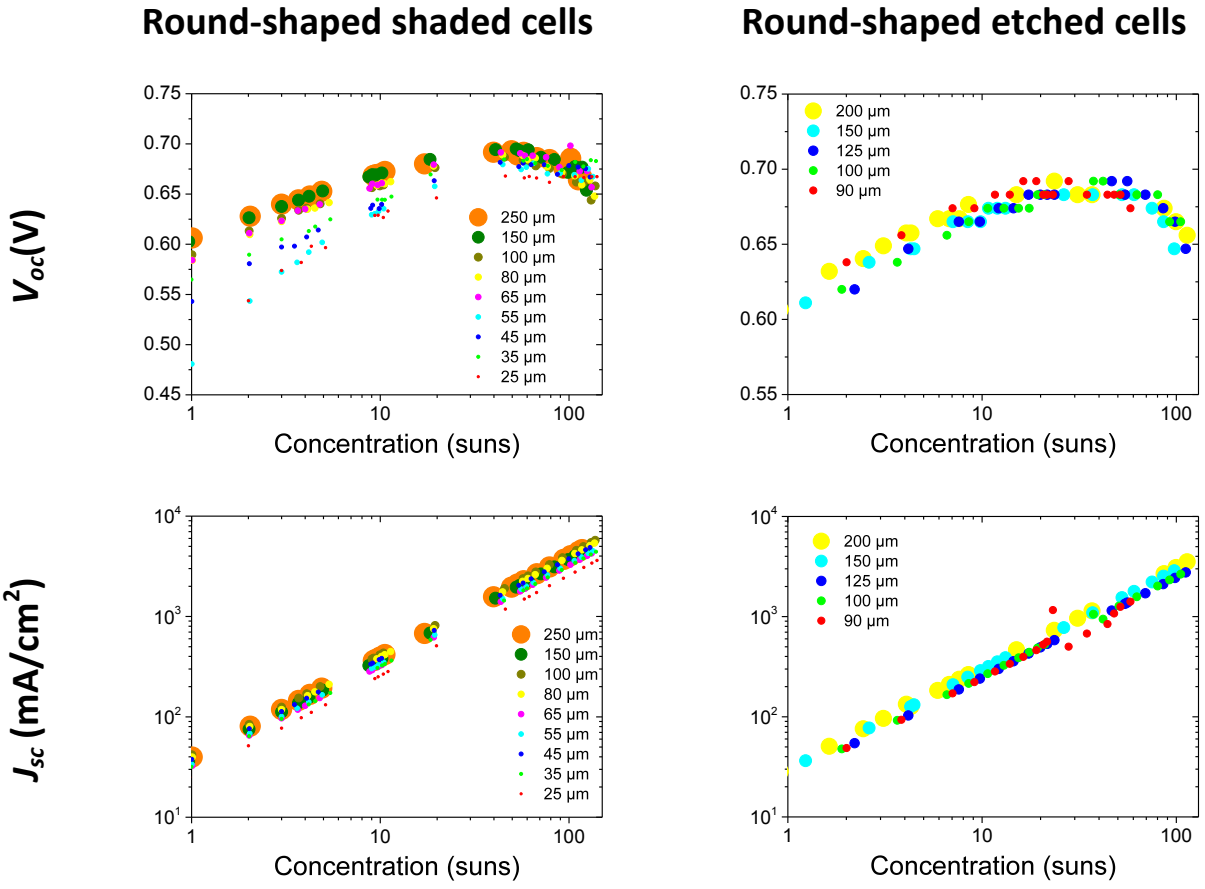

Figure 5.18: Open-circuit voltage (V_{oc}) and short-circuit current density (J_{sc}) measurements for round-shaped solar cells (by shadowing or etching the absorber material) under concentrated light under standard test conditions at 20°C.

Figure 5.19 depicts the efficiency and the fill factor dependence with concentrated light for shaded and etched absorbers. The total power conversion to electricity, i.e. efficiency, increased

with concentrated light reaching a maximum value in the range of 20x to 50x and in the range of 20x to 30x for shaded and etched cells, respectively (Figure 5.19-η). However, the smaller the diameter of the solar cell, the lower the maximum efficiency reached. Large cells were desirable for concentration applications with the current fabrication techniques and characterization setup. Whether for shaded or etched absorbers, the maximum efficiency available with concentration was reduced by reducing the area of the cell. The experimental results presented a 3.7 ± 1.9% absolute and 25.3 ± 12.5% relative increment of the efficiency for the best micrometer-sized solar cell (∅ 250 µm) by shadowing the absorber with respect to its performance under STC-20°C. Also, the absolute and relative increment of the efficiency for the best etched device (∅ 200 µm) was 2.1 ± 1.4% and 14.0 ± 9.7%, respectively, compared to its performance under STC-20°C. Therefore, even when there was no material saving by shading the cell absorber, the total power conversion to electricity approximately duplicated the best results of the etched samples. However, this tendency was opposite to that published by Paire *et al.* [97] [78], where shaded cells (∅ 50 µm) presented a maximum efficiency in the range of 200x to 500x with an absolute and relative increment of 5.0% and 23.5%, respectively. Moreover, etched samples (referred as mesa diodes by Paire *et al.* [78]) (∅ 25 µm and ∅ 40 µm) exhibited a maximum over 1000x with 2.0% absolute and 11.5% relative increment of the efficiency compared to its value under STC. One of the reasons argued was the homogeneous etching using a bromide solution, which leaves a stoichiometric surface after the process. In this case, with the selected chemical bath (as referred in section 4.2.7), there was a selective etching process, and it explained the measured trends opposite to what Paire *et al.* [97] [78] published.

Regarding the fill factor evolution with concentrated light, the calculated value of the selected etched cells was remarkably greater than the planar reference (*Ref.SC*), specifically a 12.4 ± 1.3 % increment (Figure 5.19-FF). This increment was reflected in the efficiency values that increased in the same manner. The basic parameters were in agreement with the Ref.SC except for the fill factor. Although, the same behavior was measured in different characterization equipment, no theory was found to explain this phenomenon. However, the basic parameters obtained for the shaded cells were in correlation with the measured for the reference solar cells. Moreover, if this increment of the *FF* is deducted from the experimental measurements,

the fill factor was a slightly higher but quantitatively comparable. Figure 5.19-FF show the evolution of the fill factor under concentrated light. Here, a slight increment in the *FF* was observed with concentration reaching a maximum in the range of 20x to 50x for the shaded cells. Moreover, in this case, by reducing the diameter of the shadowing of the cell, the *FF* was reduced by up to 50% of its value. In the case of etched cells, the FF presented its maximum under STC-20°C and decreased slightly with concentrated light. For diameters of the cell below 100 µm, the *FF* was comparable to the Ref.SC value.

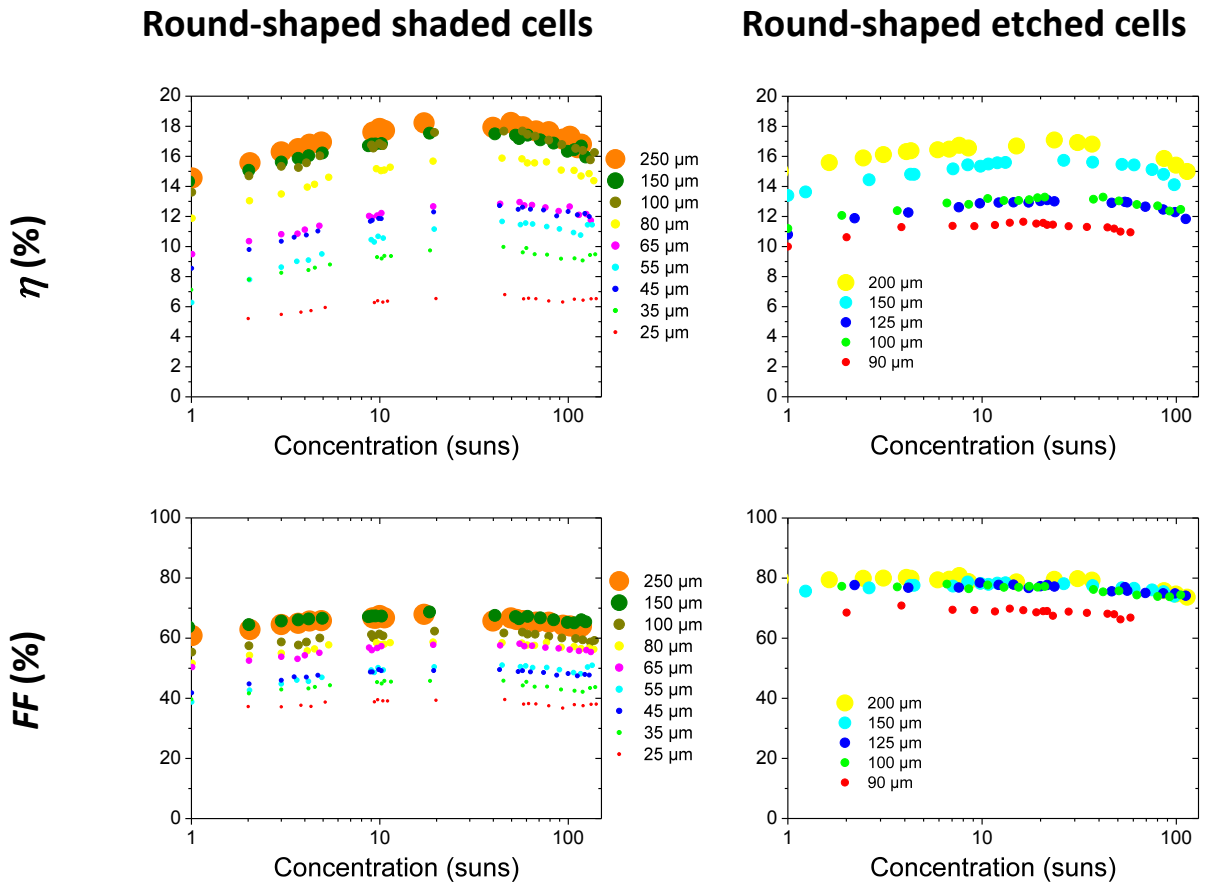

Figure 5.19: Efficiency (η) and fill factor (*FF*) measurements for round-shaped solar cells (by shadowing or etching the absorber material) under concentrated light under standard test conditions at 20°C.

The evolution of the series and shunt resistance with concentration was depicted in Figure 5.20. A linear dependence of the natural logarithm of the concentration and the natural logarithm of R_s and R_{sh} was observed. However, the slope of the R_{sh} was more pronounced than of the R_s. Figure 5.20-R_{sh} shows the shunt resistance dependence with concentrated light. R_{sh} decreased with concentration; nonetheless, the result of multiplying R_{sh} by the concentration factor showed an increasing value with concentrated light. On the other hand, the reduction of the R_s

was expected as a consequence of the energy conservation law. To complain with this law, Joule heating produced by the passage of an electric current through a resistance cannot be greater than the total energy. Hence, by increasing the concentration factor, the photo-generated current increases and, therefore, the current through the solar cell. As shown in Figure 5.18-J_{sc}, a linear dependence of the J_{sc} with concentration was observed, which provoked a necessary reduction of the series resistance by the square root of the concentrated light. Moreover, the power loss by Joule heating remained below 3% of the incoming power for all types of solar cells.

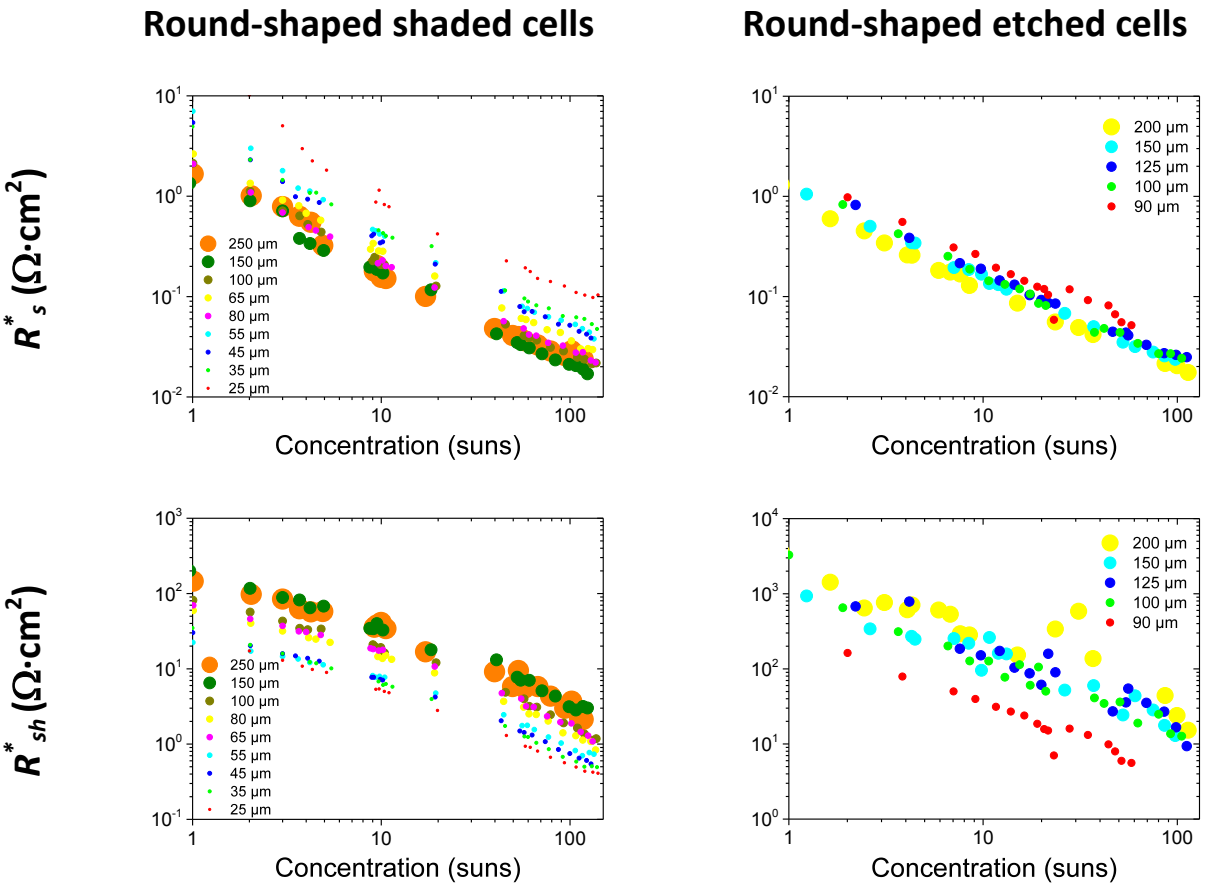

Figure 5.20: Series resistance (R^*_s) and shunt resistance (R^*_{sh}) measurements for lamellar-shaped solar cells (by shadowing or etching the absorber material) under concentrated light under standard test conditions at 20°C.

A close approximation to the observed dependence of the R_s with C was described by *Paire's* equation [45][45] (2.24) and observed by Lotter *et al.* [29] for CIGSe solar cells. However, the series resistance is one of the major limiting factors for CPV technology [98]. Therefore, efforts to reduce the effect of this parameter in the cell performance were carried out, developing a suitable metal grid on the front contact to properly extract the photo-generated current by

minimizing R_s [99]. This progress allowed a tremendous increase in the concentration of light on III-V solar cells by boosting the concentration factor from 500x to over 1500x without penalizing the performance of the cell. Therefore, by designing a suitable metal grid for the micrometer-sized solar cells, it is expected to observe a remarkable increment in the concentration capabilities.

Lamellar-shaped solar cells

Apart from the variety of round-shaped solar cells, lamellar-shaped solar cells were produced. In this case, only a sole width type was fabricated, 140 ± 10 µm. The basic parameters evolutions with concentrated light were presented in the following figures. The overall behavior of these parameters was similar to the observed in the previous section. Specifically, in Figure 5.21, a comparable trend was observed for V_{oc} and J_{sc} as a function of the concentration factor. Here, the maximum V_{oc} achievable was found in the range of 40x to 90x and in the range of 40x to 60x for shaded and etched cells, respectively (Figure 5.21-V_{oc}). Unlike what was observed for round-shaped solar cells, the maximum V_{oc} achievable was found in a higher concentration region due to a lower temperature of the cell during the measurement (see Chapter §3, section 3.3.4). Hence, these behaviors supported the benefits of cell miniaturization, where an improved heat management allowed higher concentration factors. Moreover, these results highlighted the fact that a suitable illumination needs to be implemented by measuring the I-V characteristic curves with the current setup to avoid undesired heat coming from the surrounding illuminated area as well as a suitable etching process to minimize the effect of a higher recombination mechanism at the cell perimeter due to the presence of a lack of Se.

In Figure 5.21-J_{sc}, the short-circuit current density is depicted under concentrated light. Here, the effect of the recombination at the edge with cell minimization was expected to remain invariable for different widths of the solar cells. The cell perimeter was considered as a constant, because the length of the cells was orders of magnitude larger than the width (> 100x). Therefore, a slightly decrease in J_{sc} was expected with the minimization of the width of the cell but this assertion cannot be backed up with facts.

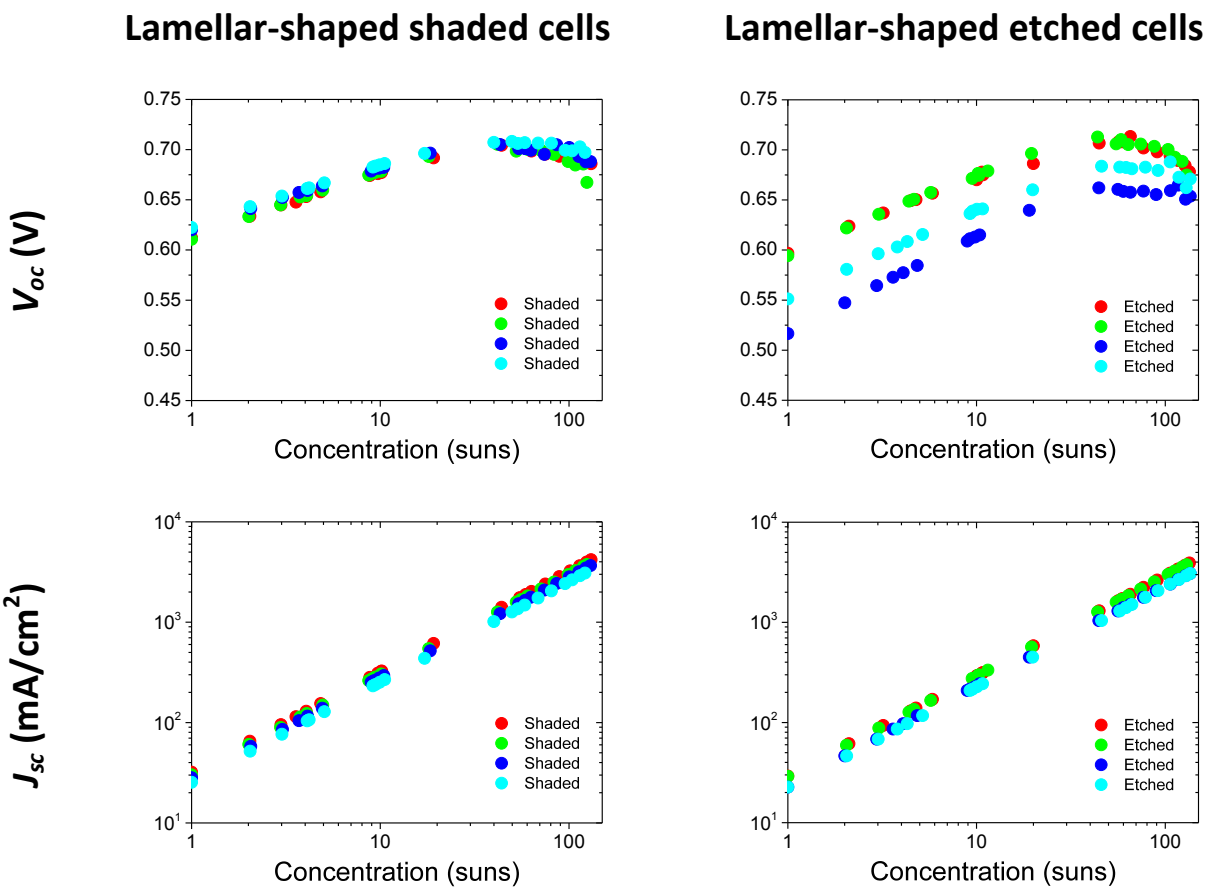

Figure 5.21: Open-circuit voltage (V_{oc}) and short-circuit current density (J_{sc}) measurements for lamellar-shaped solar cells (by shadowing or etching the absorber material) under concentrated light under standard test conditions at 20°C for lamellar-shaped solar cells with a final width of 140 ± 10 µm. The different colors of the different points correspond to different lamellar-shaped solar cells.

Regarding the cell efficiency evolution with concentration, it reached a maximum value in the range of 10x to 40x and in the range of 20x to 40x for shaded and etched cells, respectively, compared to its value under STC-20°C (Figure 5.21-η). The experimental results showed a 1.3 ± 0.4% and 1.8 ± 0.4% absolute and 10.9 ± 3.3% and 14.6 ± 3.1% relative increment of the efficiency, with respect to its value under STC-20°C, for the best lamellar-shaped solar cell produced by shadowing or by etching the absorber, respectively. Whether shaded or etched cells, the calculated *FF* was in agreement with those reported from the reference solar cells. The evolution of the fill factor with concentration slightly increased, reaching a maximum in the same range as in the efficiency dependence, to slightly decrease to a *FF* value below the initial level under STC-20°C.

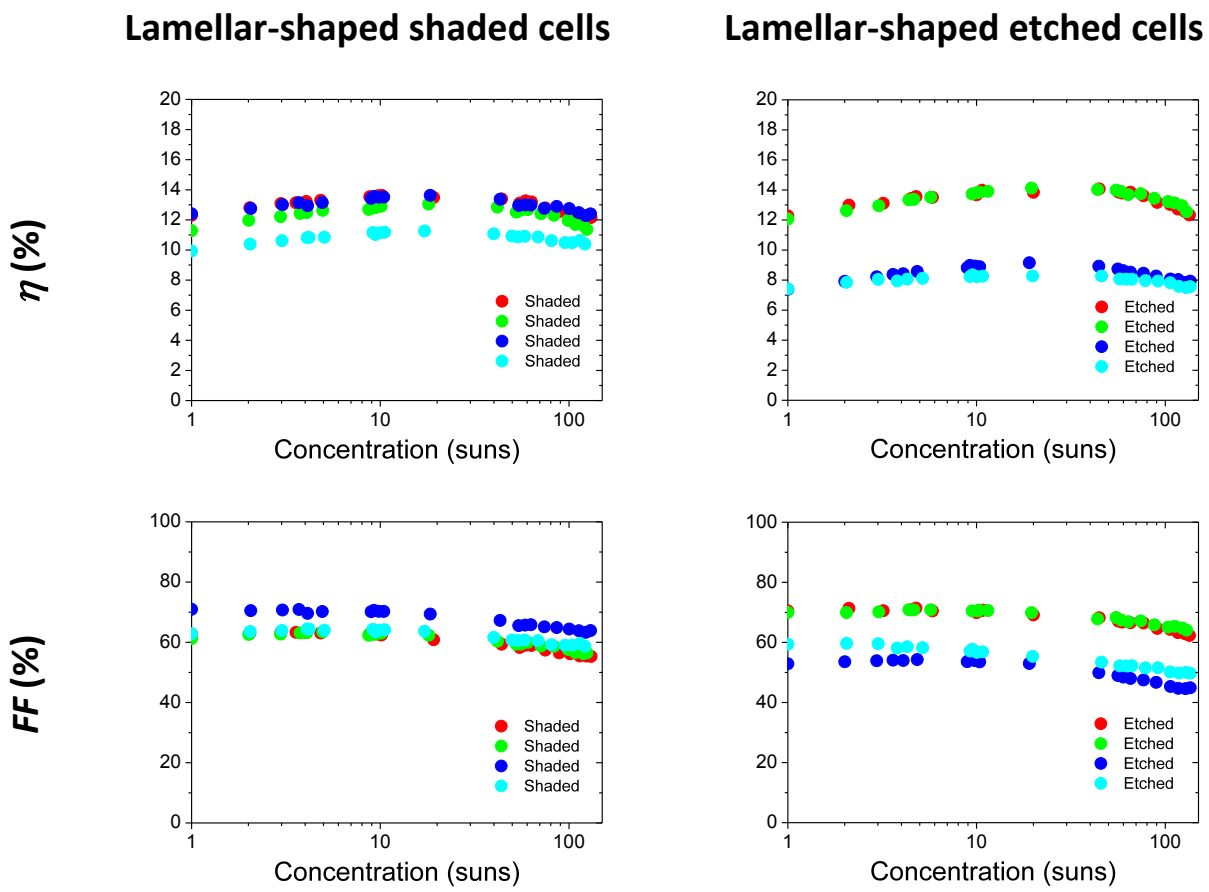

Figure 5.22: Efficiency (η) and fill factor (*FF*) measurements for lamellar-shaped solar cells (by shadowing or etching the absorber material) under concentrated light under standard test conditions at 20°C for lamellar-shaped solar cells with a final width of 140 ± 10 µm. The different colors of the different points correspond to different lamellar-shaped solar cells.

As referred to before, the evolution of the series (Figure 5.23-R_s) and shunt resistance (Figure 5.23-R_{sh}) with concentration presented a linear dependence when the natural logarithm of the resistance was plotted as a function of the natural logarithm of the concentration. Here, the same behavior was observed, where the decay factor of the R_{sh} was more pronounced than of the R_s.

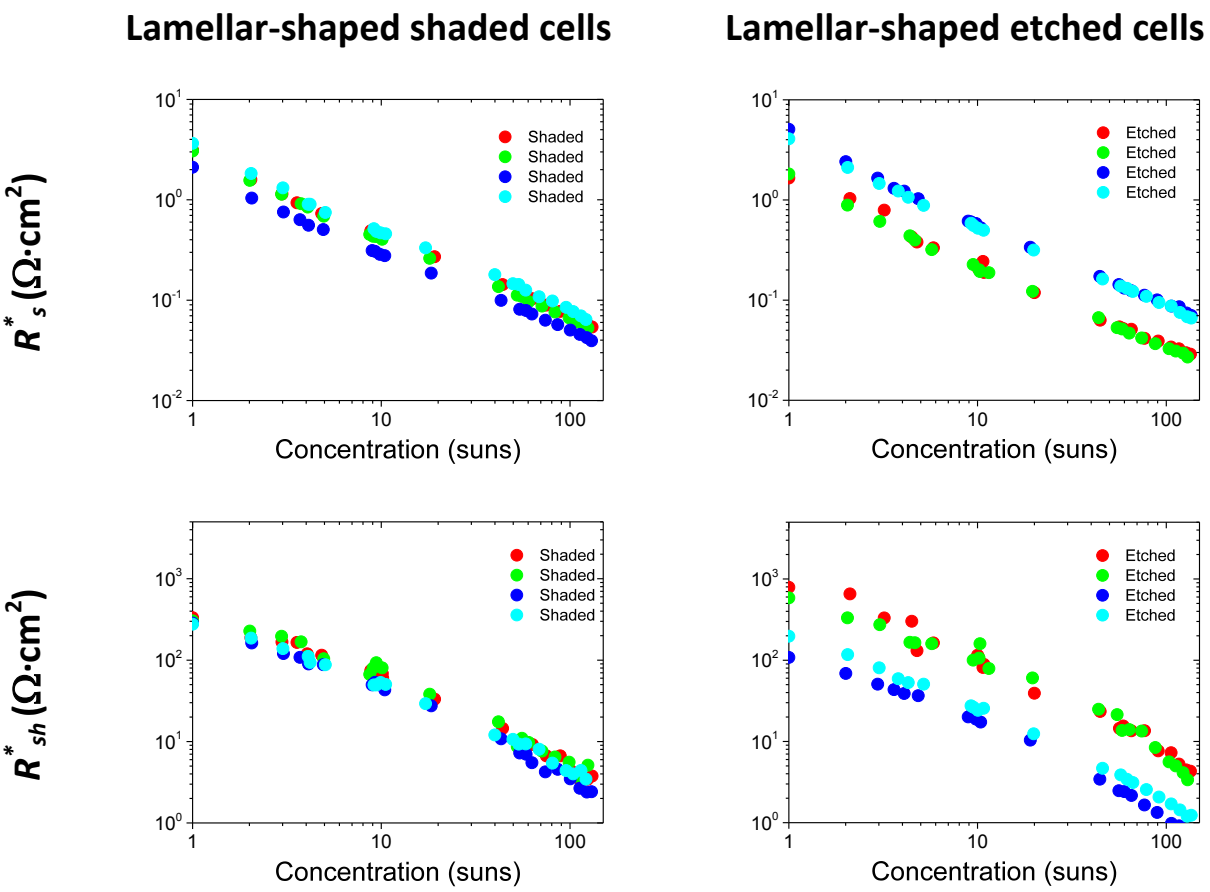

Figure 5.23: Series resistance (R^*_s) and shunt resistance (R^*_{sh}) measurements for lamellar-shaped solar cells (by shadowing or etching the absorber material) under concentrated light under standard test conditions at 20°C for lamellar-shaped solar cells with a final width of 140 ± 10 µm. The different colors of the different points correspond to different lamellar-shaped solar cells.

5.4. Conclusions

I-V characteristic curves under STC-20°C presented a moderate deviation with respect to the reference solar cells, specifically, for round-shaped solar cells, the open-circuit voltage dropped in about 5.0 ± 0.6% and 7.0 ± 1.0% for shaded and etched cells, respectively. The short-circuit current density presented a drop of 4 ± 0.5% for shaded cells and 10.0 ± 1.4% for etched cells. The fill factor presented an increase of 12.5 ± 1.3% with respect to those values of Ref.SC for etched cells. Therefore, the efficiency was in agreement with the presented for the reference solar cells. For lamellar-shaped solar cells, the open-circuit voltage, for shaded and etched cells, presented a drop in about 6.0 ± 0.8% and 8.0 ± 1.1%, respectively. The short-circuit current density presented 7.0 ± 0.9% drop for shaded and etched cells. The calculated fill factor correlated with those values of the reference solar cell. However, the final efficiency was

affected by the drop in V_{oc} and I_{sc}, decreasing in about 13.5 ± 1.3% compared to those values of the reference solar cell. A hypothesis to explain this behavior was related with the distance between the active area and the metal grid to collect the photo-generated electrons. The greater the distance, the greater the probability for an electron to be recombined. Therefore, the current losses through the photoresist layer, which covered a large area with respect to the size of the micrometer-sized solar cell, explained the behavior found for shaded cells. But the gap presented for etched cells was explained with the addition of another loss mechanism. EDX and PL characterizations revealed the real effects of etching with a Piranha-based solution, where a lack of selenium along the absorber perimeter was observed. The shortage of selenium, featured in a 5 to 10 µm wide ring at the edge of the etched CIGSe layer, affected dramatically the electrical performance of the solar cells. The Cu/Se rich perimeter influenced the electrical performance by increasing the recombination mechanism at the cell edge. The loss mechanism was assumed to be mainly by SRH recombination.

A selection of the fabricated micrometer-sized solar cells was investigated under concentrated light. Whether shaded or etched, the cells showed a maximum performance in the medium concentration range, specifically in the range of 20x to 50x and from 20x to 30x, respectively. Experimental results showed a 3.7 ± 1.9% and 2.1 ± 1.4% absolute and 25.3 ± 12.5% and 14.0 ± 9.7% relative increment of the efficiency for the best round-shaped micrometer-sized solar cell by shadowing (∅ 250 µm) or etching (∅ 200 µm) the absorber, respectively. Regarding the lamellar-shaped solar cells, the I-V parameters with concentration reached a maximum value in the range of 10x to 40x and from 20x to 40x for shaded and etched cells, respectively. 1.3 ± 0.4% and 1.8 ± 0.4% absolute and 10.9 ± 3.3% and 14.6 ± 3.1% relative increment of the efficiency for the best lamellar-shaped solar cell produced by shadowing or etching the absorber, respectively, was observed.

The opto-electronic properties of the micrometer-sized solar cells were affected by the different fabrication processes and characterization tools. Fabricated devices have shown a concentration limit (<100x) due to the temperature of the cell during the measurement and the current losses through the isolation layer. High concentration factors are feasible to apply to micrometer-solar cells if the heat management of the cell is enhanced and the series and shunt resistances are

constrained. Furthermore, high fluxes could be reached without diminishing the cell performance by implementing a suitable metal grid on the front contact to extract the photo-generated current, reducing the series resistance. Concentration factors above 100x are expected to be measured in such circumstances.

Chapter 6:

Opto-electronic simulations

6.1. Introduction

In the previous chapters, the fabrication of micrometer-sized solar cells displayed the benefits of cell size minimization under concentrated light, but also the loss mechanism induced during the fabrication process such as the increment of the series resistance due to the gap between the active area and the Ni/Al grids. Furthermore, by etching the absorber material a lack of selenium was found at the perimeter of the cell, where a high Shockley-Read-Hall recombination strongly affected the performance of the cell.

The model was implemented with the help of FEM software by combining a thermal module with an opto-electronic module to reproduce the behavior of the fabricated solar cells. Moreover, the model was intended to simulate the behavior of CIGSe solar cells, but could also be used for any kind of solar cell for concentration purposes. In this chapter, the validation of the model under standard test conditions at 20°C was investigated first and, secondly, under concentrated light. The different loss mechanism observed in the previous chapter, the expected temperature of the cell during the measurement time and other parameters obtained from the different characterization of the fabricated micrometer-sized solar cells, were taken into account in the thermal-opto-electronic model and shown in this chapter.

6.2. Thermal-opto-electronic simulations and results examination

A 3D thermal-opto-electronic (*TOE*) model was implemented using finite element method (*FEM*) software [35] to simulate the I-V characteristic curves of the solar cells. A meticulous reproduction of the fabricated micrometer-sized solar cells produced by etching the absorber was implemented in the model. The structure and dimensions of the cells were as detailed in Chapter §3.

6.2.1. I-V simulations under AM1.5G illumination

The implemented TOE model was validated by iterating parameters such as relative permittivity, electron affinity, effective density of states and others variables contained in Table 6.1 to fit the performance of the reference cells under standard test conditions at 20°C (*STC-20°C*) (Further details in Appendix III-2). In this work, the same opto-electronic properties were assumed for micrometer-sized and macroscopic solar cells.

Table 6.1:
Opto-electronic properties used for the modeling based on [100] [101] [102] by fitting the I-V reference characteristic curve.

Parameter	Units	CIGSe (p-type)	CdS (n-type)	i-ZnO (i-type)	AZO (n-type)
Band gap, E_g	eV	1.185	2.450	3.400	
Relative permittivity, ε	-	13.6	10.0	9.0	
Electron affinity, χ	eV	3.89	3.75	4.00	
Effective density of states, Valence band, N_v	$1/cm^3$	$15 \cdot 10^{+18}$	$15 \cdot 10^{+18}$	$9 \cdot 10^{+18}$	
Effective density of states, Conduction band, N_c	$1/cm^3$	$7 \cdot 10^{+18}$	$2 \cdot 10^{+18}$	$4 \cdot 10^{+18}$	
Donor doping concentration, N_D	$1/cm^3$	-	$1 \cdot 10^{+15}$	$1 \cdot 10^{+18}$	
Acceptor doping concentration, N_A	$1/cm^3$	$1 \cdot 10^{+16}$	-	-	
Electron mobility, μ_e	$cm^2/(V \cdot s)$	50	50	50	
Hole mobility, μ_h	$cm^2/(V \cdot s)$	20	20	20	
Electron lifetime, SRH	ns	10	30	10	
Hole lifetime, SRH	ns	10	0.033	0.010	
Optical index, n [47]	-	CIGSe_n	CdS_n	i-ZnO_n	AZO_n
Optical index, k [47]	-	CIGSe_k	CdS_k	i-ZnO_k	AZO_k

Note that the same opto-electronic properties were selected for the intrinsic ZnO and for the aluminum-doped zinc oxide ($ZnO:Al_2O_3$ 1.5wt.%) layers. In this work, to simplify the validation of the opto-electronic model, those properties were assumed to be identical. This assumption is widely used by the research community that provides acceptable and comparable results

between simulations and experimental results [100] [101] [102]. However, the author included and simulated both layers in case that in future works it is desired to modify these values without changing the structure of the TOE model.

Generally, during the co-evaporation process, the molybdenum back contact is subjected to high temperatures in a selenium atmosphere. Although, the Mo layer is affected by this process, a tiny $MoSe_2$ layer is generated. Pure Mo/CIGSe interfaces behave typically like a Schottky contact, but Mo/$MoSe_2$/CIGSe interfaces act as an ohmic contact [103] [104]. An ohmic contact will be selected for further simulations for the back contact, but the addition of a process dependent $MoSe_2$ layer was ignored in the model design.

The I-V characteristic curve of the simulated reference solar cell (*SimRef.SC*) differed slightly from the measured results, specifically, the short-circuit current density (J_{sc}) was reduced by 1.5% to 32.3 $\pm$ 0.1 mA/cm^2. The open-circuit voltage (V_{oc}) presented an increment of 0.9%, reaching 0.653 $\pm$ 0.048 V but the fill factor exhibited a reduction of 2.1%, dropping to 68.6 $\pm$ 2.3 %. The overall efficiency was found to be below the reference values in about 2.7%, reaching 14.5 $\pm$ 1.2 % of the power conversion to electricity. The values obtained for the SimRef.SC were in correlation with the experimental results presented in Chapter §5.

Round-shaped solar cells were investigated as a function of the cell size, specifically, solar cells produced by etching the absorber material. The aim of this Thesis is to save material and reduce costs to boost CPV capabilities in the PV market, consequently, the investigation focused on this cell group rather than on shaded cells. However, the fabrication of micrometer-sized solar cells via top-down approaches by using high quality material produces a large amount of waste that must be processed and recycled for later reuse to reduce cost and save material. Nevertheless, solar cells developed via bottom-up approaches by using in early stage low quality material should be able to be described by the current configuration for the TOE model, apart from its different opto-electronic properties.

Therefore, the loss mechanism discussed in Chapter §5 were taken into account in the TOE simulations for the case of etched cells. The photo-generated current was extracted directly from the front and back contacts of the solar cell. Therefore, the effect of the intrinsic

resistance of the resin was neglected in the model, i.e. the current losses through the photoresist layer were not simulated. For simulations purposes, homogeneous Shockley-Read-Hall recombination was applied to the bulk absorber only. However, EDX and PL characterizations revealed a lack of Se featured in a 5 to 10 µm wide ring at the edge of the etched absorber layer. A SRH recombination rate greater than in the CIGSe bulk material was settled to the cell perimeter. The lifetime value implemented along the perimeter was 10^{-1}x lower than the lifetime for the bulk absorber and the width of the ring at the CIGSe edge was selected to be 10 µm regardless of the solar cell diameter.

Figure 6.1a-f depict the basic parameters dependence with concentrated light, from 1 sun up to 150 suns. Under STC-20°C in particular, TOE simulations exhibited a reduction of the cell performance as the size of the cell decreased. The larger the diameter, the higher was the performance of the cell. Electrical parameters obtained from the I-V simulations presented a short-circuit current density below 30 mA/cm^2 for the variety of diameters (∅ 200 µm, ∅ 150 µm, ∅ 125 µm, ∅ 100 µm and ∅ 90 µm) of the solar cells included in the simulations (shown only for ∅ 200 µm in Figure 6.1a). The J_{sc} was reduced by minimizing the cell size due to the strong SRH recombination concentrated at the cell edge. The smaller the cell size, the greater was the weight of the perimeter recombination with respect to the generation rate of the cell. In the same manner, the open-circuit voltage dependence with cell minimization was observed to linearly decrease by minimizing the active area of the cell (Figure 6.1b). Furthermore, the measured V_{oc} exhibited drop with respect to the reference solar cells under STC-20°C in about 7%, the same percentage as the values provided by the simulations.

Regarding the fill factor under STC-20°C, the simulations exhibited a drop in about 7% with respect to the SimRef.SC (Figure 6.1d). This behavior was in correlation with that observed for round-shaped shaded solar cells but not for the etched ones. As discussed before in Chapter §5, section 5.3.3.3.1, no theory was found to explain the increment of the *FF* for the solar cells produced by etching the absorber. Even when this phenomenon was not understood, the simulated values were in correlation with the other measurements such as those obtained from RSS and lamellar-shaped solar cells. For comparison purposes, the reduction of the *FF* with respect to the experimental results was reflected in the same manner in the efficiency values

(Figure 6.1c). The simulated efficiency under STC-20°C was found to decrease as the diameter of the solar cells was reduced. This behavior was observed previously for round-shaped solar cells investigated in Chapter §5, section 5.3.3.3.2. The smaller the diameter of the solar cell, the lower the maximum efficiency reached under STC-20°C. As discussed in Chapter §5, section 5.3.3.3.2, with the current fabrication techniques, large cells (in the range of ∅ 200 µm solar cells) were desirable for concentration purposes due to the reduction of the cell performance with cell minimization and the comparable values respect to the reference values. By fitting the dependence of the efficiency with the cell size, no solar cells with a diameter less than 40 µm were expected to present an electrical response. This estimation was in agreement with the observed values for RSE cells, where the diameter threshold was found in the range of 50 µm.

Hence, the experimental and simulated results under standard test conditions at 20°C presented a comparable behavior with the selected boundary conditions in the TOE model, where the temperature increment with illumination (*AM1.5G*) was considered, as well as the loss mechanism provoked by etching the absorber material, and the absorption of each layer with the use of a suitable optical database of the fabricated layers.

6.2.2. I-V simulations under concentrated AM1.5G illumination

The I-V characteristic curves were simulated under concentrated light. As referred in section 2.5, the spectrum of the beam was considered not to alter with concentrated illumination as the generation rate, which increased linearly as the concentration factor augmented. One of the most important parameters taken into account in the TOE simulations was the inclusion of the expected temperature dependence of the solar cells under concentrated light during the measurements, apart from the loss mechanism. The temperature evolution with concentrated light was previously presented in Chapter §3, section 3.3.4, and how the characterization equipment influenced such parameter in Chapter §5, section 5.2.3.3. Therefore, as a result of illuminating the active area and the surrounding material, the temperature evolution described a quick increment within the measurement time. Additionally, the expected temperature of the solar cell was simulated and included in the TOE model when the sole cell was illuminated with concentrated light (Chapter §3, section 3.3.4). The temperature of the cell can be reduced by

laminating the device with a cover glass, which will spread the temperature along this material as described in Chapter §3, section 3.3.2. Therefore, a reduction of the temperature will benefit the overall performance of the micrometer-sized solar cells by augmenting the concentration capabilities with respect to indoor measurements.

Figure 6.1a-f show the simulations results performed with concentrated light. Three cases are depicted: when the active area is solely illuminated keeping the temperature of the cell at 20°C ("*RT(20°C)"*), and at the expected temperature ("*Only cell"*), and when the active area and surrounding material are illuminated with the corresponding temperature (*"All over"*). For comparison purposes, for a cell diameter of 200 µm only, the three cases are shown in Figure 6.1a-f. For other diameters, the simulated results behave in the same manner as those depicted for a ∅ 200 µm solar cell but proportionally shifted with respect to the values under STC-20°C.

I-V simulations presented a comparable tendency with respect to the experimental results (Figure 6.1a-f with respect to those reported in Chapter §5, section 5.3.3.3.2). As remarked in the prior section, TOE simulations exhibited a reduction of the performance of the cell with size minimization. In this case, with concentrated AM1.5G light, the dependence of the basic parameters on the cell size maintains the same proportion. This trend was expected based on the pre-determined boundary conditions, where the recombination mechanism remained invariable with concentrated light and the temperature gap between the different concentration factors remained below 25°C for concentrations up to 120x at the end of the measurement time (Chapter §3, section 3.3.4).

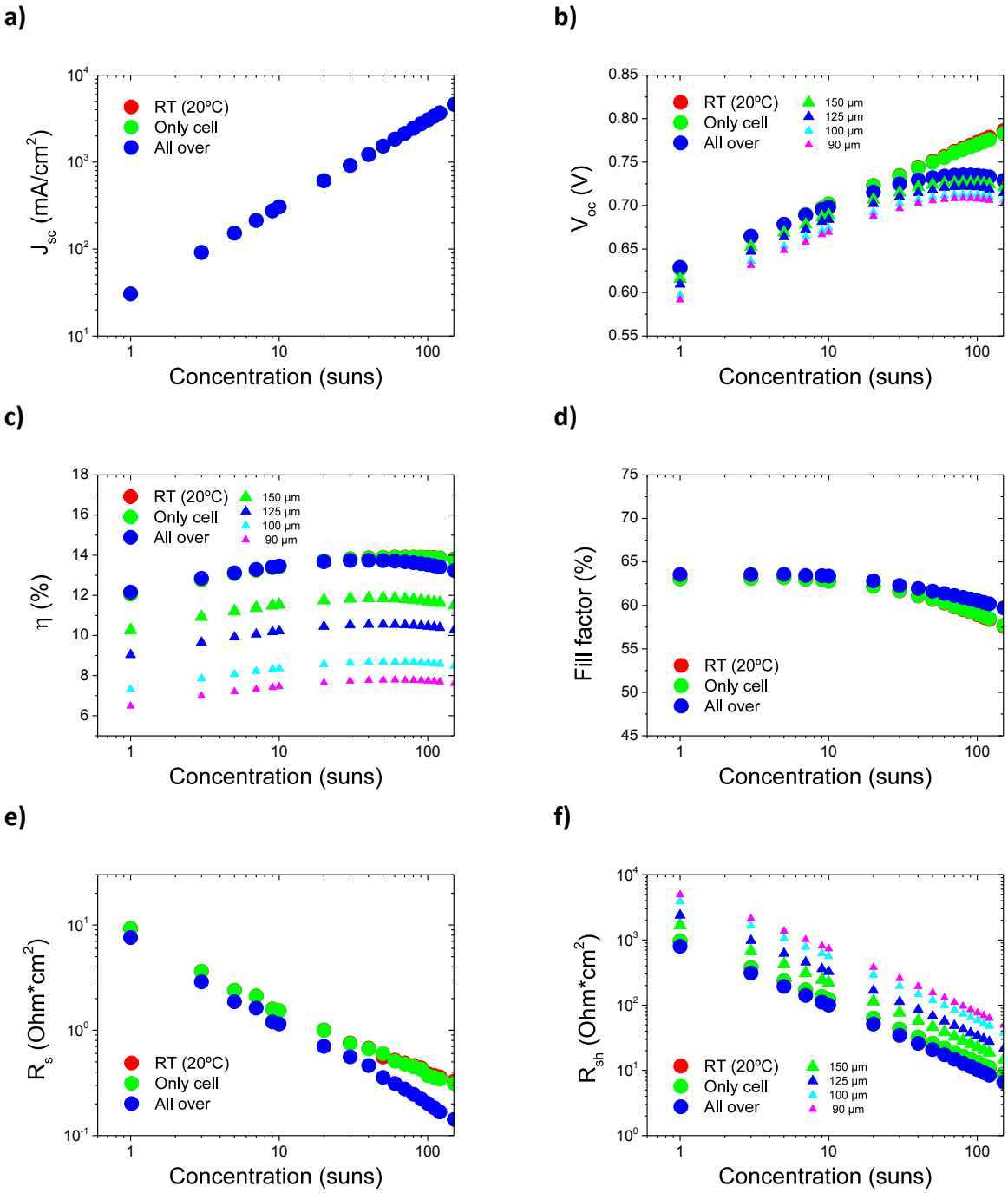

Figure 6.1: Basic parameters extracted from the simulated I-V characteristic curves of the simulated micrometer-sized CIGSe solar cells under concentrated light, **a)** J_{sc} (all cases overlapped), **b)** V_{oc}, **c)** η, **d)** *FF*, **e)** R_s and **f)** R_{sh} (*"RT (20°C)"* case overlapped by the *"Only cell"* case) dependence with concentrated light. Simulations for the device structure as in (Chapter §3, section 3.2). *"RT(20°C"*, *"Only cell"* and *"All over"* correspond to the simulations of a solar cell with a diameter of 200 µm. V_{oc}, η and R_{sh} figures include the simulations for a ∅ 150 µm, ∅ 125 µm, ∅ 100 µm and ∅ 90 µm solar cell for the *"All over"* case.

In Figure 6.1a, the results of the simulations under concentrated light presented a linear increase of the short-circuit current density, which was found to be invariable with the pre-set temperatures of the solar cell. Respect to the open-circuit voltage results; Figure 6.1b shown

the evolution of this parameter with concentrated light, where a maximum is reached in the range of 60x to 100x for the selected solar cells. The behavior of the V_{oc} with concentration depicts a similar performance for the solar cells investigated. A remarkable difference between the V_{oc} values obtained experimentally and through simulations, was the range where the maximum V_{oc} was found. In this case, the experimental results exhibited a maximum in the range of 20x to 40x for round-shaped etched solar cells. The V_{oc} could be slightly shifted to higher values with respect to the experimental results due to underestimated temperature settings. The cell temperature could be higher during the measurement time with respect to the temperatures obtained from the thermal simulations. However, an *in situ* measurement of the temperature dependence with time for the cell was not accomplished to cross-check with thermal simulations presented in Chapter §3 due the complexity of the measurement and the available resources.

Previous argumentation referred to the dependence of the V_{oc} when the solar cell and the surrounding material were fully illuminated (*"All over"*). For the other cases, the open-circuit voltage increases without being penalized by the temperature increment in the cell (*"Only cell"*) and for the ideal case when the temperature of the cell is kept at 20°C (*"RT(20°C)"*). The *"Only cell"* case begins to diverge slightly with respect to the *"RT(20°C)"* case above 100x due to the increasing temperature of the cell. However, the maximum V_{oc} obtained from the simulations was found in the range of 1000x as reported previously by Paire *et al.* [78].

At low concentration factors (<10x), the fill factor (Figure 6.1d) remained invariable with respect to the values under STC-20°C, however, above 10 suns, this value is reduced, as it is affected by the series and shunt resistance evolution with concentrated light. The *FF* obtained by simulating the pn-junction was lower than those measured experimentally. Nevertheless, this increment of the *FF* with respect to the reference values was not understood, and for comparison purposes, the *FF* was compared with that obtained for RSE solar cells. In this case, the *FF* was a slightly higher but quantitatively comparable. Although the *FF* for the RSE cells exhibited an increment with respect to the values found under STC-20°C, reaching a maximum in the range of 10x to 40x to decrease after this range, the simulated value dropped when above 10 suns. Either *"All*

over" or the other cases, the *FF* decreased with the concentration, being slower for the first case.

The evolution of the *FF* influenced drastically the overall performance of the cell, diminishing the power conversion to energy in the same manner (Figure 6.1c). The remarkable increment of 12.4% of the *FF* measured for RSE cells affected the final efficiency of the micrometer-sized solar cells, augmenting its value. In this case, the efficiencies obtained with TOE simulations presented a lower value due to the homogenization of the *FF* with respect to the reference values. The maximum efficiency achieved, reproducing the experimental setup (*"All over"* case), was in the range of 30x to 50x in correlation with the experimental results. The TOE simulations showed a 1.6% absolute and 13.0% relative increment of the efficiency under concentrated light for the best round-shaped micrometer-sized solar cell for the *"All over"* case. Experimental results, with the same configuration, depicted an absolute and relative increment of the efficiency of 2.1% and 10.9%, respectively. Apart from the unexpected and inexplicable increment of the *FF* for RSE solar cells, the TOE model reproduced the behavior of the different micrometer-sized CIGSe solar cells. However, to improve such simulations, *in situ* temperature measurements of real devices need to be investigated as well as other loss mechanisms not taken into account in this Thesis. Medium concentration factors could be applied to micrometer-sized solar cells without diminishing the cell performance as shown in Figure 6.1c for the *"RT 20°C"* and *"Only cell"* cases, where the efficiency of the solar cell reaches a maximum in the range of 50x to 100x. Both cases, *"RT 20°C"* and *"Only cell"*, presented an absolute and relative increment of the efficiency under concentrated light of 1.8% and 11.5%, respectively, for the best round-shaped micrometer-sized solar cell (∅ 200 µm) compared to the values under STC-20°C.

TOE simulations of I-V characteristic curves depicted a reduction of the series (Figure 6.1e) and shunt (Figure 6.1f) resistance with concentration, specifically, with a dependence similar to *Paire's* model [45]. R_{sh} obtained by simulating the pn-junction presented a good correlation with the experimental results. However, the difference between measurements and simulations for R_s exhibited a deviation factor of 10. Therefore, the experimental value of the series resistance was affected by the increment of the *FF*, which induced a reduction of R_s in the same manner.

The series resistance found for the different cases followed the *Paire's* model [45]. Nevertheless, for concentrations over 40x, a different trend was observed for the *"RT(20°C)"* and *"Only cell"* cases, where the dependence with concentrated light slightly changed with respect to the linear trend of the *"All over"* case. For R_{sh}, the dependence of these values with concentration for the different cases remained invariable, but as the diameter of the solar cell decreases, R_{sh} increased. In comparison with the experimental results, where no clear trend was found for the shunt resistance with concentration and with diameter, the Author assumed that in the case of having a larger amount of data from more measurements, the dependence of R_{sh} will follow the depicted in Figure 6.1f.

6.2.3. I-V simulations under inhomogeneous AM1.5G illumination

The effect of different illumination profiles in the performance of the solar cell was investigated. However, and due to the limitations of the FEM software in the semiconductor module, the results obtained above 1000 suns for an incident beam with a Gaussian like light distribution and for a Tower like irradiation profile have not been taken into account to be discussed in this work. Concentrations factors above 1000x provided inconclusive results, which depended strongly on the meshing of the stack of layers in the TOE model. Nonetheless, the results obtained for concentrations below this value are introduced hereunder.

As discussed in Chapter §3, section 3.3.3, CPV devices for high concentration requires a complex optical systems, which often do not produce a uniform distribution of the beam and requires high accuracy to concentrated light on the solar cell. The TOE model was examined for different light distributions for investigating the possibilities of enlarging the active area meanwhile the beam is concentrated in a smaller surface. Hence, the following study encompasses misalignment and angular tolerance of illumination, i.e. simplifying tracking systems for high concentration purposes, by investigating the effect of concentrating light inside the active area. The solar cell was kept at standard temperature, 20°C (*RT(20°C)*).

As a result of applying a Gaussian like beam distribution on the surface of the active area, considering the same that the solar cell receivers the same amount of energy regardless of the shape, the V_{oc} obtained for a micrometer-sized solar cell with a diameter of 100 µm remained

constant for *FWHM* values above $1 \cdot 10^{-4}$ m (Figure 3.7-V_{oc}). Below this point, the open-circuit voltage slightly decreased with localized light. However, for the Tower like distribution, the evolution of the V_{oc} with localized light remained nearly constant for concentrations up to 1000 suns.

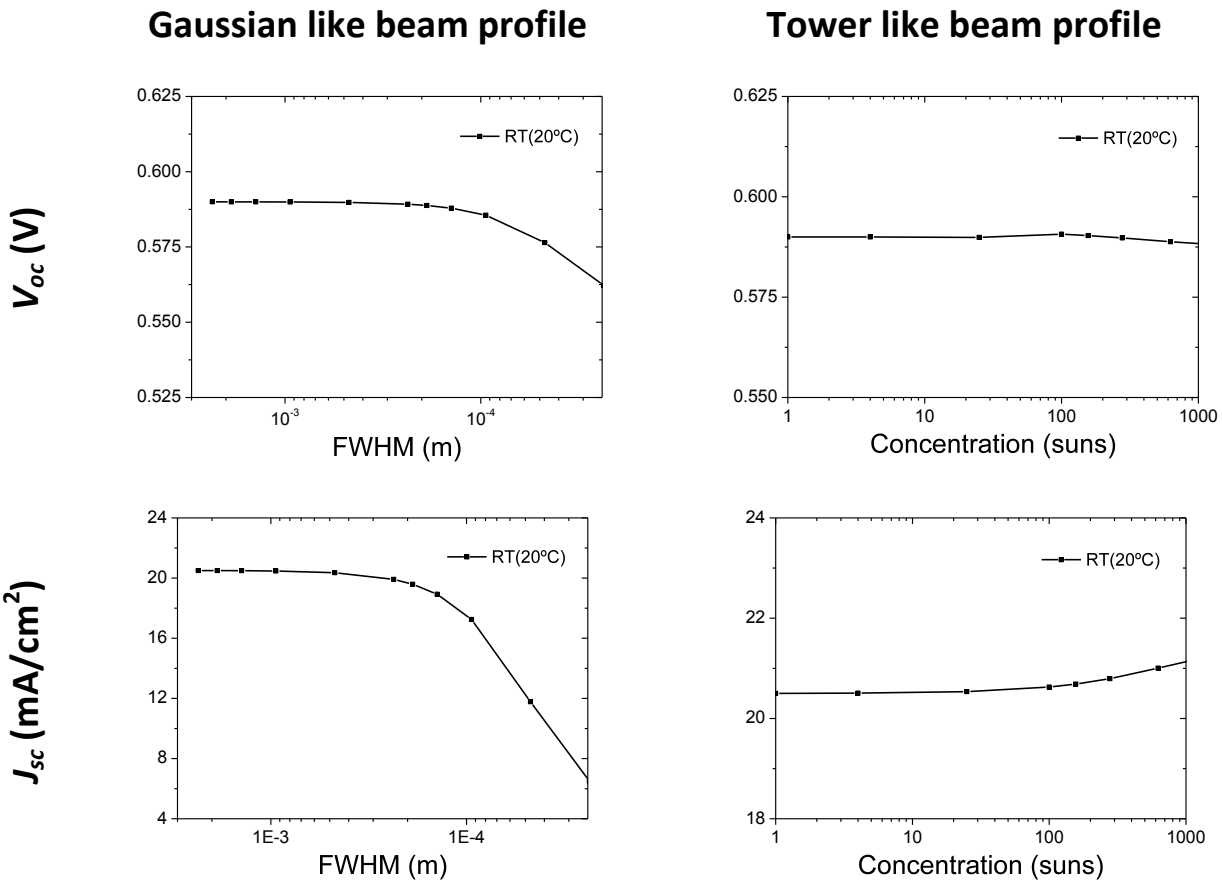

Figure 6.2: Open-circuit voltage and short-circuit current density of the simulated micrometer-sized CIGSe solar cell (∅ 100 µm) under concentrated light with a Gaussian like beam profile and a Tower like beam profile along the solar cell surface as a function of the full width at half maximum (FWHM) and the Tower size (see 2.7), respectively.

An opposed trend was observed for the short-circuit current density, where J_{sc} decreased dramatically for *FWHM* values below $1 \cdot 10^{-4}$ m and increased for concentration factors above 100 suns for Gaussian and Tower like beam distributions, respectively (Figure 3.7-J_{sc}). One possible explanation of the fast decrease of J_{sc} with localized light could be the effect of the normalization of the energy provided by the Gaussian beam. Due to the limitations of the equipment used, a dense mesh in the semiconductor material could not be applied, due to the limited RAM memory [67] and the large structure used in the TOE model. Therefore, the integration of the photo-generated energy along the solar cell for narrow beam profiles was

underestimated as the FWHM decreased. However, for Tower like distributions, the integration of the photo-generated energy was found to not underperform the overall characteristics of the cell. Another explanation for this effect could be the impact of different regions where different I-V characteristics of the cell are present. Active areas without illumination, called dark areas, behave as ohmic paths with the exception of the voltage induced at the semiconductor terminals, which provoke a current flow through the diode. The higher the voltage, the greater the electric current lost through the diode. For the Gaussian beam distribution, the different regions behave as point sources which are connected through the transparent conductive oxide. Moreover, to complain with Kirchhoff's current law, the performance of the regions with higher concentration need to be reduced, and therefore, the short-circuit current density, open-circuit voltage and the efficiency of the solar cell. On the other hand, Tower like beam distributions were less affected by this phenomenon due to the ohmic like behavior of the dark areas with respect to the illuminated zones.

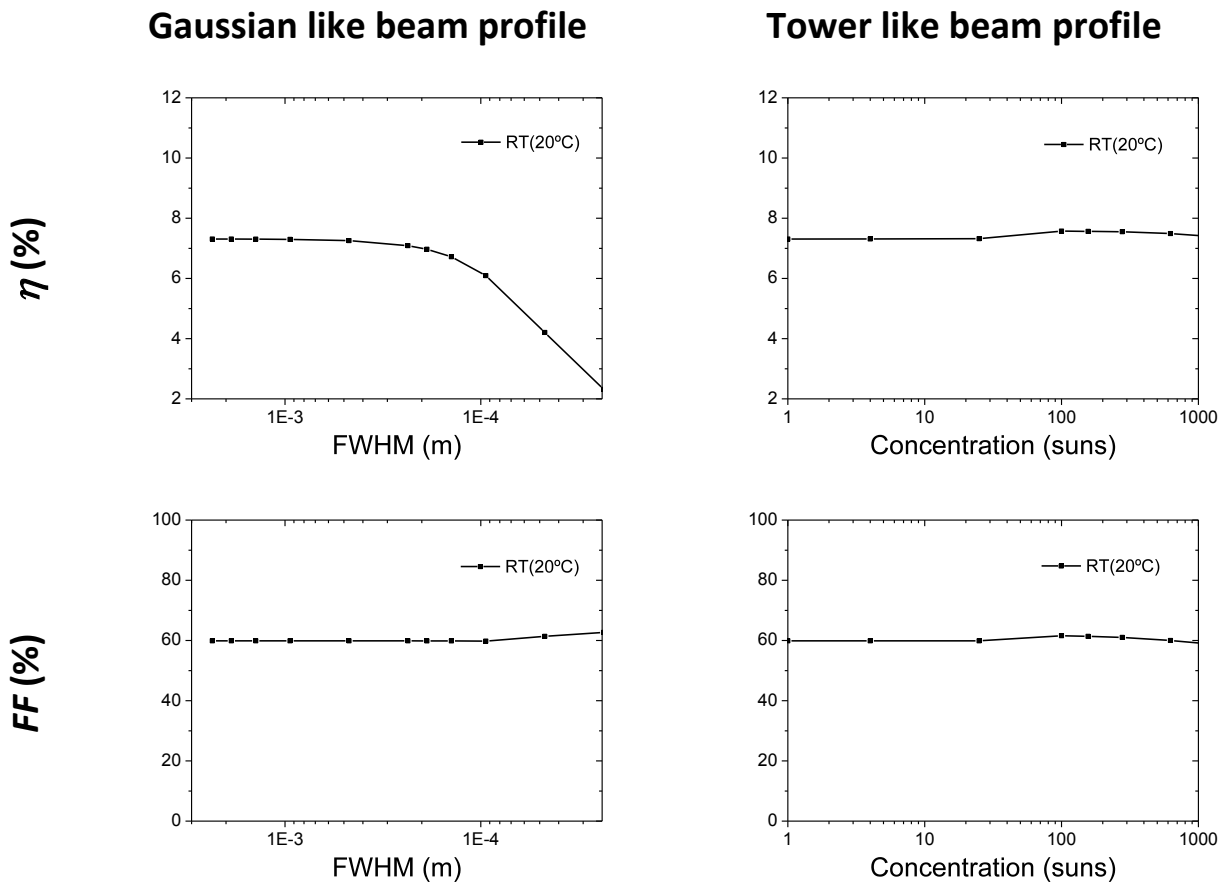

Figure 6.3: Efficiency and fill factor of the simulated micrometer-sized CIGSe solar cell (∅ 100 µm) under concentrated light with a Gaussian like beam profile and a Tower like beam profile along the solar cell surface as a function of the full width at half maximum (*FWHM*) and the Tower size (see 3.7), respectively.

Thereby, the fill factor and the power conversion to electricity shown in Figure 6.3 presented the same behavior as the open-circuit voltage and the short-circuit current density. Even when the *FF* remained constant with localized light (Figure 6.3-FF), the efficiency decreased for *FWHM* below $1 \cdot 10^{-4}$ m (Figure 6.3-η). However, for a Tower like beam distribution, the efficiency of the cell remained constant and increased slightly for concentrations above 100x.

Flat irradiation profiles, Tower like beam distributions, are preferred for concentration purposes as the TOE simulations depicted. Although, for some *FWHM* values, Gaussian like beam distributions could be used avoiding the implementation of complex optical systems for concentrating light. However, these results were carried out maintaining the temperature of the solar cell at 20°C which implies that these values correspond to the best possible case, where the temperature of the cell remains constant with localized light. Narrow beam profiles produce highly localized heat onto the cell which could lead to a hot point and produce a shunted cell if the temperature value is above 150°C. Moreover, using narrow Gaussian or Tower like beams could help to simplify module fabrication, device assembly and system operation requirements. Hence, higher design tolerances are provided using narrow illumination profiles helping to mitigate the effect of lens misalignment and facilitating the operation of the tracking systems.

6.3. Conclusions

In this chapter, micrometer-sized $Cu(In_x,Ga_{1-x})Se_2$ solar cells were modelled with FEM software composed of different modules: optical, thermal and electrical. The thermal-opto-electronic model was implemented to represent the CIGSe solar cells produced in HZB. Moreover, the modification of the TOE model to consider other kind of solar cells can be easily performed by finding the suitable opto-electronic parameters, which reproduce the behavior under STC-20°C.

The TOE model simulations for the I-V characteristic curves exhibited a good correlation under STC-20°C and under concentrated light with respect to the results obtained experimentally. Furthermore, the simulation performed to obtain the I-V characteristic curves under

concentrated light and as a function of the diameter of the cell, presented a similar behavior as the experimental results. However, the temperature of the cell during the measurement time was found to be an important factor in the model, which was only estimated and not as a result of an *in situ* measurement. Undesired heat can be diminished by the inclusion of a cover glass in the device structure, which will affect considerably the final temperature of the cell and, hence, the maximum efficiency reached under concentrated light. Additionally, even with the estimated recombination mechanism along the cell edge and the estimated width of this region, with a higher SRH recombination than in the bulk material, the performed simulations correlated with the experimental measurements.

Here, the benefits of cell size minimization were impaired by the inclusion of the SRH recombination at the cell edge based on the effects of the etching process in the final performance of the solar cell. Solar cells with a diameter in the range of 200 μm were preferred for concentration applications with the current fabrication process. Furthermore, the electronic performance of those cells was similar to that exhibited by the reference cells with the advantage of saving material and proving a similar power conversion to electricity. By reducing the cell size, the performance of the cell decreased progressively to completely disappear for cell diameters below 40 μm. Therefore, a commitment between the reduction of the cell size, i.e material saving, and the gain under concentrated light was needed. With the current fabrication process and the available resources, the best candidate to fulfill these requirements is a solar cell with a diameter in the range of 200 μm capable of saving material by a factor of 40x without diminishing the total amount of energy delivered by the micrometer-sized solar cell with respect to a planar reference cell.

The thermal simulations demonstrate the good disposition to enhance heat dissipation in micrometer-sized solar cells and the combined models, thermal-opto-electronic model, exhibited that medium to high concentration factors are feasible for application to micrometer-sized solar cells. However, TOE simulations depicted a limitation of the cell performance with concentrated light, which strongly depended on the recombination mechanism, the cell temperature and the intrinsic resistances. By reducing these parameters, concentration factors above 100x could be applied to micrometer-sized solar cells without diminishing the overall

performance. Therefore, a great material saving, >100, could be achieved by utilizing the benefits of cell size miniaturization.

TOE simulations with Gaussian and Tower like beam distributions shown the possibilities of localizing light inside of the active area to simplify the module fabrication, the device assembly and other requirements for high concentration purposes. Therefore, Tower like beam distributions could mitigate the effect of lens misalignment and facilitating the operation of the tracking systems without diminishing the overall performance of the micrometer-sized solar cell.

Chapter 7:

Conclusions and future work

7.1. Conclusions

The most important findings of this Thesis can be summarized as follows:

- Thermal studies have shown the individual effect of the set of general design parameters on the heat management of micrometer-sized CIGSe solar cells under concentrated light, providing novel and detailed results which corroborated the benefits of reducing cell size and increasing concentration factor.

- Micrometer-sized $Cu(In_x,Ga_{1-x})Se_2$ solar cells, via "*top-down approach*", were fabricated and characterized by different techniques, finding that the fabrication methods affected dramatically the cell performance as the active area was reduced.

- A 3D FEM model, comprised of thermal and opto-electronic modules, was successfully employed to simulate, and therefore, predict the output parameters of micrometer-sized CIGSe solar cells under all considered concentration factors and beam profiles.

- The assessing and verification of the TOE model, based on the fabrication and characterization methods, forecasted the application of higher concentration factors to micrometer-sized CIGSe solar cells without lessening the overall performance.

7.2. General conclusions

The conclusions extracted from the results obtained along this work are presented in this section, which are directly related to the main objectives sought in this Thesis. In a general view, this Thesis proves that micrometer-sized CIGSe solar cells have potential for low cost, high efficiency and improved heat dissipation under concentrated light. Furthermore, other material-based solar cells may benefit from cell miniaturization. However, based on the author´s fabrication processes and characterization methods, experimental measurements and TOE simulations showed a limitation of the cell performance with concentrated light with a maximum efficiency below 100 suns. Nevertheless, such limitations are related to the fabrication approach, other techniques could avoid these effects and boost the power conversion to electricity with concentrated light.

Thermal simulations

A detailed study of the heat management of micrometer-sized CIGSe solar cells was carried out. These results corroborate the benefits of reducing cell size augmenting the concentration factor due to the improved heat dissipation of miniaturized solar cells.

Two thermal models, basic and realistic case, were investigated. The first represented the solar cell for indoor measurements and the realistic case for outdoor applications. Nevertheless, the realistic case was intended to illustrate the temperature of the solar cell under concentrated light for a non-active cooling device, which demonstrated the possibility of reducing CPV requirements and cost by lessening or withdrawing the active cooling systems.

According to the results obtained, key parameters of the structure of the CPV device were identified such as thermal conductivity, area or thickness of the back contact material. These parameters present an important role to increase the effect of the heat dissipation of the solar cell under concentrated light. One of the most remarkable findings was the effect of the back contact metal on the heat management of the solar cell, larger areas provided greater heat dissipation. High concentration factors, up to 10^5x, were feasibly applied on micrometer-sized CIGSe solar cells, where the cell remained in a dependable temperature range below 150°C.

Thermal results depicted the application of high irradiation values for PV cells width above 20 µm for a 3 mm wide substrate and above 3.2 µm width for 0.5 mm wide a substrate, i.e. a minimum substrate-cell width ratio of 150.

Different illumination profiles were investigated. For flat irradiation profiles, high concentration factors, up to 10^5x, were applied on micrometer-sized CIGSe solar cells without being the temperature above the pn breakdown range. Gaussian and Tower like beam profiles were also analyzed. Narrow beam profiles produced highly localized heat onto the cell which produces a highly located temperature increment. The temperature of the solar cell remains below 100°C for *FWHM* values (< 0.1 µm) and *TW* values (< 0.1 µm) boosting the cell tolerance against the effect of lens misalignment or the issues of the tracking systems. Although homogeneous beam profiles are desirable, CPV operational requirements could be reduced by applying different irradiation profiles.

Experimental results

Micrometer-sized $Cu(In_x,Ga_{1-x})Se_2$ solar cells were fabricated for concentration purposes via the so-called "*top-down approach*" by different techniques. The combination of lithography and chemical etching processes was found the most suitable for solar cell miniaturization. Two types of solar cells, round- and lamellar-shaped, were developed. Furthermore, these cells were either shaded or etched providing trends clearly appreciable. Larger diameters or widths were found for shaded solar cells in comparison with etched samples. This effect influenced the minimum achievable size of the fabricated cells, a minimum diameter of 30 µm for shaded cells and 50 µm for etched absorbers was achieved.

For round-shaped solar cells produced by etching, a lack of selenium along the absorber perimeter was observed. EDX and PL characterizations revealed the effects of Piranha-based etching featured in a 5 to 10 µm wide ring at the edge of the etched CIGSe layer. The shortage of selenium, affected the electrical performance of the solar cell noticed in the I-V characteristic curves under STC-20°C and concentrated light. The loss mechanism was assumed to be mainly by SRH recombination.

A selection of the fabricated micrometer-sized solar cells was investigated under concentrated light, which showed a maximum efficiency in the range of 20x to 50x and from 20x to 30x for shaded and etched cells, respectively. The best round-shaped micrometer-sized solar cell by shadowing (∅ 250 µm) or etching (∅ 200 µm) the absorber showed a 3.7 ± 1.9% and 2.1 ± 1.4% absolute and 25.3 ± 12.5% and 14.0 ± 9.7% relative increment of the efficiency compared to the values under STC-20°C, respectively.

Regarding the lamellar-shaped solar cells, with a maximum efficiency value in the range of 10x to 40x and from 20x to 40x for shaded and etched cells, respectively, showed a 1.3 ± 0.4% and 1.8 ± 0.4% absolute and 10.9 ± 3.3% and 14.6 ± 3.1% relative increment of the efficiency compared to the values under STC-20°C, respectively.

Despite the location of the maximum efficiency value, fabricated devices have shown a concentration limit (<100x), where the electrical performance of the cell was below the obtained under STC-20°C. The temperature of the cell during the measurement and the current losses through the isolation layer were the main responsible of this concentration limitation. Nonetheless, with the current fabrication settings, CPV cost could be reduced by reducing the active area by a factor of 100 without lessening the electrical performance in comparison with the values under STC-20°C.

Thermal-opto-electronic simulations

A 3D model of micrometer-sized solar cells, in which thermal, optical and electrical (*TOE*) modules were implemented, was used to simulate the behavior of these cells under concentrated light. The suitable opto-electronic parameters were obtained, which reproduced the behavior of such cells under STC-20°C and which were applied to the solar cells under different circumstances.

The TOE simulations focused on the determination of the I-V characteristic curves. These exhibited a good correlation under STC-20°C and under concentrated light with respect to the results obtained experimentally after including the different loss mechanism and characterization methodology. The assumptions taken into account for the modelling were

turned out to be appropriate. Furthermore, the benefits of cell size minimization were impaired by the inclusion of the SRH recombination at the cell edge as it was also observed experimentally.

Three cases were simulated: "*RT(20°C)"*, "*Only cell"* and *"All over"*. The maximum efficiency when the active area and surrounding material were illuminated showed a maximum in the range of 30x to 50x with a 1.6% absolute and 13.0% relative increment of this parameter under concentrated light for the best round-shaped micrometer-sized solar cell (∅ 200 µm) compared to the values under STC-20°C. However, in case of performing a proper illumination by measuring, the efficiency value reached a maximum in the range of 50x to 100x for the case when the active area is solely illuminated keeping the temperature of the cell at 20°C and at the expected temperature. Both cases presented an absolute and relative increment of the efficiency under concentrated light of 1.8% and 11.5%, respectively, for the best round-shaped micrometer-sized solar cell (∅ 200 µm) compared to the values under STC-20°C.

Different illumination profiles were also investigated. These beam distributions could mitigate the CPV requirements such as misalignments, tracking operation or assembly by localizing the spot inside of the active area of the solar cell.

Larger cells, in the range of 200 µm diameter, were preferred for concentration applications as the simulations depicted based on effects of the current fabrication process on the opto-electronic properties of the solar cell. Furthermore, these cells provided similar power conversion to electricity to that exhibited by the reference cells as the simulations and experiments shown. Moreover, solar cells with a diameter in the range of 200 µm demonstrated its capability to save material under concentrated light by enabling the cost reduction of CPV technology and its requirements.

Therefore, CPV requirement can be lessen by adopting the miniaturization of solar cells instead of the current technology used in this field. Cost reduction due to a great material saving (>100) and no need of active cooling can be achieved by utilizing the benefits of cell size miniaturization as was described in this work.

7.3. Future work

The fabrication process of micrometer-sized solar cells affected dramatically the opto-electronic properties of etched cells. By reducing the effect of the etching at the edge of the solar cell, the I-V characteristic curves are expected to improve due to the reduction of SRH recombination. On the same manner, by implementing a proper metal grid on the front contact to extract the photo-generated current, the series resistance is expected to reduce and the *FF* and efficiency to increase. Furthermore, if a cover glass is attached on top of the device, as it was shown in Chapter §3, the temperature of the solar cell will be lower due to an enhanced heat management of the cell. The open-circuit voltage, the fill factor and the efficiency are expected to increase. Therefore, additional improvements could show a higher concentrations factor and higher electrical performance.

The temperature of the cell has shown to be an important and crucial factor experimentally and in the simulations. However, it was only estimated and not as a result of an *in situ* measurement. A detailed and accurate determination of the temperature under concentrated light and during the measurement could ratify the assumptions and simulations used in this work. Furthermore, to improve TOE simulations, other loss mechanisms not taken into account in this Thesis need to be investigated.

Furthermore, the experimental and simulation results contained in this work are easily extrapolated to other material-based solar cells, which could also benefit from the advantages of solar cell minimization.

Appendix I

I.1. IOP publishing license

Hereunder, the accreditation IOP to publish the content of the paper *"Thermal management approaches of Cu(In_x,Ga_{1-x})Se_2 micro-solar cells"* published in the Journal of Physics D: Applied Physics (*50 (2017) 445501, doi:/10.1088/1361-6463/aa8ac5*) by Diego Sancho-Martinez *et al.*

IOP Publishing LICENSE

TERMS AND CONDITIONS

May 07, 2019

This is a License Agreement between FREIE UNIVERSITÄT BERLIN -- DIEGO SANCHO ("You") and IOP Publishing ("IOP Publishing") provided by Copyright Clearance Center ("CCC"). The license consists of your order details, the terms and conditions provided by IOP Publishing, and the payment terms and conditions.

All payments must be made in full to CCC. For payment instructions, please see information listed at the bottom of this form.

License Number	4583640082052
License date	May 07, 2019
Licensed content publisher	IOP Publishing
Licensed content title	Journal of Physics D : Applied Physics
Licensed content date	Jan 1, 1970
Permission type	Republish or display content
Type of Use	Thesis/Dissertation
Requestor type	Author of requested content
Format	Print, Electronic

Portion	chart/graph/table/figure
Number of charts/graphs/tables/figures	7
The requesting person/organization is:	Diego Sancho-Martinez
Title or numeric reference of the portion(s)	I would like to include in my Thesis the following figures (from 1 to 6) and the table 1 in Chapter 3 as Figure 3.1, 3.3, 3.4, 3.5, 3.6, 3.7, 3.8 and 3.9, and Table 3.1 and publish it online in the Freie University Repositorium Service
Title of the article or chapter the portion is from	Chapter 3: Thermal simulations
Editor of portion(s)	N/A
Author of portion(s)	N/A
Volume of serial or monograph.	N/A
Page range of the portion	39-59
Publication date of portion	Expected 01/06/2019
Rights for	Main product
Duration of use	Life of current edition
Creation of copies for the disabled	no
With minor editing privileges	no
For distribution to	Worldwide
In the following language(s)	Original language of publication
With incidental promotional use	no
The lifetime unit quantity of new product	Up to 499
Title	Chalcopyrite-based micro-concentrator solar cells: realistic device modelling and fabrications
Instructor name	Prof. Martina Schmid
Institution name	Freie Universität Berlin
Expected presentation date	Jun 2019
Billing Type	Invoice
Billing Address	FREIE UNIVERSITÄT BERLIN Berlin, Germany Attn: DIEGO SANCHO
Total (may include CCC user fee)	0.00 USD

Appendix II

II.1. Absorber (*CIGSe*) fabrication process

Two different processes, sequential and co-evaporation, were used to fabricate $Cu(In_x,Ga_{1-x})Se_2$ (CIGSe) absorbers.

II.1.1. Sequential fabrication process

A sequential process was firstly employed for the absorber formation. Evaporation of elemental elements in a vacuum chamber and a posterior selenization in a rapid thermal process (RTP) oven composed the two-step sequential process. Copper was deposited by electron beam (*e-beam*) physical vapor deposition (*PVD*). Indium and gallium were evaporated using an evaporation PVD system. E-beam and evaporation processes were performed in Creamet 450 equipment from the CreaVac company.

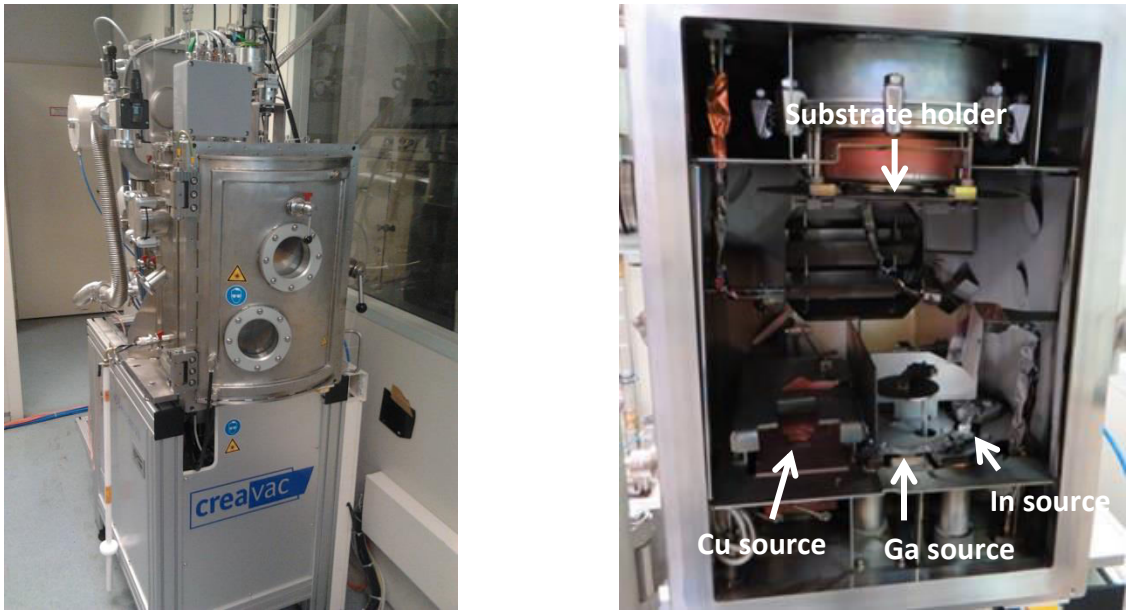

Figure App.II-1: Creamet 450 e-beam and evaporation equipment from the CreaVac company used for Cu, In and Ga deposition in HZB-NanooptiX group.

Variations of the stack of the precursor layers were performed (Figure App.II-2) to enhance the current efficiencies of the solar cells produced at the HZB-NanooptiX group [105]. The use of different stoichiometries and layer stacks was investigated [5]. CIGSe compositional characteristics were previously reported as the CGI and GGI atomic ratio. CGI and GGI ratios between 0.7 to 1.0 and 0.25 to 0.5, respectively, are desirable for the CIGSe formation [6].

$$CGI = \frac{Cu}{(Ga+In)} \qquad \text{(Eq.App.II-1)} \qquad GGI = \frac{Ga}{(Ga+In)} \qquad \text{(Eq.App.II-2)}$$

The In (*Alfa Aesar, 99.99% purity*) evaporation was performed by applying 1.2 ± 0.1 V and 105 ± 3 A to a crucible under a vacuum pressure of 10^{-5} mbar. With a deposition rate of 5 Å/s, the thickness of the evaporated layer was 290 ± 5 nm thick. The settings for the Ga (*Alfa Aesar, 99.99% purity*) and Cu (*Alfa Aesar, 99.95% purity*) deposition were 1.0 ± 0.1 V and 205 ± 5 A and 10 KV and 110 ± 2 mA, respectively, under a vacuum pressure of 10^{-5} mbar.

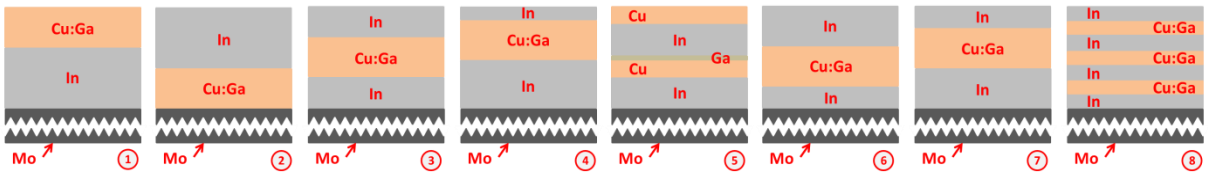

Figure App.II-2: Precursor structures tried at the sequential fabrication process.

The total thickness for each element was selected to achieve a CGI atomic ratio of 1 and a GGI atomic ratio of 0.3 after the selenization process. Specifically, a 290 ± 10 nm thick indium layer, a 230 ± 10 nm thick copper sheet and a 110 ± 10 nm thick gallium thin-film were deposited.

Table App.II-1:
XRF measurements of the selenized precursors from Figure App.II-2.

	$Cu(In_{0.7}Ga_{0.3})Se_2$	1	2	3	4	5	6	7	8
CGI	1.00	1.05	0.88	0.91	0.96	1.14	0.87	0.98	1.09
Cu/Se	0.50	0.45	0.38	0.39	0.41	0.50	0.41	0.45	0.47
GGI	0.30	0.45	0.41	0.41	0.47	0.43	0.40	0.46	0.43
Se/GI	2.00	2.32	2.35	2.42	2.21	2.33	2.14	2.19	2.30

To produce CIGSe absorbers, the precursors need to be selenizated. The samples were selenizated in a rapid thermal process (*RTP*) oven designed by the HZB-NanooptiX group (Figure App.II-3a-c). The precursors were introduced into a graphite box with a certain amount, 45 ± 1 mg, of selenium pellets (*Sigma-Aldrich, 99.999% purity, < ∅5 mm*) under a vacuum pressure of

800 ± 20 mbar. Se pellets were disposed along the samples perimeter inside the ceramic crucibles.

a) **b)** **c)**

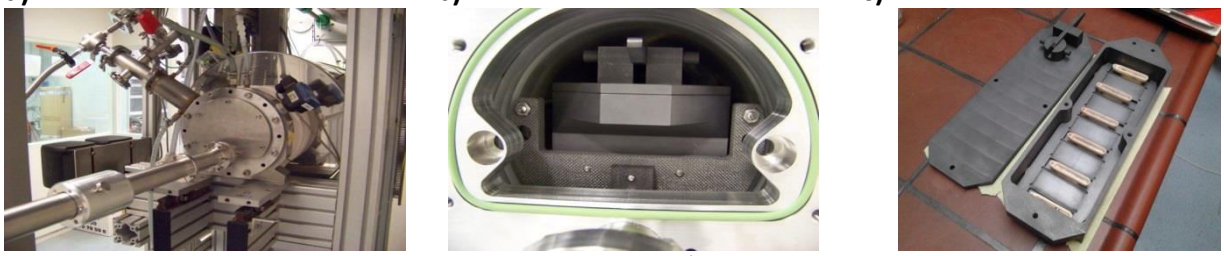

Figure App.II-3: Selenization equipment: **a)** RTP furnace, **b)** RTP load/unload port with selenization box and **c)** selenization box with ceramic Se holder.

A two-step temperature process was applied for the absorber formation. The sample box was introduced into the chamber at room temperature (*RT*) and vacuum was applied inside to remove dry air. Two recycling nitrogen-vacuum cycles were used to displace the undesired dry air of the furnace. The RTP oven was composed of 3 independently controlled regions, the settings of the first (*Z1*) and the second (*Z2*) zones were identical but the third (*Z3*) region was settled to a higher temperature. For the precursors selenization, a 24 minutes process was developed [7][8] (Figure App.II- 4). During the first 4 min a N_2 recycling atmosphere was employed. Additionally, regions 2 and 3 were settled at 350°C meanwhile the sample box was in the first zone at room temperature. When the temperature plateau in Z2 and Z3 was reached, the sample box was moved to Z2 to induce an annealing process of the precursors inside the sample holder. The real temperature of the sample was increasing from RT to 250 ± 10 °C during the annealing process, 8 min. In addition, the third region was set to 700°C with a temperature ramp of 1.5 °C/s 4 minutes after the starting point of the annealing process. Once the settled temperature was reached, the sample box was transferred to the Z3 and baked for 8 minutes. The temperature inside the sample box increased from 250 ± 10 °C to 550 ± 20 °C meanwhile the selenization process was carried out. Once the baking process was completed, the temperature of the Z3 was settled to room temperature and the sample holder was moved to the first region where the temperature was passively increased from RT to 80 ± 5 °C during the whole process. The sample box was passively cooled down inside the RTP oven for 60 minutes and outside the chamber, the samples were actively cooled down with a N_2 flow. During the complete process, the pressure was kept at a constant value by extracting the N_2/Se_X

air. CIGSe absorbers were produced with this technique presented a non-homogeneous CIGSe layer with a radial distribution.

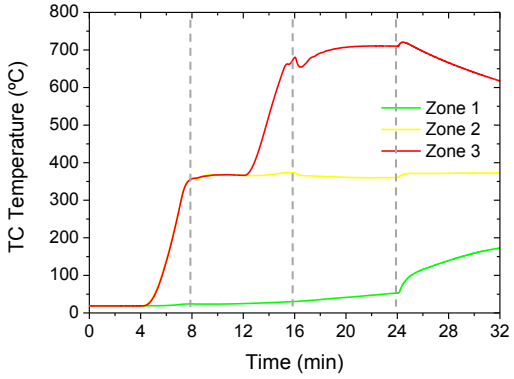

Figure App.II- 4: Setting of the selenization process, sample position: 0-8 min in Zone 1, 8-16 min in Zone 2, 16-24 min in Zone 3 and (cooling down) 24-84 min in Zone 1.

II.1.2. Co-evaporation fabrication process

Figure App.II- 5 shows the elemental deposition line at the co-evaporation process. Co-evaporation of Cu, Ga, In and Se elements at high temperature (>550°C) in a vacuum chamber were deposited to produce the CIGSe layer with a HZB PVD-A equipment by T. Köhler. CIGSe absorbers produced with this technique presented a homogeneous distribution.

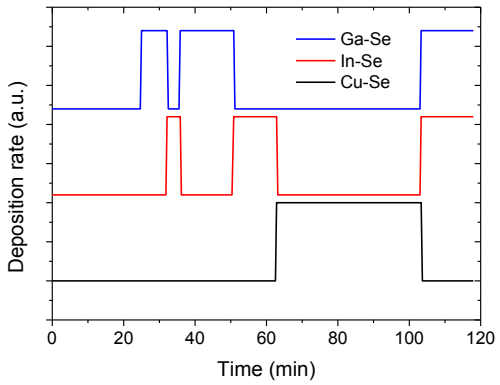

Figure App.II- 5: Co-evaporation step process used in HZB-Wannsee facilities.

II.1.3. Lithography process

Different lithography masks were designed for the fabrication of micrometer-sized solar cells. Round-shaped masks were tailored to be fabricated by the Technische Universität Berlin (*LM01#1-4*) and by the E. Rose Fotomasken Mikroelektronik company (*LM02#1-3*). Additionally,

lamellar-shaped patterns were tailored to be fabricated by laser scribing (with a characteristic wobble edges) by PVcomB (*PVcomB#50* to *#400*, in steps of *#50*).

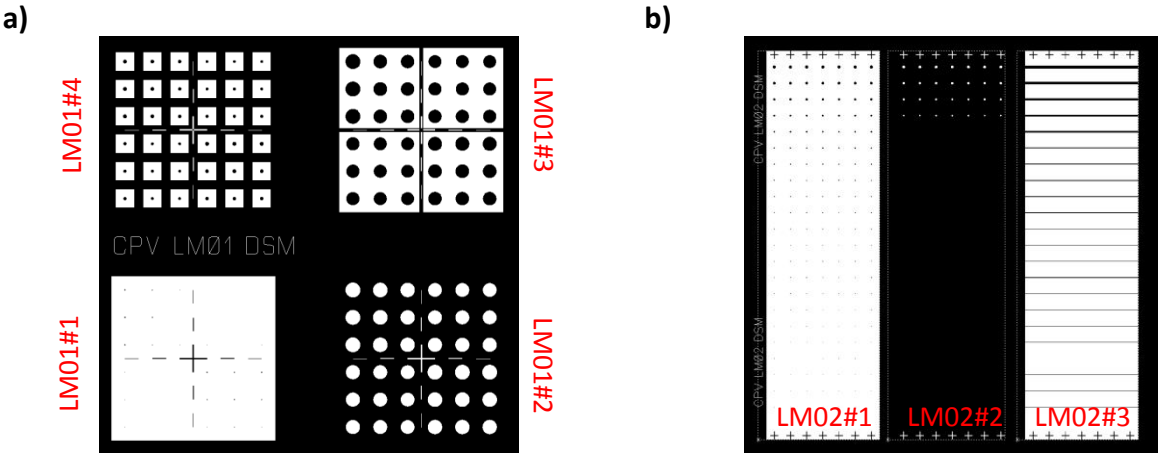

Figure App.II- 6: Round-shaped lithography masks (top view), **a)** LM01 mask divided in 4 sections and **b)** LM02 mask divided in 3 sections. The white areas correspond to Cr coated regions, i.e. no light travel through these areas.

LM01 lithography mask was composed of 4 independent sections, which were designed to produce micrometer-sized solar cells as follows. A photoresist layer was deposited on a Mo surface using the LM01#1 section with holes, diameters from 10 to 125 µm. The first attempt to create micro-sized solar cells was by evaporating SiO_x and by sputtering ZnO_x on the pre-patterned molybdenum (Figure App.II-7.1). After the lift off, a SiO_x/ZnO_x array was produced and CIG precursors were evaporated on the patterned surface (Figure App.II-7.2). The ZnO_x layer was removed with a $HCl:H_2O$ (1:3) solution [9] and the precursor laying on it was detached from the substrate at the same time. A posterior precursor selenization was developed but a cross contamination process of elements occurred. The remaining photoresist attached at the absorber was the mayor undesired contamination element. Additionally, to isolate electrically the cells, an intermediate photoresist layer (*LM01#2*) was deposited (Figure App.II-7.3). The buffer layer and the front contact were deposited on the patterned sample. The photoresist was lifted off removing the material attached on it. To ensure the isolation of the cells, a SiO_x layer was deposited on a pre-patterned (*LM01#3*) substrate (Figure App.II-7.4). After the development of the LM01#3 layer (Figure App.II-7.5), removing undesired SiO_x, a new pattern (*LM01#4*) was imprinted on the substrate (Figure App.II-7.6). The metal grid was evaporated and finally the remaining photoresist was removed (Figure App.II-7.7).

Figure App.II-7: Micro-sized solar cells process steps using LM01 lithography mask.

All samples fabricated with previous approach were under performance due to the absorber cross contamination. Therefore, a new deposition method was investigated using the LM02 lithography mask to avoid contamination.

II.2. Characterization

III.2.1. Glow-Discharge Optical Emission Spectroscopy (*GDOES*) characterization

The depth distribution of the elements measured by GDOES is shown in Figure App.II-8.

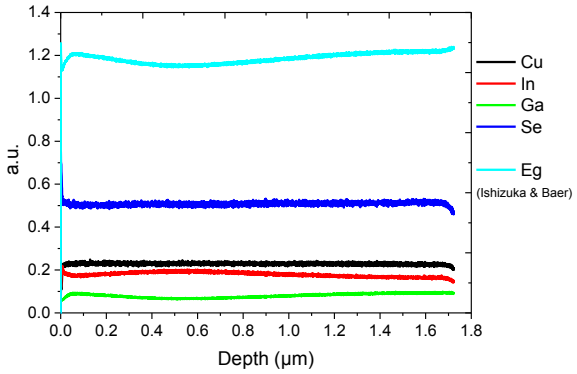

Figure App.II-8: GDOES characterization of a CIGSe reference solar cell.

A slightly noticeable grading was observed, with a minimum band gap of 1.128 ± 0.005 eV in a valley centred in 0.575 ± 0.010 µm from the pn-junction interface. A maximum band gap value was resulting at the rear interface of the absorber, 1.261 ± 0.005 eV at 1.700 ± 0.010 µm depth.

Appendix III

III.1. Optical constants

The optical constants of Mo, CIGSe, CdS, i-ZnO and AZO as reported in [47] shown in Figure App.III-1a-b were used for simulations purposes to calculate the amount of energy absorber as a function of the layer and wavelength.

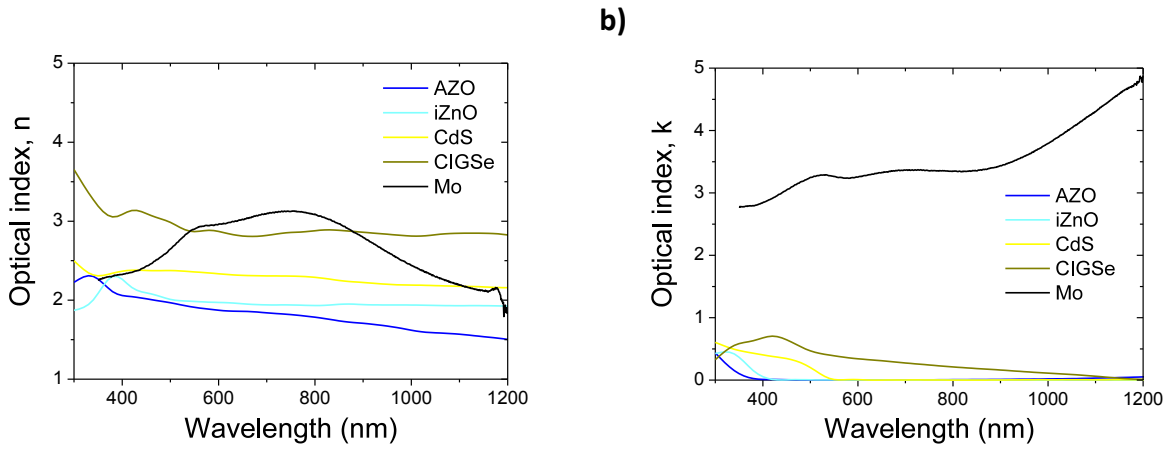

Figure App.III-1: Optical constants for each layer as a function of the wavelength used in the thermal-opto-electronic (TOE) simulations; **a)** n, **b)** k.

III.2. Model validations

For validating the model, different modifications were carried out to determine the best combination of parameters which fitted the I-V characteristic curve of the fabricated planar reference solar cells with an area of 0.5 cm^2. For simplicity, flat layers were implemented in the model and therefore, grain size, surface morphology or defects in the material were neglected. Moreover, a smoother film will increase the reflection from the film with respect to rougher layers with the subsequent energy loss. The opto-electronic properties were assumed to be identical and constant for intrinsic ZnO and for the aluminum-doped zinc oxide layers [100] [101] [102]. In this work, to simplify the validation of the model, the opto-electronic properties

of the absorber and buffer layers were investigated only. The opto-electronic characteristics for the different layers were obtained from the literature and used as a starting point for the simulations [100] [101] [102]. Different material properties could bring the same results. However, the selected parameters for the validation were based on the previous literature and were modified to represent the fabricated micrometer-sized solar cells. In general terms, the model implemented with the FEM software toolboxes reproduces the typical behavior of a solar cell. However, it is necessary to assume certain tolerances due to the internal process of the software to obtain results.

III.2.2. Band gap modifications

Modifications of the band gap of the absorber and buffer layers were performed to find the values, which fitted the performance of the reference solar cells. The I-V characteristic curve was calculated by varying the CIGSe band gap (Figure App.III-2a), keeping the other opto-electronic parameters invariable. In the same manner, the CdS band gap was varied but did not show a significant influence (Figure App.III-2b). The open-circuit voltage decreases as the CIGSe band gap decreases. However, the short-circuit current slightly increased by increasing the band gap of the absorber instead of decreasing. For the buffer layer, any noticeable increment or decrement was observed by varying the absorber band gap.

a) **b)**

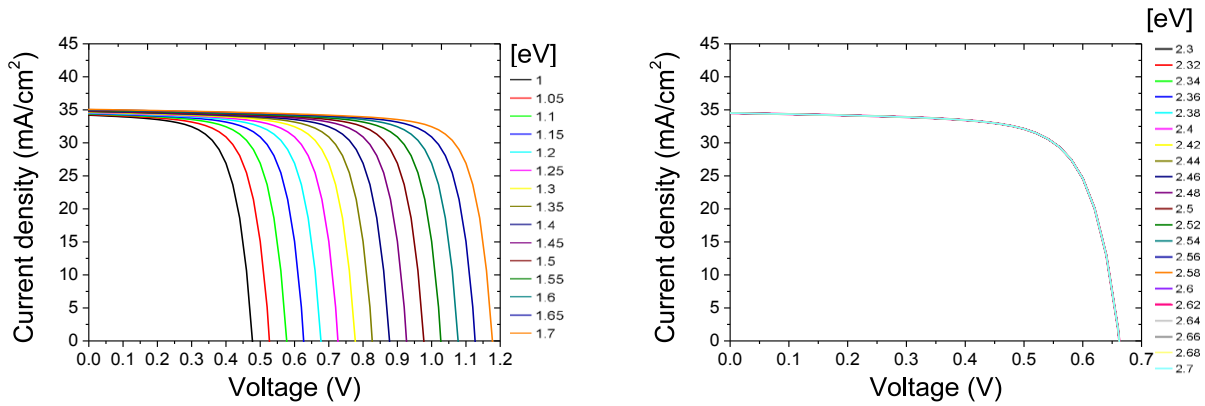

Figure App.III-2: Band gap modifications for TOE model verification; **a)** CIGSe and **b)** CdS (all cases overlapped).

III.2.3. Doping modifications

Modifications of the doping of the absorber and buffer layers were performed to find the values, which fitted the performance of the reference solar cells. By increasing the doping of the

CIGSe layer (Figure App.III-3a), keeping the other opto-electronic parameters invariable, the V_{oc} increased and the J_{sc} decreased. In the same manner, the CdS doping level was varied but did not show a significant influence (Figure App.III-3b).

a) **b)**

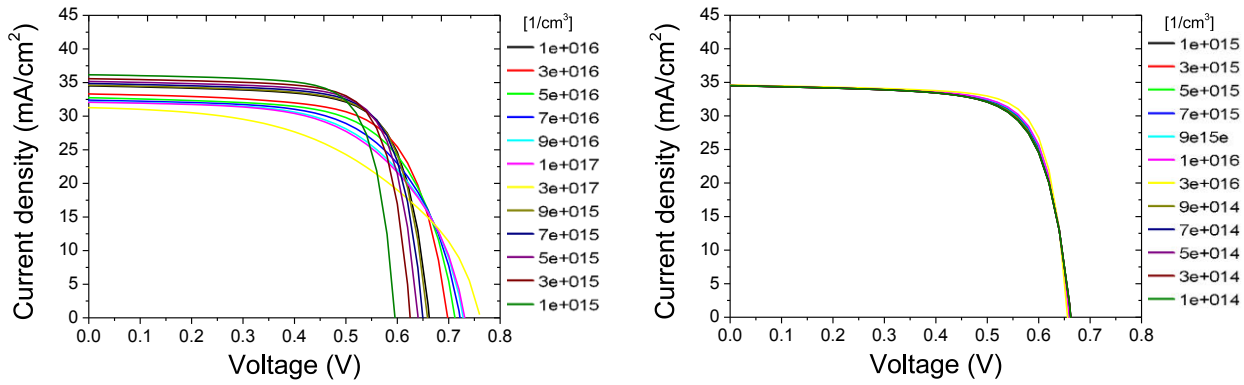

Figure App.III-3: Doping modifications for TOE model verification; **a)** CIGSe (acceptor) and **b)** CdS (donor) (all cases overlapped).

III.2.4. Lifetime modifications, e⁻

Modifications of the lifetime of the electrons in the absorber and buffer layers were performed to find the values, which fitted the performance of the reference solar cells. By increasing the electrons lifetime of the CIGSe layer (Figure App.III-4a), keeping the other opto-electronic parameters invariable, the V_{oc} and the J_{sc} increased. In the same manner, the electrons lifetime of the CdS layer was varied but did not show a significant influence (Figure App.III-4b).

a) **b)**

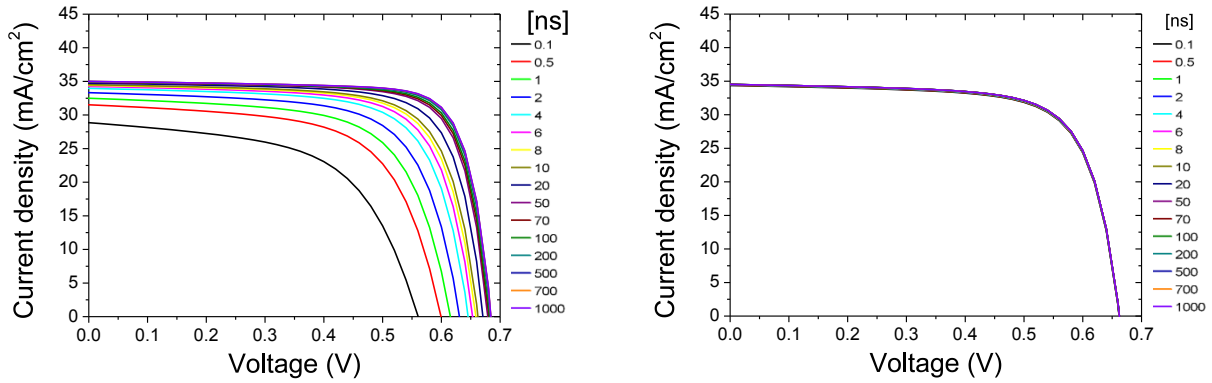

Figure App.III-4: Lifetime modifications for TOE model verification; **a)** CIGSe (electrons) and **b)** CdS (electrons) (all cases overlapped).

III.2.5. Lifetime modifications, h^+

Modifications of the lifetime of the holes in the absorber and buffer layers were performed to find the values, which fitted the performance of the reference solar cells. The I-V characteristic curve was calculated by varying the holes lifetime of the CIGSe layer (Figure App.III-5a), keeping the other opto-electronic parameters invariable. In the same manner, the holes lifetime of the CdS layer was varied (Figure App.III-5b). The V_{oc} and the J_{sc} did not show a significant influence by varying the electrons or holes lifetimes. However, the fill factor decreases by decreasing the lifetime of the holes at the absorber layer.

a) **b)**

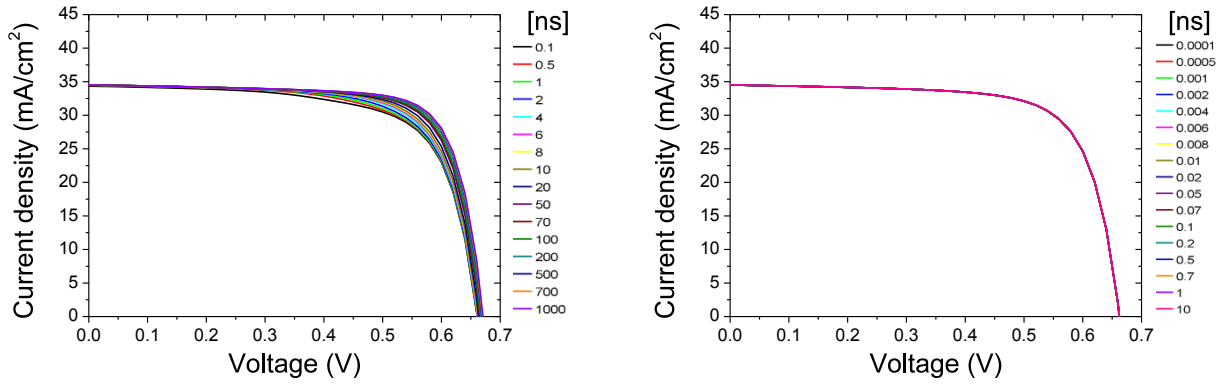

Figure App.III-5: Lifetime modifications for TOE model verification; **a)** CIGSe (holes) and **b)** CdS (holes) (all cases overlapped).

III.2.6. Other modifications

Modifications of the energy level between the defect level and the intrinsic level (Figure App.III-6a) were performed to observe the effect of this parameter in the intrinsic carrier density of states. By modifying the SRH energy level, the V_{oc} and the J_{sc} increased with respect to the values obtained without any modification. The effect of an ideal Schottky contact at the interface between the absorber and the back contact was also investigated. Modifications of the metal work function (Figure App.III-6b) were performed to observe the effect of this Schottky barrier in the performance of the solar cell. I-V characteristic curves as a function of the metal work function presented a threshold value, 4.7 eV, below that the performance of the solar cell was dramatically reduced.

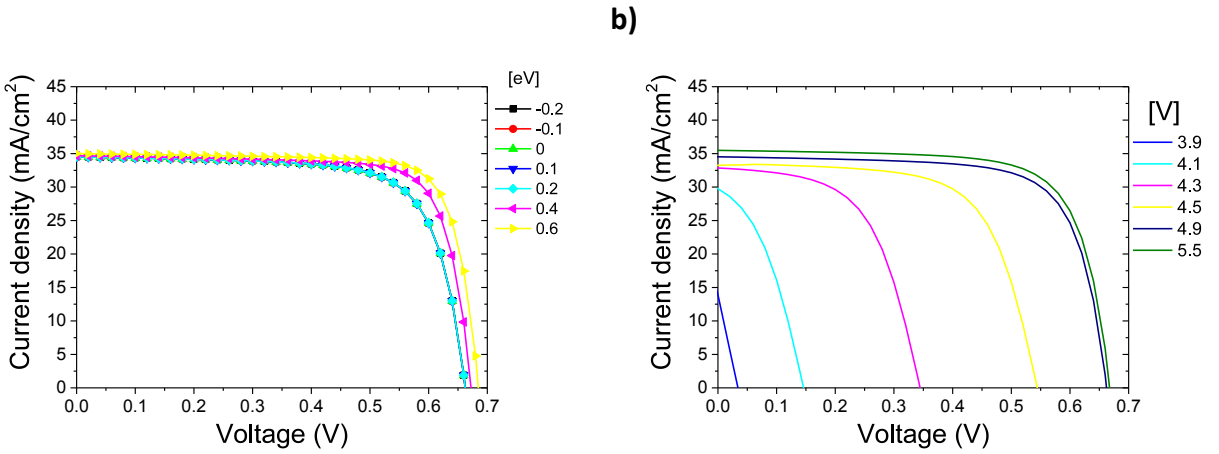

Figure App.III-6: Other modifications for TOE model verification; **a)** SRH energy level and **b)** metal work function (ideal ohmic) Mo/CIGSe.

The simulated I-V characteristic curve, obtained as a result of the different modifications of the intrinsic characteristics of the different materials contained in the solar cell, based on previous literature, differed slightly from the measured results of the reference solar cells (Figure App.III-7). Specifically, the short-circuit current density (J_{sc}) was reduced by 1.5% to 32.3 $\pm$ 0.1 mA/cm^2. The open-circuit voltage (V_{oc}) presented an increment of 0.9%, reaching 0.653 $\pm$ 0.048 V but the fill factor exhibited a reduction of 2.1%, dropping to 68.6 $\pm$ 2.3 %. The overall efficiency was found to be below the reference values in about 2.7%, reaching 14.5 $\pm$ 1.2 % of the power conversion to electricity. The simulated values obtained were in correlation with the experimental results presented in Chapter §5.

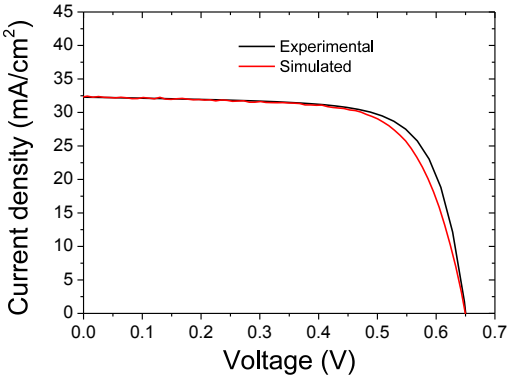

Figure App.III-7: Comparison of the experimental and simulated results for a planar solar cell under standard test conditions at 20°C.

The validated opto-electronic properties for the simulation of the planar reference solar cell were assumed for micrometer-sized and macroscopic solar cells. A detailed description of those properties was shown in Table 6.1.

Publications list

Here I present a summary of publications in which I have published my work.

Papers

D. Sancho-Martinez, M. Schmid, CPV limits for micrometer-sized chalcopyrite $Cu(In_x,Ga_{1-x})Se_2$ solar cells, in preparation.

D. Sancho-Martinez, M. Schmid, Thermal management approaches of $Cu(In_x,Ga_{1-x})Se_2$ micro-solar cells, Journal of Physics D: Applied Physics 50 (2017) 445501 (9pp).

M. Schmid, G. Yin, M. Song, S. Duan, B. Heidmann, **D. Sancho-Martinez**, S. Kämmer, T. Köhler, P. Manley, M.Ch. Lux-Steiner, Concentrating light in $Cu(In,Ga)Se_2$ solar cells, Journal of Photonics for Energy, 7 (2017), 018001.

M. Schmid, G. Yin, M. Song, S. Duan, B. Heidmann, **D. Sancho-Martinez**, S. Kämmer, T. Köhler, P. Manley, M.Ch. Lux-Steiner, Concentrating light in $Cu(In,Ga)Se_2$ solar cells. Proceedings of SPIE 9937 (2016), p. 993703/1-7.

Posters

D. Sancho-Martinez, T. Köhler, B. Heidmann, W. Raja, M. Schmid $Cu(In_x,Ga_{1-x})Se_2$ micro solar cells: Thermal and opto-electronic analysis and fabrication, 13th International Conference on Concentrator Photovoltaic System Ottawa, Canada (2017).

M. Schmid, E. Lotter, X. Lin, L. Wang, R. Klenk, K. Eylers, F. Ringleb, T. Boeck, B. Heidmann, G. Nenna, F. Loffredo, F. Villani, T. Köhler, **D. Sancho-Martinez**, T. Raadik, J. Krustok, M. Grossberg, M.Ch. Lux-Steiner, Micro concentrator concept for cost reduction and efficiency enhancement

of thin-film chalcopyrite photovoltaics: Results from EU joint research program CHEETAH, 33rd European Photovoltaic Solar Energy Conference and Exhibition, Amsterdam, Netherlands (2017)

D. Sancho-Martinez, B. Heidmann, P. Manley, R. Klenk, B. Reinhold, M. Ch. Lux-Steiner, M. Schmid, Modelling and fabrication of a photovoltaic $Cu(In_x,Ga_{1-x})Se_2$ micro solar cell under different light concentration fluxes. IW-CIGSTech 6, Berlin, Germany (2015).

D. Sancho-Martínez, B. Heidmann, P. Manley, R. Klenk, B. Reinhold, M. Ch. Lux-Steiner, M. Schmid, Modelling and fabrication of a photovoltaic $Cu(In_x,Ga_{1-x})Se_2$ micro solar cell under different light concentration fluxes. 11th International Conference on Concentrator Photovoltaic System Chambery, France (2015).

M. Schmid, G. Yin, M. Song, S. Duan, B. Heidmann, **D. Sancho-Martinez**, S. Kämmer, T. Köhler, P. Manley, M.Ch. Lux-Steiner, Concentrating light in $Cu(In,Ga)Se_2$ solar cells. SPIE Optics + Photonics, USA (2016).

Bibliography

[1] U.S. Energy Information Administration, "International Energy Outlook 2017," [Online]. Available: https://www.eia.gov/outlooks/ieo/.

[2] U.S. Internal Revenue Service, "1 barrel equal to 159 liters, 5.8 Mega-BTU, i.e. 6.1 Giga-Joule, 1.7 Mega-Wh.," [Online]. Available: https://www.irs.gov/.

[3] United Nations Climate Conference Goals, 2017. [Online]. Available: http://www.un.org/sustainabledevelopment/sustainable-development-goals/.

[4] Renewable Energy Policy Network for the 21st Century, REN21, "Renewables 2017: Global status report," [Online]. Available: http://www.ren21.net/wp-content/uploads/2017/06/17-8399_GSR_2017_Full_Report_0621_Opt.pdf.

[5] National Renewable Energy Laboratory (NREL), "Research cell record efficiency chart," [Online]. Available: https://www.nrel.gov/pv/assets/images/efficiency-chart.png.

[6] Frauhofer-ISE, "New world record for solar cell efficiency at 46%.(2014)," [Online]. Available: https://www.ise.fraunhofer.de/en/press-media/press-releases/2014/new-world-record-for-solar-cell-efficiency-at-46-percent.html.

[7] Katie Shanks et al., "Optics for concentrating photovoltaics: Trends, limits and opportunities for materials and design," *Renewable and Sustainable Energy Reviews 60 (2016) 394–407, doi:/10.1016/j.rser.2016.01.089.*

[8] Pablo Benitez et al., "High performance Fresnel-based photovoltaic concentrator," *Opt. Express 18, A25-A40 (2010), doi:/10.1364/OE.18.000A25.*

[9] Guido Vallerotto et al., "A novel achromatic Fresnel lens for high concentrating photovoltaic systems," *AIP Conference Proceedings 1766, 050007 (2016). doi:/10.1063/1.4962089.*

[10] M. Hernández et al., "Imagen High-performance Köhler concentrators with uniform irradiance on solar cell," *Proc. SPIE 7059, Nonimaging Optics and Efficient Illumination Systems V, 705908 (2 September 2008), doi:/10.1117/12.794927.*

[11] British Geological Survey, "Risk list 2015 - Current supply risk for chemical elements or element group which are of economic value," [Online]. Available: http://www.bgs.ac.uk/mineralsuk/statistics/risklist.html.

[12] Kenji Araki et al., "A simple-passive coolingstructure and its heat analysis for 500 X concentrator PV module," *Photovoltaic Specialists Conference, 2002. Conference Record of the Twenty-Ninth IEEE, doi:/10.1109/PVSC.2002.1190913.*

[13] Diego Sancho-Martinez et al., "Thermal management approaches of $Cu(In_x,Ga_{1-x})Se_2$ micro-solar cells," *J. Phys. D: Appl. Phys. 50 (2017) 445501, doi:/10.1088/1361-6463/aa8ac5.*

[14] Ye Zhangbo et al., "The cooling technology of solar cells under concentrated system," *Power Electronics and Motion Control Conference, 2009. IPEMC '09. IEEE 6th International, doi:/10.1109/IPEMC.2009.5157766.*

[15] Nicholas J. Ekins-Daukes et al., "What does CPV need to achieve in order to succeed?," *AIP Conference Proceedings 1766, 020004 (2016); doi:/10.1063/1.4962072.*

[16] Solar Frontier K.K., "Solar Frontier Achieves World Record Thin-Film Solar Cell Efficiency of 22.9%," [Online]. Available: http://www.solar-frontier.com/eng/news/2017/1220_press.html.

[17] ZSW, "ZSW Sets New World Record for Thin-film Solar," [Online]. Available: https://www.zsw-bw.de/fileadmin/user_upload/PDFs/Pressemitteilungen/2016/pr09-2016-ZSW-WorldRecordCIGS.pdf.

[18] Rudmann et al., "Efficiency enhancement of $Cu(In,Ga)Se_2$ solar cells due to post-deposition Na incorporation," *Appl. Phys. Lett. 84, 1129 (2004), doi:/10.1063/1.1646758.*

[19] Philip Jackson et al., "Compositional investigation of potassium doped $Cu(In,Ga)Se_2$ solar cells with efficiencies up to 20.8%," *Phys Stat Sol (RRL) – Rapid Res Lett 2014, 8:219–222, doi:/10.1002/pssr.201409040.*

[20] Christopher P. Muzzillo, "Review of grain interior, grain boundary, and interface effects of K in CIGS solar cells: Mechanisms for performance enhancement," *Solar Energy Materials and Solar Cells 172 (2017) 18–24, doi:/10.1016/j.solmat.2017.07.006.*

[21] Philip Jackson et al., "Effects of heavy alkali elements in $Cu(In,Ga)Se_2$ solar cells with efficiencies up to 22.6%," *P hys. Status Solidi RRL 10, No. 8, 583–586 (2016), doi:/10.1002/pssr.201600199.*

[22] Albert Polman et al., "Photonic design principles for ultrahigh-efficiency photovoltaics," *Nature Materials 11, 174–177 (2012), doi:/10.1038/nmat3263.*

[23] Guanchao Yin et al., "Integration of plasmonic Ag nanoparticles as a back reflector in ultra-thin $Cu(In,Ga)Se_2$ solar cells," *Applied Surface Science, Volume 355, 15 November 2015, Pages 800–804.*

[24] Sascha Sadewasser et al., "Materials efficient deposition and heat management of CISe microconcentrator solar cells," *Solar Energy Materials & Solar Cells 159 (2017) 496–502, doi:/10.1016/j.solmat.2016.09.041.*

[25] Pierre Albert et al., "Submillimeter multijunction solar cells: Impact of dimensions, design and architecture on electrical performances. (Poster)," *CPV-13 Conference (2017).*

[26] Tian Gu et al., "Wafer integrated micro-scale concentrating photovoltaic. (Presentation)," *CPV-13 Conference (2017).*

[27] AZUR SPACE Solar Power, "Sponsor presentation. (Presentation)," *CPV-13 Conference (2017).*

[28] Panasonic Corporation, "PIC: New concept of CPV module offering high performance at low cost. (Presentation)," *CPV-13 Conference (2017).*

[29] Erwin Lotter et al., "Identification of loss mechanism in CIGS micro-cells for concentrator applications," *32nd European Photovoltaic Solar Energy Conference and Exhibition (2016).*

[30] Myriam Paire et al., "Toward microscale Cu(In,Ga)Se_2 solar cells for efficient conversion and optimized material usage: Theoretical evaluation," *Applied Physics, American Institute of Physics, 2010, 108, pp.034907, doi:/10.1063/1.3460629.*

[31] Myriam Paire et al., "Microscale solar cells for high concentration on polycrystalline Cu(In,Ga)Se_2 thin films," *Appl. Phys. Lett. 98, 264102 (2011), doi:/10.1063/1.3604789.*

[32] Sebastien Jutteau et al., "Study of a micro-CPV system based on Cu(In,Ga)Se_2 microcells array," *Appl. Opt. 2016 Aug 20; 55(24):6656-61, doi:/10.1364/AO.55.006656.*

[33] Bernhard Reinhold et al., "Monolithically interconnected lamellar Cu(In,Ga)Se_2 micro solar cells under full white light concentration," *Progress in Photovoltaics: Research and Applications (2015), doi:/10.1002/pip.2611.*

[34] Berit Heidmann et al., "Local growth of $CuInSe_2$ micro solar cells for concentrator application," *Materials Today Energy 6 (2017) 238-247, doi:/10.1016/j.mtener.2017.10.010.*

[35] COMSOL Multiphysics, Finite element analysis, solver and simulation software (version 5.3, 2017), [Online]. Available: https://www.comsol.com/.

[36] AZoM, "AZoNetwork UK Ltd (2016)," [Online]. Available: http://www.azom.com/.

[37] The Engineering Toolbox, "(2016)," [Online]. Available: http://www.engineeringtoolbox.com/convective-heat-transfer-d_430.html.

[38] COMSOL Multiphysics, "Heat Transfer Module, User´s Guide (version 5.2a, 2016)".

[39] Antonio Luque, Cu(In,Ga)Se_2 Solar Cells, in Handbook of Photovoltaic Science and Engineering, John Wiley & Sons, Ltd, Chichester, UK (2003), doi:/10.1002/0470014008.ch13..

[40] Su-Huai Wei et al., "Effects of Ga addition to $CuInSe_2$ on its electronic, structural, and defect properties," *Applied Physics Letters 72, 3199 (1998), doi:/10.1063/1.121548.*

[41] Thomas Unold et al. , "Photoluminescence Analysis of Thin-Film Solar Cells," in *Advanced Characterization Techniques for Thin Film Solar Cells (eds D. Abou-Ras, T. Kirchartz and U. Rau), Wiley-VCH Verlag GmbH & Co. KGaA, Weinheim, Germany, doi:/10.1002/9783527636280.ch7*.

[42] Antonio Luque and Steven Hegedus, The Physics of the Solar Cell, in Handbook of Photovoltaic Science and Engineering, John Wiley & Sons, Ltd, Chichester, UK (2003), doi:/10.1002/0470014008.ch3..

[43] ASTM International, "ASTM G173-03(2012), Standard Tables for Reference Solar Spectral Irradiances: Direct Normal and Hemispherical on 37° Tilted Surface, ASTM Internationa, 2012, doi:/10.1520/G0173-03R12".

[44] Olivier Dupré, "Physics of the temperature coefficients of solar cells," *Solar Energy Materials and Solar Cells, Volume 140, September 2015, Pages 92-100, doi:/10.1016/j.solmat.2015.03.025.*

[45] Myriam Paire et al., "Characterization of $Cu(In,Ga)Se_2$ electrodeposited and co-evaporated devices by means of concentrated illumination," *Ieee Journal of Photovoltaics, Vol. 4, No. 2, March 2014, doi:/10.1109/JPHOTOV.2013.2293889.*

[46] Svante Arrhenius, "Über die Dissociationswärme und den Einfluss der Temperatur auf den Dissociationsgrad der Elektrolyte," *Z. Phys. Chem. 4 (1889) 96-116,* doi:/10.1515/zpch-1889-0408.

[47] G. Yin, "Preparation of ultra-thin $CuIn_{1-x}Ga_xSe_2$ solar cells and their light absorption enhancement," *Technische Universität Berlin (2015).*

[48] Melanie Nichterwitz, "Charge carrier transport in $Cu(In,Ga)Se_2$ thin-film solar-cells studied by electron beam induced current and temperature and illumination dependent current voltage analyses," *Technische Universität Berlin (2012).*

[49] Qing Cao et al., "Defects in $Cu(In,Ga)Se_2$ chalcopyrite semiconductors: a comparative study of material properties, defect states, and photovoltaic performance," *Adv. Energy Mater. 2011, 1, 845–853, doi:/10.1002/aenm.201100344.*

[50] Leonid A. Kosyachenko et al., "Optical and recombination losses in thin-film $Cu(In,Ga)Se_2$ solar cells," *Solar Energy Materials & Solar Cells 130 (2014) 291–302, doi:/10.1016/j.solmat.2014.07.019.*

[51] Gerhard Peharz et al., "Energy payback time of the high-concentration PV system FLATCON," *Prog. Photovolt: Res. Appl. 2005; 13:627–634, doi:/10.1002/pip.621.*

[52] Greg Nielson, "Cost analysis for flat-plate concentrators employing microscale photovoltaic cells," *IEEE 39th Photovoltaic Specialists Conference (PVSC) 2013, Conference paper,*

doi:/10.1109/PVSC.2013.6745185.

[53] Avancis, "PowerMax® Premium class solar module (2016)," [Online]. Available: http://www.avancis.de/en/products/powermaxr/.

[54] John H. Scofield et al, "Sputtered Molybdenum Bilayer Back Contact for Copper Indium Diselenide-Based," *Thin Solid Films, 260 (1), pp. 26-31 (May 1, 1995), doi:/10.1016/0040-6090(94)06462-8.*

[55] H.A. Al-Thani et al., "The Effect of Mo Back Contact on Na Out-Diffusion and Device Performance of Mo/Cu(In,Ga)Se_2/CdS/ZnO Solar Cells," *29th IEEE PV Specialists Conference (2002).*

[56] Ju-Heon Yoon et al., "Effect of a Mo back contact on Na diffusion in CIGS thin film solar cells," *Prog. Photovolt: Res. Appl. 2013; 21:58–63, doi:/10.1002/pip.2193.*

[57] Manz GmbH, "CIGS MODULES & BIPV: High-performance CIGS thin-film solar modules and building-integrated photovoltaics from the CISGinnoline (2016)".

[58] Saint-Gobain, "Saint-Gobain-Glass Brouches (2018)," [Online]. Available: http://uk.saint-gobain-glass.com/category/uploadtag/brochures.

[59] Stefan Puttnins et al., "Breakdown characteristics of flexible Cu(In,Ga)Se_2 solar cells," *Solar Energy Materials & Solar Cells 120 (2014) 506–511, doi:/10.1016/j.solmat.2013.09.031.*

[60] Priyanka Singh et al., "Temperature dependence of solar cell performance - an analysis," *Solar Energy Materials & Solar Cells 101 (2012) 36-45, doi:/10.1016/j.solmat.2012.02.019.*

[61] J.L. Johnson et al., "Effects of 2nd Phases, Stress, and Na at the Mo/Cu_2ZnSnS_4 Interface," *MRS Proceedings, 1268 (2010), doi:/10.1557/PROC-1268-EE03-03..*

[62] K. Orgassa et al., "Alternative back contact materials for thin film Cu(In,Ga)Se_2 solar cells," *Thin Solid Films 431 –432 (2003) 387–391, doi:/10.1016/S0040-6090(03)00257-8.*

[63] Fraunhofer ISE and NREL, "Current status of concentrator photovoltaics (CPV) technology (2017)," [Online]. Available: www.ise.fraunhofer.de/en/renewable-energy-data.

[64] Linak, "Improving energy efficiency (2017)," [Online]. Available: http://www.linak.com/techline/?id3=2236.

[65] David C. Miller et al., "Durability of Fresnel lenses: A review specific to the concentrating photovoltaic application," *Solar Energy Materials & Solar Cells 95 (2011) 2037–2068, doi:/10.1016/j.solmat.2011.01.031.*

[66] Hasan Baig et al, , "Non-uniform illumination in concentrating solar cells," *Renewable and Sustainable Energy Reviews 16 (2012) 5890–590, doi:/10.1016/j.rser.2012.06.020.*

[67] HZB (EE-NOPT group), "Supernano computer details: Intel(R) Xeon(R) CPU E5-2650 v2 @ 2.60Ghz (2 processors) 128 GB RAM".

[68] Hong Quang Nguyen et al., "The Role of the Heterointerfaces in the Cu(In,Ga)Se_2 Thin Film Solar Cell with Chemical Bath Deposited Buffer Layers," *OPUS (2004), doi:/10.18419/opus-776.*

[69] J Wennerberg et al., "Design and stability of Cu(In,Ga)Se_2-based solar cell modules," *DiVA (2002), diva2:161227.*

[70] A. Duchatelet et al., "A new deposition process for Cu(In,Ga)$(S,Se)_2$ solar cells by one-step electrodeposition of mixed oxide precursor films and thermochemical reduction," *J. Renewable Sustainable Energy, vol. 5, no. 1, p. 011203, 2013, doi:/10.1063/1.4791782.*

[71] Xianzhong Lin et al., "Structural and optical properties of Cu_2ZnSnS_4 thin film absorbers from ZnS and Cu_3SnS_4 nanoparticle precursors.," *Thin Solid Films, vol. 535, no.1, pp.10–13, 2013, doi:/10.1016/j.tsf.2012.10.034.*

[72] Titus J. Rinke and Christian Koch, Photolithography: Basics of Microstructuring (2017), MicroChemicals GmbH.

[73] Marc J. Madou, Fundamentals of Microfabrication: The Science of Miniaturization, Second Edition (2002), CRC Press, ISBN 9781482274004 - CAT# KE28561.

[74] Karl Suss, Operator's reference manual: MJB-3 (1984), Karl Suss.

[75] MicroChemicals GmbH, "AZ nLOF 20xx series (2005)," [Online]. Available: https://www.microchemicals.com/technical_information/az_nLof_20xx_additional_informations.pdf.

[76] ZEISS GmbH, "Education in Microscopy and Digital Imaging (2017)," [Online]. Available: http://zeiss-campus.magnet.fsu.edu/articles/lightsources/mercuryarc.html.

[77] J. Parisi et al., "Schottky contact analysis of photovoltaic chalcopyrite thin film absorbers," *Physics Letters A 362 (2007) 229–233, doi:/10.1016/j.physleta.2006.10.039.*

[78] Myrian Paire et al. , "Cu(In,Ga)Se_2 mesa diodes for the study of edge recombination," *Thin Solid Film 582 (2015) 258-262, doi:/10.1016/j.tsf2014.11.033.*

[79] Marco Calicchio, "Technological processes for CIGS based solar cells," *University of Parma, (2013), Dissertation.*

[80] Eric Perozzielo et al. , "Method for patterning a photovoltaic device comprising CIGS material using an etch process". US Patent 20070227578 A1, 4 10 2007.

[81] Sven Schönherr et al., "High lateral resolution energy dispersive X-ray spectroscopy and

cathodoluminiscence on lamellae of CIGSe solar cells," *Photovoltaic Specialist Conference (PVSC), 2014 IEEE 40th. doi:/10.1109/PVSC.2014.6925248.*

[82] F.A. Padovani and R. Stratton, "Field and thermionic-field emission in shcottky barrieirs," *Solid-State Electronics, Volume 9, Issue 7, July 1966, Pages 695-707, doi:/10.1016/0038-1101(66)90097-9.*

[83] A. R. Riben and D. L. Feucht, "nGe-pGaAs heterojunctions," *Microelectronics Reliability, Volume 6, Issue 3, August 1967, Page 249, doi:/10.1016/0026-2714(67)90312-5.*

[84] ASTM International, "ASTM E927-10(2015), Standard Specification for Solar Simulation for Photovoltaic Testing, doi:/10.1520/E0927-10R15".

[85] International Electrotechnical Commission, "IEC 60904-9:2007," *https://webstore.iec.ch/publication/3880#additionalinfo.*

[86] "Durable and Cost-Effective Neutral Density Filters Utilizing Multiple Reflections in Glass Slide Stacks," *IEEE Photonics Journal, Volume 9, Issue 6, 2017, doi:/ 10.1109/JPHOT.2017.2773500.*

[87] U.S. Department of commerce, "Calculations for comparing two-point and four-point probe resistivity measurements on rectangular bar-shaped semiconductor samples," *National bureau of standards, technical note 241, 1964.*

[88] C. J. R. Sheppard and M. Hrynevych, "Diffraction by a circular aperture: a generalization of Fresnel diffraction theory," *J. Opt. Soc. Am. A 9, 274-281 (1992), doi:/10.1364/JOSAA.9.000274.*

[89] Yasoo Harada et al., "Preferential etching and etched profile of GaAs," *Journal of Electrochemical Society, 1971, volume 118, issue 1, 118-122 doi:/10.1149/1.2407921.*

[90] Myrian Paire et al., "Thin-film microcells: a new generation of photovoltaic devices," *SPIE Newsroom (2013), doi:/10.1117/2.1201305.004808.*

[91] Wolfram Witte et al., "Gallium gradients in Cu(In,Ga)Se_2 thin-film solar cells," *Prog. Photovolt: Res. Appl. 2015; 23:717–733. doi:/10.1002/pip.2485.*

[92] Hakim Marko et al., "Influence of Cu off-stoichiometry on wide band gap CIGSe solar cells," *Thin Solid Films 519 (2011) 7228–7231, doi:/10.1016/j.tsf.2010.12.174.*

[93] Tim Kodalle et al., "Investigating sulfur distribution and corresponding bandgap grading in C(In,Ga)$(S,Se)_2$ absorber layers processed by fast atmospheric calcogenization of metal precursors," *Journal of Alloys and Compounds 703 (2017) 600-604, doi:/10.1016/j.jallcom.2017.01.329.*

[94] Yasuhiro Aida et al., "Cu-rich $CuInSe_2$ solar cells with a Cu-poor surface," *Prog. Photovolt: Res. Appl. 2015; 23:754–764, doi:/10.1002/pip.2493.*

[95] Clément Colin, "Metallic nano-structures for light-trapping in ultra-thin GaAs and CIGS solar cells," *Thesis (2014) Université Paris Sud, https://tel.archives-ouvertes.fr/tel-00998396.*

[96] Ingrid Repins et al., "Comparison of device performance and measured transport parameters in widely-varying Cu(In,Ga)(Se,S) solar cells," *Prog. Photovolt: Res. Appl. 2006; 14:25-43. doi:/10.1002/pip.654.*

[97] Myrian Paire et al., "Cu(In,Ga)Se_2 microcells: High efficiency and low material consumption," *Journal of renewable and sustainable energy 5, 011202 (2013), doi:/10.1063/1.4791778.*

[98] Ignacio Rey-Stolle et al., Handbook of concentrator photovoltaic technology (2016), John Wiley & Sons, Aturim.

[99] Pengyun Huo et al., "Al-based front contacts for HCPV solar cell," *AIP Conference Proceedings 1881, 040004 (2017), doi:/10.1063/1.5001426.*

[100] Janez Krc et al., "Optical and electrical modeling of Cu(In,Ga)Se_2 solar cells," *Optical and Quantum Electronics (2006) 38:1115–1123. doi:/10.1007/s11082-006-9049-1.*

[101] M. Gloeckler et al., "Numerical modelling of CIGS and CdTe solar cells: setting the baseline," *3rd World Conference on Photovoltaic Energy Conversion, May 11-18, 2003, Osoka, Japan (Poster).*

[102] Soumaila Ouedraogo et al., "Optimization of Copper Indium Gallium Di-Selenide (CIGS) based solar cells by back grading," *Journal of Ovonic Research, Vol.9, No.4, July - August 2013, p. 95 - 103, doi:/10.1109/AFRCON.2013.6757813.*

[103] Jean Christian Bernède et al., "Study of the Mo thin films and Mo/CIGS interface properties," *Applied Surface Science 246 (2005) 159–166, doi:/10.1016/j.apsusc.2004.11.020.*

[104] Torben Klinkert et al., "New insights into the Mo/Cu(In,Ga)Se_2 interface in thin film solar cells: Formation and properties of the MoSe2 interfacial layer," *The Journal of Chemical Physics 145, 154702 (2016), doi:/10.1063/1.4964677.*

[105] HZB-Nanooptix, "4% Sequential two-step process efficiency (2014)".

Abstract

Concentrator photovoltaic (*CPV*) is a cost-effective method for energy generation with a high photovoltaic conversion rate. Highly efficient solar cells, which are based on III-V semiconductor materials, are used for CPV applications present a higher cost with respect to other material-based solar cells. To achieve a price reduction in this technology and, therefore, a higher integration and expansion of this renewable source of energy, efforts must be made to simplify each element contained in a CPV device. Every single element, from the optical system to the cooling device through the solar cell material, must be modified to reduce its cost without decreasing the overall performance of the solar cell. In this work, thanks to the funding from the Helmholtz-Association for Young Investigator groups within the Initiative and Networking fund (VH-NG-928) and the funding from the European Union Seventh Framework Programme (FP7/2007-2013) under grant agreement n° 609788, micrometer-sized chalcopyrite-based solar cells, specifically, $Cu(In_x,Ga_{1-x})Se_2$ (*CIGSe*), were investigated in detail to reduce the requirements of this technology for concentration purposes.

In the first part of this work, FEM simulations were employed to predict the heat management of micrometer-sized CIGSe solar cells in order to verify the benefits of cell minimization under concentrated light. These novel findings were obtained by varying different structure elements to find out the best configuration for high concentration. High concentration factors and high material saving, up to 10^5x, are feasibly to be applied on micrometer-sized CIGSe solar cells. In the second part of this work, based on these investigative thermal simulations, micrometer-sized CIGSe solar cells were fabricated via "*top-down approach*" and characterized by different techniques. The morphology as well as the elemental composition and distribution were investigated in order to characterize the quality of the fabricated solar cells. In addition, electrical characterizations were carried out, specifically, photoluminescence, current-voltage characteristic curve as a function of the temperature and as a function of the concentrated light, to determine the main opto-electronic parameters of the micrometer-sized CIGSe solar cells. These properties were dramatically affected by the fabrication method as the active area was reduced due to a higher SRH recombination mechanism. Higher recombination and the temperature increment of the solar cell during I-V measurements resulted in a maximum power conversion to electricity, i.e. efficiency, under concentrated light in the range of 20x to 50x and in the range of 20x to 30x for shaded and etched cells, respectively.

Finally, a 3D thermal-opto-electronic (*TOE*) model was successfully validated and employed to simulate the experimental setup as well as the ideal one, where the active area of the solar cell is only illuminated. These simulations predicted the output parameters of micrometer-sized CIGSe solar cells under all considered concentration factors and beam profiles in this work. The results extracted from the TOE model were compared with those of the experiments, and therefore, assessing and verifying such model. These simulations exhibited a good correlation under STC-20°C and under concentrated light with respect to those obtained experimentally. These simulations forecast the application of higher concentration factors, above 100x, to micrometer-sized CIGSe solar cells without lessening the overall performance by taking advantage of cell miniaturization.

Kurzfassung

Concentrator photovoltaic (CPV) ist eine kostengünstige Methode zur Energieerzeugung mit hoher photovoltaischer Umwandlungsrate. Hocheffiziente Solarzellen, die auf III-V-Halbleitermaterialien basieren, werden für CPV-Anwendungen eingesetzt, die gegenüber anderen materialbasierten Solarzellen einen höheren Aufwand darstellen. Um eine Preissenkung bei dieser Technologie und damit eine höhere Integration und Erweiterung dieser erneuerbaren Energiequelle zu erreichen, müssen Anstrengungen unternommen werden, um jedes in einem CPV-Gerät enthaltene Element zu vereinfachen. Jedes einzelne Element, vom optischen System bis zum Kühlgerät durch das Solarzellenmaterial, muss modifiziert werden, um seine Kosten zu reduzieren, ohne die Gesamtleistung der Solarzelle zu verringern. In dieser Arbeit dank der Finanzierung der Helmholtz-Gemeinschaft für Nachwuchsgruppen im Rahmen des Initiative und Networking-Fonds (VH-NG-928) und der Finanzierung aus dem Siebten Rahmenprogramm der Europäischen Union (RP7 / 2007-2013) gemäß der Finanzhilfevereinbarung Nr. 609788, Mikrometer Solarzellen auf der Basis von Chalkopyrit, speziell $Cu(In_x,Ga_{1-x})Se_2$ (CIGSe), wurden im Detail untersucht, um die Anforderungen dieser Technologie für Konzentrationszwecke zu reduzieren.

Im ersten Teil dieser Arbeit wurden FEM-Simulationen zur Vorhersage des Wärmemanagements von Mikrometer-großen CIGSe-Solarzellen verwendet, um die Vorteile der Zellminimierung unter konzentriertem Licht zu untersuchen. Diese neuartigen Ergebnisse wurden durch Variation verschiedener Hohe Konzentrationsfaktoren und hohe Materialeinsparungen von bis zu 10^5x sind für CIGSe-Solarzellen in Mikrometergröße praktikabel. Im zweiten Teil dieser Arbeit wurden basierend auf diesen thermischen Simulationen Mikrometer-große CIGSe-Solarzellen mittels "Top-Down-Ansatz" hergestellt und durch verschiedene Techniken charakterisiert. Die Morphologie sowie die Elementzusammensetzung und -verteilung wurden untersucht, um die Qualität der hergestellten Solarzellen zu charakterisieren. Zusätzlich wurden elektrische Charakterisierungen durchgeführt, und zwar Photolumineszenz, Strom-Spannungs-Kennlinie in Abhängigkeit von der Temperatur und in Abhängigkeit vom konzentrierten Licht, um die optoelektronischen Hauptparameter der mikrometergroßen CIGSe-Solarzellen zu bestimmen. Diese Eigenschaften wurden durch die Herstellungsmethode dramatisch beeinflusst, da die aktive Fläche aufgrund eines höheren SRH-Rekombinationsmechanismus reduziert wurde. Eine höhere Rekombination und der Temperaturanstieg der Solarzelle während IV-Messungen führten zu einer maximalen Leistungsumwandlung in Elektrizität, dh Effizienz, unter konzentriertem Licht im Bereich von 20x bis 50x und im Bereich von 20x bis 30x für abgeschattete bzw. geätzte Zellen.

Schließlich wurde ein 3D-Thermo-Opto-Elektronisches (TOE) -Modell erfolgreich validiert und eingesetzt, um den experimentellen Aufbau zu simulieren, sowie das Ideal, bei dem die aktive Fläche der Solarzelle nur beleuchtet wird. Diese Simulationen haben die Ausgangsparameter von Mikrometer-großen CIGSe-Solarzellen unter Berücksichtigung aller in dieser Arbeit berücksichtigten Konzentrationsfaktoren und Strahlprofile vorhergesagt. Die Ergebnisse, die aus dem TOE-Modell extrahiert wurden, wurden mit denen der Experimente verglichen und somit ein solches Modell bewertet und verifiziert. Diese Simulationen zeigten eine gute Korrelation unter STC-20ºC und unter konzentriertem Licht bezüglich der experimentell erhaltenen. Diese Simulationen prognostizieren die Anwendung höherer Konzentrationsfaktoren (über 100x) für Mikrometer-große CIGSe-Solarzellen, ohne die Gesamtleistung zu beeinträchtigen, indem die Miniaturisierung der Zellen ausgenutzt wird.

Selbstständigkeitserklärung

Hiermit versichere ich, die vorliegende Arbeit selbstständig und unter ausschließlicher Verwendung der angegebenen Quellen und Hilfsmittel erstellt zu haben.

Die Arbeit wurde weder in gleicher noch in ähnlicher Form einer anderen Prüfungsbehörde vorgelegt oder veröffentlicht.

Berlin, den 05.10.2018

Diego Sancho Martínez